Synthesis of Bio-based Block Copolymers with Conjugated Segments and Their Applications in Electronic Devices

A Dissertation for the Degree of Doctor of Philosophy

LI-CHE HSU

Hokkaido University

September 2021

Acknowledgements

The study presented in this dissertation has been performed under the co-supervision of professor Toshifumi Satoh, Division of Applied Chemistry, Faculty of Engineering at Hokkaido University, and professor Wen-Chang Chen, Department of Chemical Engineering, College of Engineering at National Taiwan University. Professor Satoh provided me a great vision for material design, sharpened my skills in polymer synthesis and supported me in realizing my research plan with tremendous guidance and encouragement. Professor Chen gave me valuable guidance with his huge background in optoelectronic devices, and advised me to find the best way to bring our materials into applications. I would like to express my greatest and sincerest appreciation to my two supervisors for all the guidance and words of wisdom throughout my wonderful and exciting academic journey. They set great examples as polymer scientists for me to follow, and I couldn't have imagined a better teacher and mentor in my pursuit of doctorate program.

I am also grateful to professor Takuya Isono, Division of Applied Chemistry, Faculty of Engineering, Hokkaidio University, who is a young and talented polymer chemist, and a good baseball player. I thank him for teaching me laboratory skills, and for all the inspiring discussions and suggestions during my stay in Polymer Chemistry Lab at Hokkaido University.

Much appreciation is expressed to professor Tajima, professor Yamamoto and professor Sada for providing useful suggestions to raise the value of my doctoral dissertation.

I also thank to Mr. Saburo Kobayashi for teaching me polymer synthesis and for the collaborations in developing functional conjugated polymers. I wish him the best luck in pursuing his Ph. D. degree.

I appreciate my lab members in Polymer Chemistry Lab including Mato, Katsuhara, Ryoto, Saki, Shingu, Nao, Takojima and Yasuko for treating me as their members since the first day we met. I also pay my gratefulness to the international students that I have met in this lab including Yubo, Bo-Yu, Ching-Heng, Dai-Hua, Alice, Lucy and Chris. Together we shared good memories of studying and visiting in Japan.

Special thanks goes to two of my seniors, doctors Kodai Watanabe and Brian Ree. Doctor Watanabe accompanied me to accommodate the life in Hokkaido from the first day I arrived. He is a cool Japanese person and the life and working style he presented to me was truly fascinating and intriguing. Doctor Ree shares similar interests to me in music and we had unforgettable moments in playing music together. He also taught me a lot on synchrotron experiments and showed me the good attitudes from a disciplined researcher. Now he became a specially appointed assistant professor in Hokkaido University, and I wish him all the best in his academic career.

Last but not least, I extend my love and gratitude to my family and my girlfriend Bonnie. Without them I couldn't make it so far.

September, 2021

Abstract

In this dissertation, bio-based and stretchable semiconducting polymers through elegant design of conjugated block copolymers (BCPs) with linear and branched soft segments of poly(δ-decanolactone) (PDL) were developed. PDL was chose as the green and soft building block in the target BCPs since it is a bio-based soft polymer with a metal-free and living ring-opening polymerization process. Conjugated-insulating BCPs were prepared through Cu-catalyzed azido–alkyne click reaction (CuAAC) between azido-functionalized PDLs and typical conjugated polymers with alkyne functional group including poly(3-hexylthiophene) (P3HT) and poly(9,9-di-*n*-hexyl-2,7-fluorene) (PF). Thermal, mechanical and electronic properties were systematically studied for the stretchable electronic applications. In chapter 2, I propose soft-hard-soft type triblock BCPs with poly(3-hexylthiophene) (P3HT) and branched PDL segments to enhance stretchability of BCP without sacrificing charge mobility. The BCPs with AB, AB_2, B_2AB_2 and B_3AB_3 structure (A: P3HT, B: PDL) exhibit competitive hole mobility of 0.088, 0.085, 0.089 and 0.045 $cm^2 V^{-1} s^{-1}$, respectively. Interestingly, stretchability of the BCPs increases by introducing soft-hard-soft structure and the branched soft segments, as investigated by optical microscopy (OM) and amplitude modulation-frequency modulation atomic force microscopy (AM-FM AFM). This can be attributed to more random phase separation and smaller P3HT crystallites of the branched triblock BCPs. Finally, OFETs with the stretched and transferred semiconducting layer of the BCPs were fabricated and the B_3AB_3 device shows the highest mobility retention among all the synthesized BCPs (72%-75%) under 100% strain, and 71-75% mobility retention after 500 stretch-release cycles at 50% strain. In chapter 3, poly(9,9-di-*n*-hexyl-2,7-fluorene)-*block*-poly(δ-decanolactone)s (PF-*b*-PDLs) with AB, AB_2 and AB_3 structure (A: PF, B: PDL) were designed as stretchable charge-storage layer of organic field-effect transistor (OFET) memory. The BCP thin films exhibit extraordinary

stretchability with no cracks observed by optical microscopy (OM) under up to 100% strain owing to the incorporated PDL soft segments. Meanwhile, the trapping density of the electret film of the branched polymers is boosted by the tailored phase separation and higher crystallinity of the BCPs. Quantitative analysis of the polymer thin films on the atomic force microscopic (AFM) images was performed to correlate thin film morphology with memory device performance. As a result, PF-*b*-PDL_3 device exhibits the largest memory window (102 V) and the highest memory ratio (3.5×10^4). OFET memories made by the stretched and transferred BCPs can retain their memory performance under up to 100% strain, and the PF-*b*-PDL_3 device can endure 500 stretch-release cycles at 50% strain with 84% memory window retention. These results highlight the importance of architecture design on modulating electronic properties and stretchability of conjugated BCP using bio-based and soft polymer as building blocks.

Table of Contents

Chapter 1

Introduction

1.1 Stretchable Polymer Semiconductors: Design, Synthesis and Applications

Since the first discovery of the semiconducting property of the doped polyacetylene in 1977,[1] great efforts have been paid on the development of high-performance conjugated and semiconducting polymers. Until now, conjugated polymers have already been employed as the active layers of light-emitting diodes (LED),[2, 3] photovoltaics,[4, 5] organic field-effect transistors (OFET),[6, 7] memory devices,[8, 9] as well as the biological sensors.[10, 11] Meanwhile, conjugated polymers possess promising electronic properties such as charge mobility, which are even catching up with those of the inorganic counterparts in the recent years.[12] Nowadays, the industry and academic worlds have shifted their interests into the applications of wearable electronics.[13-16] Such electronic products should overcome the mechanically mismatch with human body while maintaining their performance. Conjugated and semiconducting polymer materials are particularly promising in this field due to their mechanical deformability, solution processibility, low-cost and large-area production capability.[12, 17, 18] This section will focus on the design strategies of stretchable semiconducting polymer materials and their applications on optoelectronic and memory devices.

1.1.1 Design and Synthesis

Generally, a polymeric semiconductor for stretchable electronics should have relative low tensile modulus (~ 1GPa or lower) and be stretchable at least in its thin-film state,[12] and the electronic perfromance such as charge mobility and charge-storage ability should be retained while upon stretching. Here I inroduce the strategies to produce stretchable semiconducting polymers including polymer blends, back-bone engineering, side-chain engineering and conjugated block copolymer with soft segments.

1.1.1.1 Polymer Blends

A simple strategy to create extrinsically stretchable semiconductor is to physically blend polymer semiconductor with an elastomer with low glass transition temperature (T_g). One of the first example was published by Jeong et al. in 2015.[19] They blended poly(3-hexylthiophene) (P3HT), which is a typical polymer semiconductor for OFET that possesses modulus over 1GPa and crack on-set strain of 9%,[20] with a low elastic modulus polymer, polystyrene-*block*-poly(ethylene-co-butylene)-*block*-polystyrene (SEBS) to achieve stretchable active layer of OFET (**Fig. 1.1a**). The OFET fabricated by the stretched polymer blend layer could endure strain up to 50%. Although the mechanical properties were significantly improved, the charge mobility (2×10^{-3} cm^2 V^{-1} s^{-1}) is limited to the insulating nature of SEBS and intrinsic mobility of P3HT. Therefore, this method has also been adopted on higher charge mobility polymers.

Recently, Bao et al. successfully fabricate a highly stretchable polymer semiconductor films through the nanoconfinement effect of diketopyrropyrrole (DPP)-based semiconducting polymer in SEBS (**Fig. 1.1b**).[21] The nanofibers of semiconductor formed from phase separation show reduced crystallinity but still with high aggregation. As a result, charge mobility of the blended films with 70% of SEBS is over 1 cm^2 V^{-1} s^{-1}, which is comparable with the pristine polymer, and could retain its performance under up to 100% strain. To decrease the amount of insulating materials in the blending system, researchers have proposed another strategy of conjugated/conjugated polymer blends including regiorandom P3HT/regioregualar P3HT blends[22] and P3HT/[1,2,5]thiadiazolo[3,4-c]pyridine] (PCDTPT) blends[23] to manipulate plasticity of the high-performance but brittle semiconducting polymers.

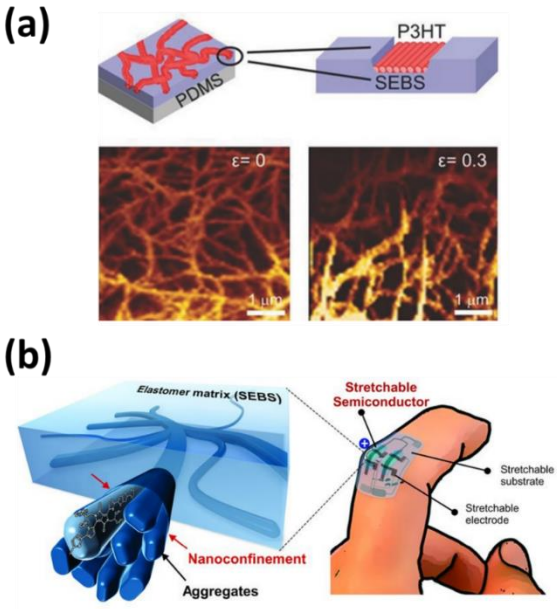

Fig. 1.1 Polymer blends through stretchable semiconductors: (a) P3HT/SEBS blends[19] and (b) poly(2,5-bis(2-octyldodecyl)-3,6-di(thiophen-2-yl)diketopyrrolo[3,4-c]pyrrole1,4-dione-alt-thieno[3,2-b]thiophen) (DPTT-TT)/SEBS blends.[21]

1.1.1.2 Back-Bone Engineering

Although the abovementioned blending method could provide stretchable semiconductor, researchers are still interested in building an intrinsically stretchable semiconductor through molecular design of the conjugated polymers. Three commonly used strategies are side-chain engineering, back-bone engineering and conjugated block copolymer (BCP) with soft segment. For back-bone engineering, Wu et al.[24] reported that the conjugated polymers with fused rings and high crystallinity, such as DPP-based polymers possess high mobility and lower stretchability. On the other hand, the polymers with separated rings and long alkyl side chains show superior stretchability, and the charge mobility can be maintained at up to 100% strain. Mei[25] developed a facile method to create stretchable and high-performance semiconducting polymer by introducing conjugation break spacers into the backbone (**Fig. 1.2a**). By randomly introducing different amount and length spacers, mechanical properties of the polymer can be effectively controlled without drastically affect the charge mobility. Lipomi[26] developed another elegant strategy to randomly introduce tail-to-tail coupled units of two 3-hexylthiophene rings (bithiophene, 2T) segments into a DPP-based polymer (PDPP2FT), in which the elastic modulus can be reduced without breaking the conjugation of the backbone (**Fig. 1.2b**). Meanwhile, the solar cell with the active layer of polymer/PCBM possess higher power conversion efficiency (PCE) of 2.8% against the pristine polymer (2.5%).

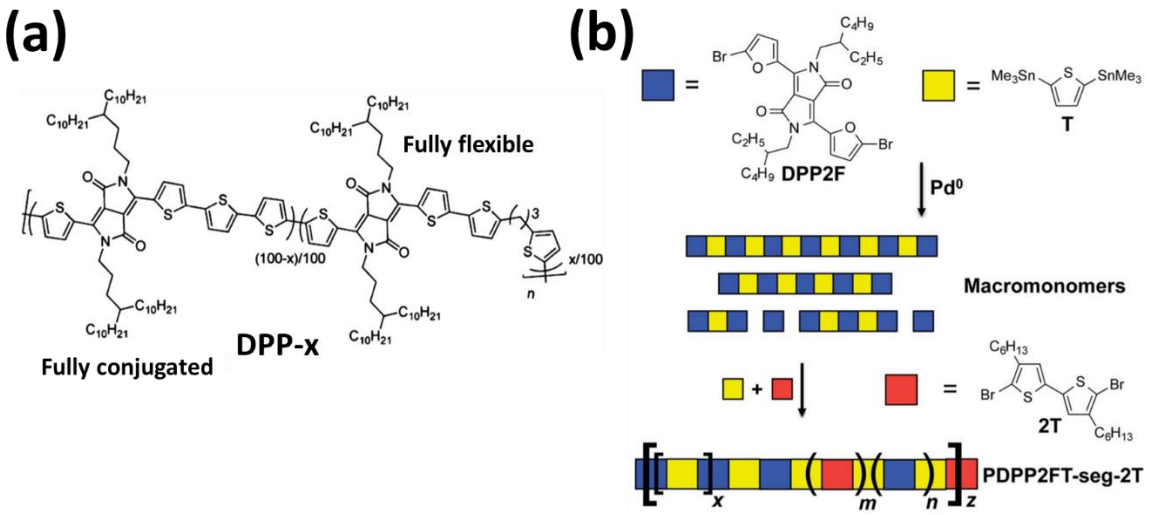

Fig. 1.2 Back-Bone Engineering to improve stretchability: (a) Conjugation break spacer[25] and (b) random segmentation.[26]

1.1.1.3 Side-Chain Engineering

A pioneering work on the side-chain engineering of semiconducting polymer was conducted by Lipomi et al.[20] on a class of poly(3-alkylthiophene)s (P3ATs) with different length of alkyl side chain, in which they concluded that the tensile modulus and brittleness of the P3ATs and their blends with [6,6]-phenyl-C61-butyric acid methyl ester (PCBM) decreased with the increasing length of alkyl side chain (**Fig. 1.3a**). In the following work, they did a systematical study on mechanical properties and device performance of the physical blends, block copolymer, random copolymer of P3HT and poly(3-octylthiophene), and poly(3-heptylthiophene) (P3HpT), and the results suggest that P3HpT exhibits the best photovoltaic properties with the lowest modulus.[27] Aside from the aliphatic side chains, Chen et al. introduced branched carbosilane side chains and butyl acrylate side chains on the isoindigo-

based polymers (**Fig. 1.3b and c**) [28-30] to achieve high-performance n-type semiconductor that could endure up to 100% strain and could maintain charge mobility above 1 $cm^2V^{-1}S^{-1}$. Other approaches such as asymmetry side chains,[31] hydrogen bonding-containing side chains[32, 33] and biaxially-extended conjugated side chains[34] have also been reported recently.

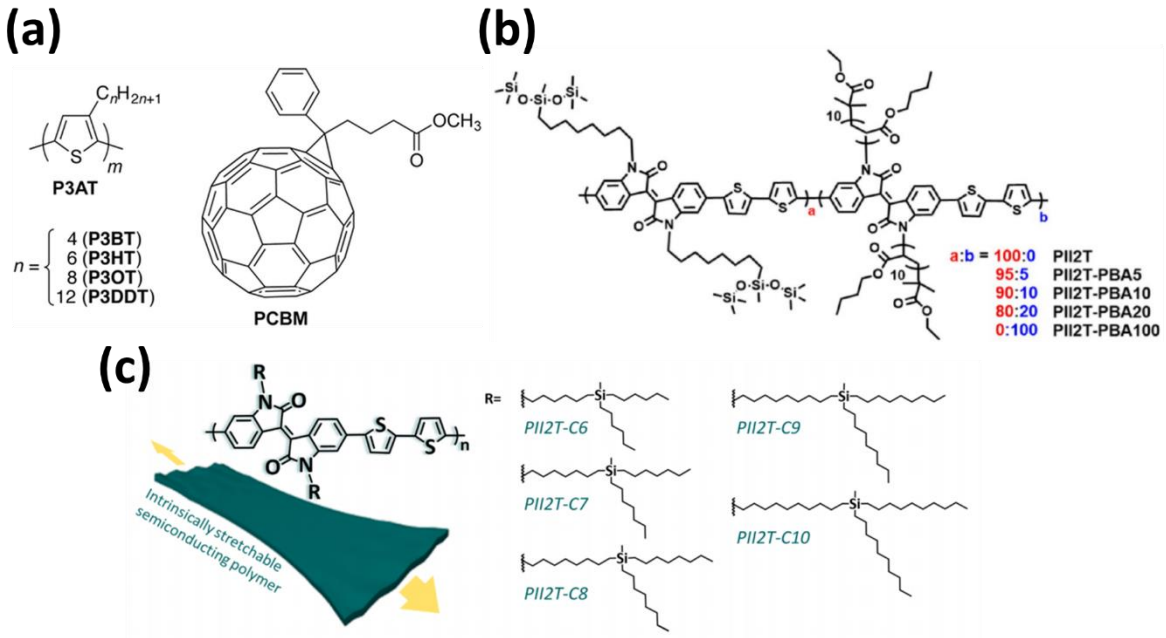

Fig. 1.3 Side-Chain Engineering to improve stretchability: (a) length of side chains[20] (b) butyl acrylate side chain[29] and (c) branched carbosilane sidechain.[30]

1.1.1.4 Conjugated Block Copolymer with Soft Segments

Incorporating an insulating soft segment directly to the conjugated polymer is another route to achieve stretchable semiconductor. Conjugated block copolymer (BCP) with soft segments can be produced from click reaction between a conjugated block and a soft insulating block. For the insulating block, a variety of soft polymers such as polyethylene, polyisoprenes,

polyacrylates, polyethers and polylactones can be used. For the conjugated block, semiconducting polymers with living polymerization process, controllable molecular weight and precise chain end-functionality such as polythiophenes and polyfluorenes are preferred. Stingelin-Stutzmann et al.[35] firstly reported that the poly(3-hexylthiophene)-*block*-polyethylene diblock copolymer shows higher elongation and lower elastic modulus than the pristine P3HT (**Fig. 1.4a**). However, they didn't report the charge mobility of the stretched polymer thin films. Chen et al.[36] synthesized a series of diblock copolymers, poly(3-hexylthiophene)-*b*-poly(butylacrylate)s (P3HT-*b*-PBAs) and fabricated the OFETs based on the stretched and transferred polymer semiconductor films (**Fig. 1.4b**), in which they suggest $P3HT_{5k}$-*b*-PBA_{6k} with the optimized conjugated/insulating block ratio exhibits the best stretchability that could endure up to 100% strain with favorable charge mobility over 10^{-2} $cm^2V^{-1}S^{-1}$. Aside from the weight or volume ratio of conjugated/insulating segments, polymer architecture is also a significant factor that could affect electronic and mechanical properties. P3HT-based triblock copolymers with hard-soft-hard type architecture have been proposed recently to mimic the elastic behavior of the SBS elastomer (**Fig. 1.4c**).[37-39] Despite the improved mechanical properties, the polymers possess much inferior semiconducting properties with the mobility of 10^{-4} – 10^{-3} $cm^2V^{-1}S^{-1}$ due to the interrupted conjugation of the P3HT backbone. Therefore, new architecture design for polythiophene-based BCP is required to enhance stretchability without sacrificing charge mobility. Despite the weak mobility

compared with polythiophenes, polyfluorenes are potential in other fields such as light-emitting diodes (LED)[40, 41] and memory device.[42-44] BCP strategy has already been applied on polyfluorenes to develop stretchable emissive materials. For example, diblock copolymers of polyfluorenes such as poly(hexylfluorene)-*block*-poly(butyl acrylate) (PF-*b*-PBA)[45, 46] and poly(octylfluorene)-*block*-polyisoprene[47] have been synthesized to develop stretchable and luminescent polymer films and fibers. Facile synthetic strategies and other useful architecture designs for stretchable and high-performance conjugated BCP are highly expected.

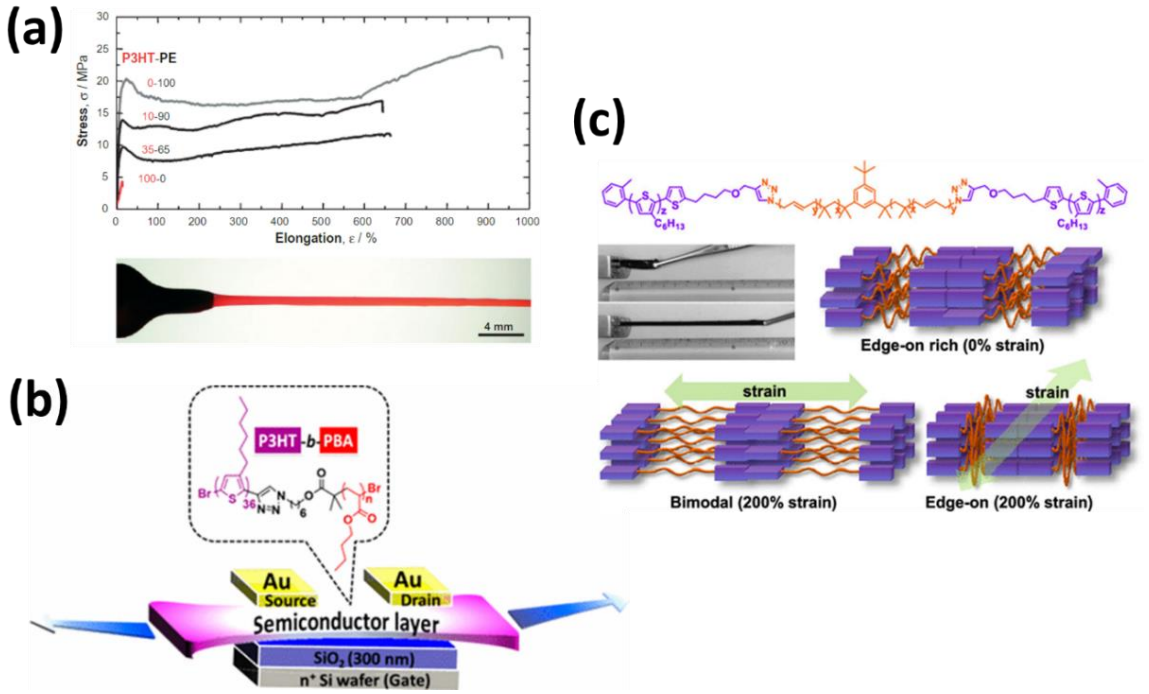

Fig. 1.4 Conjugated BCP with soft segments: (a) P3HT-*block*-PE[35] (b) P3HT-*b*-PBA[36] and (c) hard-soft-hard type triblock copolymer of P3HT-*b*-PIB-*b*-P3HT.[38]

1.1.2 Applications

Stretchable semiconducting polymers possess advanced stretchability as well as different functionalities including charge transportation, charge-trapping and light emission, leading to their widespread applications on stretchable electronic and optoelectronic devices such as LED, photovoltaics, OFET and memory device. Here I focus on the development of stretchable semiconducting polymers as the active (charge transporting) and charge-trapping layers in stretchable devices.

1.1.2.1 Stretchable Active Layer of Optoelectronic Devices

Stretchable polymer semiconductors can be utilized as active layers of organic field-effect transistor (OFET) and organic photovoltaic (OPV). Owing to the relatively simple device geometry, OFET has been proved as a powerful tool to evaluate semiconducting properties of the stretchable active layers. O'Conner et al.[48] demonstrated a method to evaluate the charge mobility of the semiconductor film under strain through the bottom gate, bottom contact FET geometry (Si/SiO_2/semiconductor/Au). In this approach, a polymer film is first deposited on top of a hydrophobic silicon wafer treated with a silane self-assembly monolayer. Then the polymer film is transferred to a cross-linked PDMS elastomer, stretched at different strain loadings and transferred to a secondary Si/SiO_2 wafer to fabricate the OFET. Hydrophobic nature of the silicon wafer enables the chain alignment of the conjugated backbones and

facilitates the release and transfer of the polymer thin films. Using this method, performance of stretchable semiconductor such as charge mobility and on-off current ratio can be evaluated before realizing a fully stretchable transistor. Motivated from this research, Wu et al.[24] developed a noninvasive contact lamination method with bottom gate geometry (Si/SiO_2/Cr-Au/semiconductor), which employs the film transferring process but doesn't require the deposition of source-drain electrodes on top of the transferred polymer films. Until now, a variety of stretchable semiconducting polymers have been developed and their semiconducting performance are evaluated based on the abovementioned approaches.[21, 28-34, 36, 49] Besides the evaluation of the performance of the semiconductor, fully stretchable transistors based on the stretchable substrates, dielectrics, semiconductors and electrodes have already been reported (**Fig. 1.5**). Some of the devices can endure up to 100% strain and the charge mobility could be retained over 0.1 $cm^2V^{-1}S^{-1}$.[21, 32, 50] It is worth to mention that the film transferring process of the semiconductor deposited on hydrophobic silicon wafers is still preferred for the fabrication of stretchable transistors to promote charge transportation of the semiconductor. As the active layer of OPV, mechanical properties of P3HT/fullerenes,[20, 51] polymer/polymer[52] and ternary blends[53] have been studied. However, compared with the progress of OFETs, the development of fully stretchable OPVs based on intrinsically stretchable materials is slightly lagged behind with a few reports,[54, 55] which is due to the more complicated device structure and lower power conversion efficiency of the polymer-based semiconductors.[56, 57]

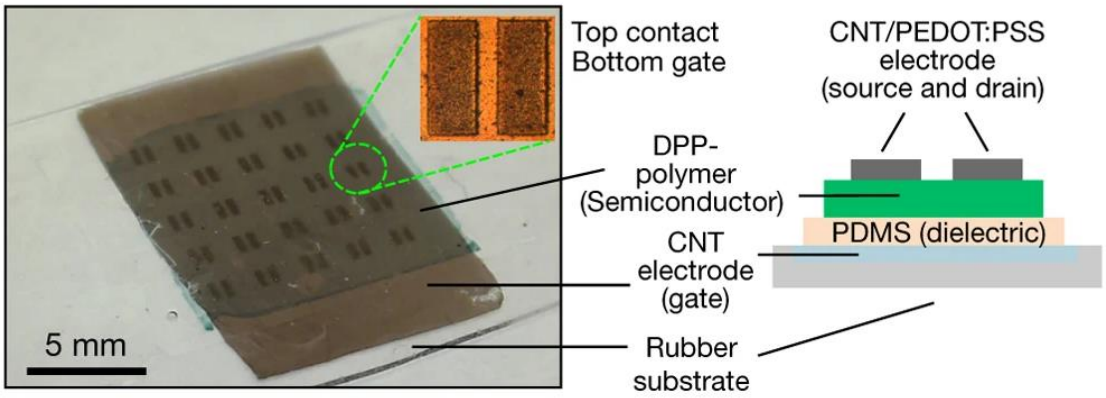

Fig. 1.5 An example of fully stretchable transistor and transistor arrays.[32]

1.1.2.2 Stretchable Charge Storage Layer of Memory Devices

In addition to serving as an active layer, some of the semiconducting polymers can function as charge-storage layer of memory devices. Such polymers are not necessarily with high charge mobility, but should have suitable nanostructures and energy levels for charge injection and stabilization.[58] For example, fluorene-, thiophene- and carbazole-containing polymers have widely been employed as the memory layer for memory devices.[59] Polymer-based memory devices have been extensively reported with resistor-type and transistor-type geometries (**Fig. 1.6**),[60] for which the resistor-type memory consists of an active layer sandwiched between the top and the bottom electrodes, and the transistor-type memory is made by introducing an additional charge-storage layer to the interface between the dielectric layer and semiconducting layer of the conventional OFET. Recently the research interests have been shifted toward the development of stretchable memory elements and memory device

applications due to the requirements of data storage in wearable and health-care electronic devices.[61-63] BCPs with phase separation nanostructures and elastic properties provide by the soft segments can serve as the intrinsically stretchable memory element. For example, conjugated BCPs of poly[2,7-(9,9-dihexylfluorene)] (PF) rods and electron-withdrawing poly(pendent isoindigo) (Piso) coils were employed to fabricate the fully stretchable resistor-type memory (**Fig. 1.7a**).[44] Furthermore, although those are not conjugated polymers, sugar-based BCPs with different architectures are studied comprehensively as stretchable charge-trapping layers for the both resistor- and transistor-type memories (**Fig. 1.7b**).[64, 65] New materials that possess charge-trapping ability with stretchability are highly desired.

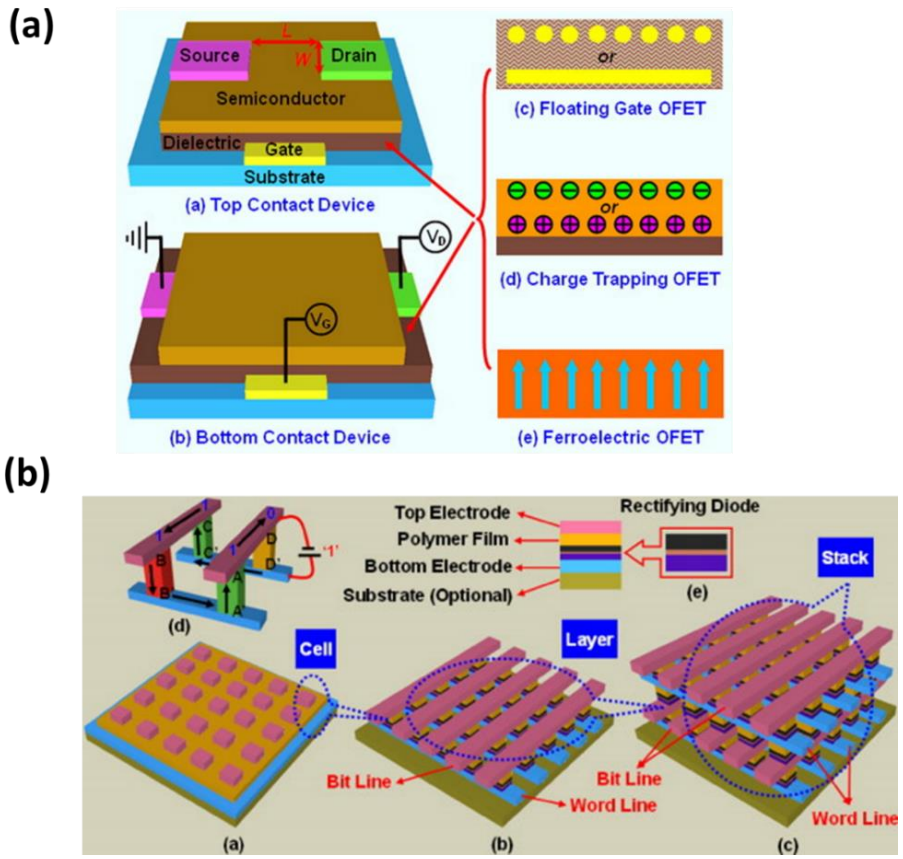

Fig. 1.6 Schematic illustration of (a) transistor-type memory and (b) resistor-type memory.[60]

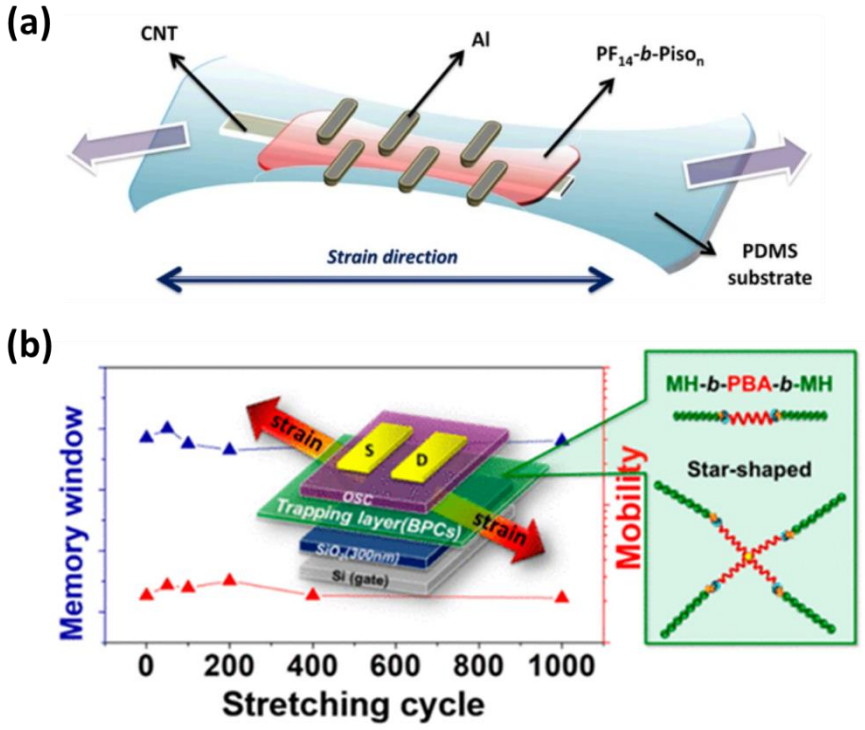

Fig. 1.7 Examples of stretchable (a) transistor-type[75] and (b) resistor-type memory.[44]

1.2 Introduction to Bio-Based Polymers

Bio-based polymers are derived from renewable carbon resources which can be extracted from plant and wood biomass such as starch, cellulose, lignin or plant oil. Those resources are produced by photosynthesis from carbon dioxide and water in the atmosphere and soil.[66] Bio-based polymers can be produced from three different ways: (1) Using nature polymers with additional modification to meet the requirements, (2) Producing bio-based polymers directly through bacteria, and (3) Polymerization of bio-based monomers to achieve bio-based polymers.[67] Once the bio-based polymers are burned after use, the generated carbon-dioxide is again turned into the biomass through photosynthesis, which meets the "carbon neutrality" concept.[66] Moreover, most of the bio-based polymers are biodegradable, which means they can be degraded into carbon dioxide and water by naturally occurring microorganisms. Therefore, bio-based polymers are regarded as eco-friendly alternatives to the conventional petroleum-based polymers.[66, 68] This section summarizes the development of electronic devices made from bio-based polymers, and introduces a novel bio-based polyester, poly(δ-decanolactone) as the promising soft building block of stretchable polymer materials.

1.2.1 Bio-Based Polymers for Optoelectronic Devices

E-waste, or known as Waste Electrical and Electronic Equipment, WEEE, describes the used and discarded electronic devices such as televisions, mobile phones, monitors and medical

devices.[69] Based on the global E-waste monitor report,[69] in 2019, the world produced a striking 53.6 million metric tons (Mt) of e-waste, an average of 7.3 kg per capita. On average, the total weight of e-waste increases annually by 2.5 Mt. Also, in 2019, the formal documented collection and recycling of e-waste was 9.3 Mt, which is 17.4% compared to e-waste generated. As focusing on Asian countries, 24.9 Mt of e-waste was produced in 2019 while only 11.7% of it (2.9 Mt) was recycled, showing that there is a long way to go for us to reduce environmental impact of the wasted electronic products.[69] In recent years, polymer-based electronic devices have been developed vigorously in industry and academia due to simple fabrication process, tunable electronic performance, and improved mechanical properties. However, most of the polymer materials in electronic devices are petroleum-based, and the used and discarded devices may have huge impact on our environment. On the other hand, bio-based polymers can be derived from nature resources, showing lower energy consumption for production. After the electronic devices were discarded and burned, the carbon dioxide generated from bio-based component will return back to nature through photosynthesis. Therefore, making electronic devices by bio-based polymers is beneficial for reducing the environmental impacts.[70, 71]

In the field of thin-film electronic devices, bio-based polymers can be directly used as substrates, dielectric layer of OFET, charge trapping layer of memory device and interlayer of OPV. Bio-based substrates attracted the early attentions since the substrate comprises over 99% of the thin-film device by mass. Starch paper and cellulose have widely been used as

mechanically robust flexible substrates of OFETs and OPVs.[72, 73] Bio-based materials with abundant polar groups such as silk, shellac, gelatin and chicken albumen are suitable candidates for dielectric materials.[70, 74] Regarding the application in memory devices, deoxyribonucleic acid (DNA) and oligosaccharide-based materials has been reported as the memory elements of OFET memory and resistor-type memory.[64, 75, 76] Meanwhile, memory behavior and stretchability of the oligosaccharide-based material can be manipulated by their BCP design.[64, 65] Considering the development of OPVs, although the current manufacture is still not environmental friendly, biomaterials such as poly-lysine, peptides, DNA, chitosan, dextrin and cellulose can be used as the interlayers to tune the work function of charge transporting layer or metal electrodes.[77-81] The readers may notice that bio-based polymers is still not capable of replacing the role of synthetic semiconducting polymers on current status. However, by creating composite materials of semiconductor and bio-based polymers through physical blending,[82, 83] or even through chemical bonding reaction,[84-86] one can manipulate the physical properties and enhance biocompatibility of the semiconducting polymer.

1.2.2 Bio-Based and Biocompatible Polyesters

Polyesters are one of the most notable class of polymers in polymer industry. They are widely used in laminating resins, surface coatings, rubbers, fibers, plasticizers and composites.[87] Polyesters can be synthesized from different methods such as through a condensation polymerization of hydroxyacid or diacid with dialcohol or by a ring-opening polymerization of a lactone.[87] Polyhydroxybutyrate (PHB) and polylactic acid (PLA) are probably the most popular bio-based polyesters. They are truly biodegradable due to the aliphatic chemical structure and are proved to possess biocompatibility with animals and human body.[66, 87] However, their applications are limited by their brittleness and narrow processing window. Therefore, physical blending or copolymerization with another synthetic polymer is required to achieve mechanically robust materials. For example, poly(lactic-co-glycolic acid) (PLGA), which is a random copolymer of lactic acid and glycolic acid, can serve as an biocompatible and resorbable substrate for flexible electronic device (**Fig. 1.8a**).[88] Another interesting bio-based polyester that receives more research attentions recently is polyethylene furanoate (PEF), which is an alipharomatic polyester synthesized through condensation polymerization of bio-based 2,5-furandicarboxylic acid (FDCA) with ethylene glycol. Due to its outstanding flexibility and thermal stability, PEF is regarded as a green alternative to the well-known petroleum-based polyester, polyethylene terephthalate (PET).[89, 90] Based on these advantages, our group successfully fabricated flexible transistor, solar cell

and memory device on PEF substrates (**Fig. 1.8b**).[76, 91] Concerning the applications in stretchable electronics, polymers with soft and elastic properties and T_g below room temperature are favored. Poly(ε-caprolactone) (PCL) is a non-bio-based, yet biodegradable aliphatic polyester with a melting point (T_m) at around 60°C and a T_g at around -60°C.[92] Polymer blends of PCL and PLA with improved mechanical properties can serve as biocompatible materials in tissue engineering.[93, 94] Moreover, PCL has also been incorporated with conjugated polymer to realize a stretchable and degradable semiconducting BCP.[95] These examples reveal the potential of aliphatic polyesters on improving the mechanical performance of stretchable electronic devices.

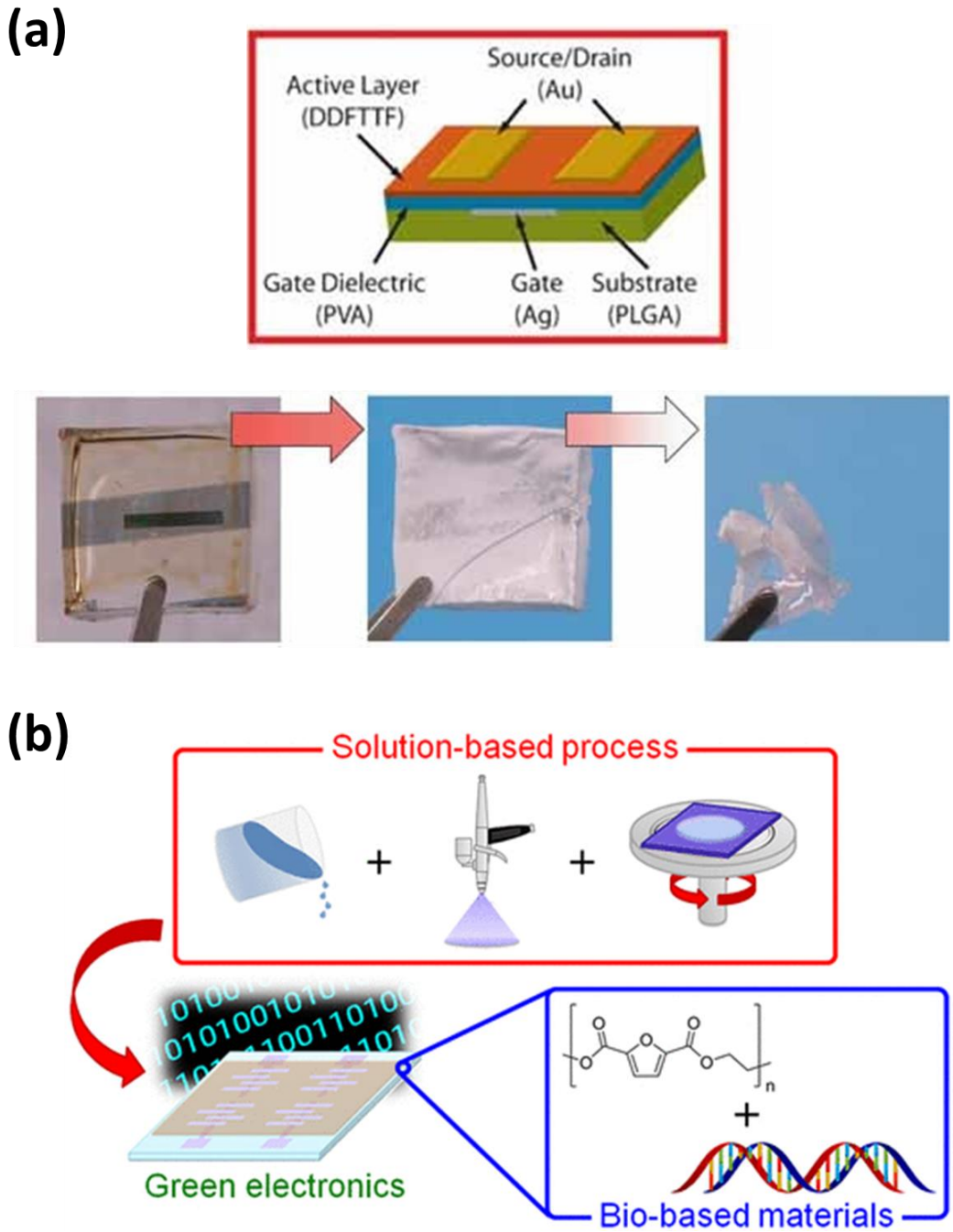

Fig. 1.8 (a) Transistor made by biocompatible PLGA,[87] (b) resistor-type memory made by bio-based PEF and DNA.[74]

1.2.3 Poly(*δ*-decanolactone) (PDL): A Bio-Based and Soft Polyester

Poly(*δ*-decanolactone) (PDL) is a bio-based, amorphous and aliphatic polyester that has already been applied for creating soft materials[96-100] and building drug-delivery systems.[101-103]

As the starting material of PDL, *δ*-decanolactone (*δ*-DL) is a naturally occurring six- membered lactone produced by Cryptocarya massoy and can be obtained in large scale from the flavor and fragrance industry.[104, 105] Natural lactones are mostly with five- and six-membered ring. Due to the most stable ring strain, ring-opening reaction of five-membered lactone is generally not favored. On the other hand, Six-membered lactones like *δ*-DL have thermodynamically favored ring-opening reaction, which can be used to synthesize polyester through ring-opening polymerization.[106, 107] Regards polymer properties, most of the aliphatic polyesters made by ring-opening polymerization are crystalline,[108] which may not be suitable candidate for soft polymer material. Since *δ*-DL has long alkyl chain attached on lactone ring, I can expect the resultant polyester with alkyl side chain to be non-crystalline material with a low-glass transition temperature, T_g. Therefore, *δ*-DL is a great choice of monomer for making soft polymer. Also, since crystallization of polymer will not occur during polymerization, the monomer can be polymerized in bulk without using any solvent at low temperature, providing an atom and energy-economic polymerization process. In 2011, Hillmyer and his coworkers successfully synthesized PDL through a bulk ring-opening polymerization of *δ*-DL (**Fig. 1.9a**).[96] By using 1,4-benzenedimethanol as initiator and 1,5,7-triazabicyclo[4.4.0]dec-5-ene (TBD) as catalyst, they derived PDL with two hydroxyl group at the both chain-ends. The polymer shows well-controlled molecular weight and dispersity (*Đ*), and is amorphous with the T_g at -51°C. Further adding racemic D,L-lactide into the polymerization system led to a

microphase separated triblock copolymer, PLA-*block*-PDL-*block*-PLA with two distinct T_g at -51ºC and 54ºC. In their following work, they used low molecular weight PDL-diols as the soft segment to create a bio-based polyurethane elastomer.[97] On the other hand, Makiguchi, Satoh and Kakuchi[109] developed an efficient living ring-opening polymerization of lactones with a weak acid organocatalyst, diphenyl phosphate (DPP), which is commercially available, metal-free, low-toxicity and chemically stable (**Fig. 1.9b**). By applying this synthetic method on PDL, one can develop a bio-based PDL with metal-free and solvent-free polymerization. Moreover, the living ring-opening polymerization method provides well-controlled molecular weight and *Đ* of polylactones, and the polymer chain-end can be easily functionalized by using azido-functionalized alcohols as initiator or through post-modification. Based on the above studies, bio-based BCPs with soft PDL segments and hard oligosaccharide segments have been synthesized to realize fully bio-based and stretchable materials (**Fig. 1.9c**).[99, 100] As a soft building block with controlled molecular weight and end-functionalities, PDL shows high potential in developing new functional and stretchable polymer materials.

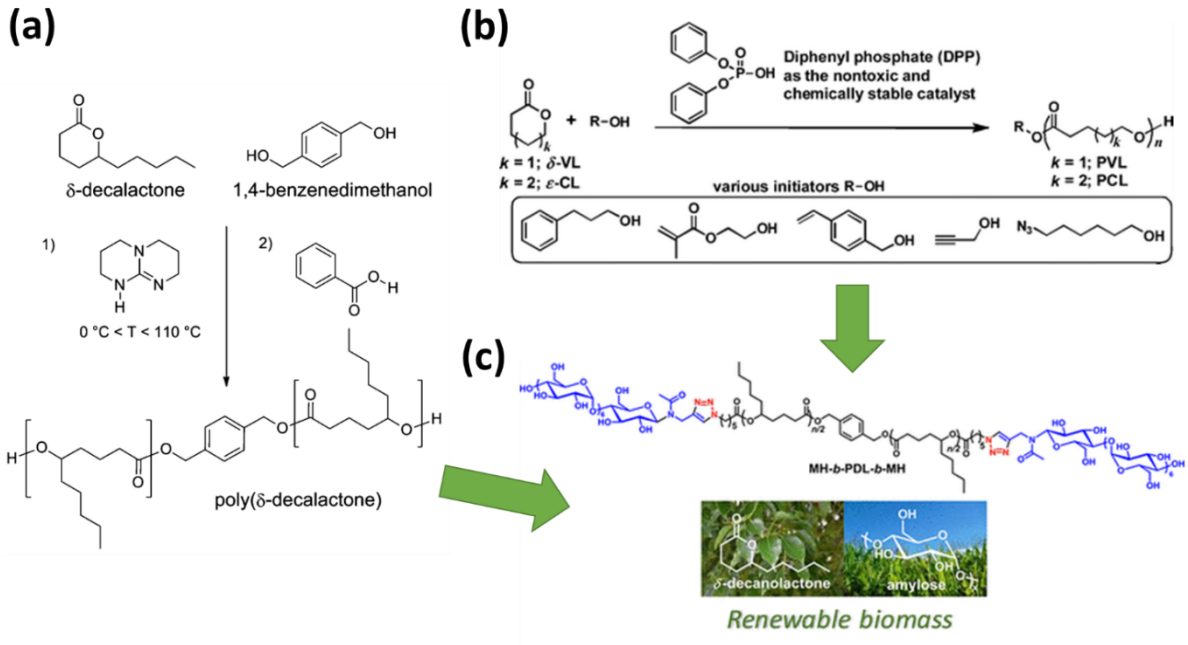

Fig. 1.9 Development of PDL-based BCP: (a) Bulk polymerization of δ-DL,[96] (b) DPP as green catalyst,[109] and (c) biomass BCP of oligosaccharide and PDL.[99]

1.3 Research Objectives

Since limited studies on bio-based semiconducting polymers have been reported, I proposed a facile synthetic strategy to develop novel PDL-based conjugated BCPs with two different conjugated segments including poly(3-hexylthiophene) (P3HT) and poly(9,9-di-*n*-hexyl-2,7-fluorene) (PF). In my research, two major functions of PDL are to increase bio-based content of polymer, and to improve stretchability. Aside from the choice of polymer, miktoarm topology of BCP with branched soft segment was adopted to advance polymer properties. As shown in **Fig. 1.10a**, in a previous study on maltoheptaose-*block*-polycaprolactone (PCL), miktoarm topology with branched maltoheptaose or PCL segment was used to control surface curvature between two blocks, leading to controllable phase separation of BCP.[110] In another study (**Fig. 1.10b**), branched polylactide (PLA) was used to form diblock BCP with polyfluorene and to manipulate phase behavior.[111] However, PLA is a crystalline polymer with no stretchability, which is not helpful for making stretchable conjugated BCP. Therefore, in my study, I will investigate the architecture effect of branched soft segments on properties of conjugated BCP, for the first time. Branched soft segments in conjugated-insulating BCP are expected to create higher curvature between two blocks, thus affecting phase separation of BCP and crystallinity of conjugated segment. Strategies to advance electronic property and stretchability of conjugated BCP through architecture design will be proposed.

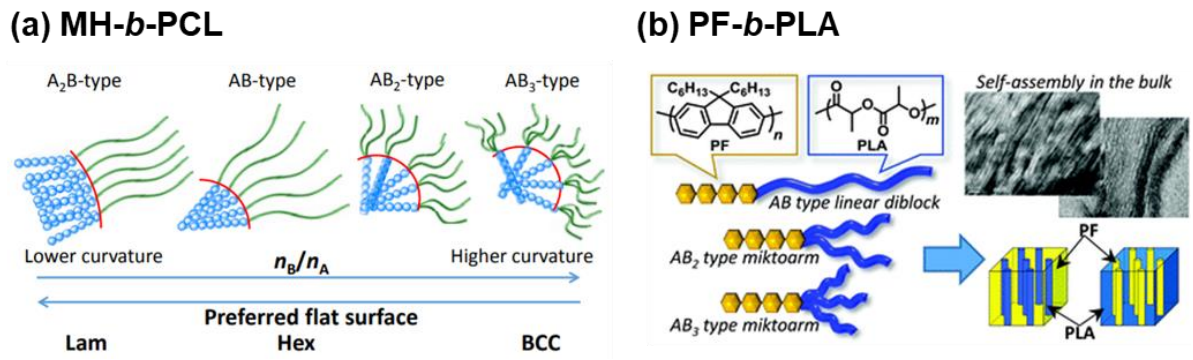

Fig. 1.10 Topology effect of miktoarm branched BCPs on phase behavior: (a) maltoheptaose-*block*-polycaprolactone (MH-*b*-PCL)[110] and (b) polyfluorene-*block*-polylactide (PF-*b*-PLA).[111]

Fig. 1.11 summarizes the research objectives in this dissertation. Azido-functional PDLs with linear and branched structure were produced by living ring-opening polymerization of *δ*-DL using azido-functional alcohol, diol and triol as initiators. On the other hand, P3HT and PF with alkyne functional groups, were synthesized. Cu-catalyzed azido–alkyne click reaction (CuAAC) were conducted between the PDL and conjugated segments to achieve the target polymers. Such polymers are potential in the applications of OFET and OFET memory device. The detailed research objectives are presented below:

Poly(3-hexylthiophene)-*block*-poly(*δ*-decanolactone)s: Toward High-Performance and Stretchable Semiconducting Material Through Branched Soft-Hard-Soft Type Triblock Copolymer Design (Chapter 2)

In the development of conjugated BCP, P3HT-based BCP has the most elaborate synthetic technique with multiple architecture design such as diblock, triblock and branched architecture.

Therefore, in my research I further propose a delicate design of branched soft-hard-soft type polymers. P3HT-*b*-PDLs with AB, BAB, B_2AB_2, B_3AB_3 architectures (A: P3HT, B:PDL) are designed for high-performance and stretchable semiconducting layer of OFET. The branched soft segments are expected to tailor phase separation of the BCP without affecting the conjugation of the P3HT block, leading to a semiconducting material with advanced stretchability. Thermal, mechanical and electronic properties of the polymers will be discussed. Also OFETs with the stretched and transferred polymer layer will be evaluated to manifest the BCP design strategy.

Poly(9,9-di-*n*-hexyl-2,7-fluorene)-block-poly(*δ*-decanolactone)s: Effect of Soft Segment Branching on Electronic Properties of Stretchable Polymer Electret (Chapter 3)

Despite the inferior charge mobility, PF has been reported as an efficient charge-trapping material.[59] Considering structure-property relationships of PF-based BCP, properties of diblock BCP with branched soft segment haven't be fully studied. Also, a reliable strategy for making bi-functional polyfluorene with narrow dispersity has not been developed yet. Therefore, rather than triblock BCP, I designed diblock BCP with branched PDL structure for stretchable memory applications. PF-*b*-PDLs with AB, AB_2 and AB_3 architectures (A: PF, B: PDL) are utilized as the electret layer for OFET memory. Thermal, mechanical and electronic properties will also be evaluated. Moreover, quantitative analysis on the PF nanofibers will be performed using microscopy images. Thus thin film morphology of the BCP can be correlated with

memory device performance. Finally, memory performances of the stretched polymer films are studied to find out the best polymer for memory device.

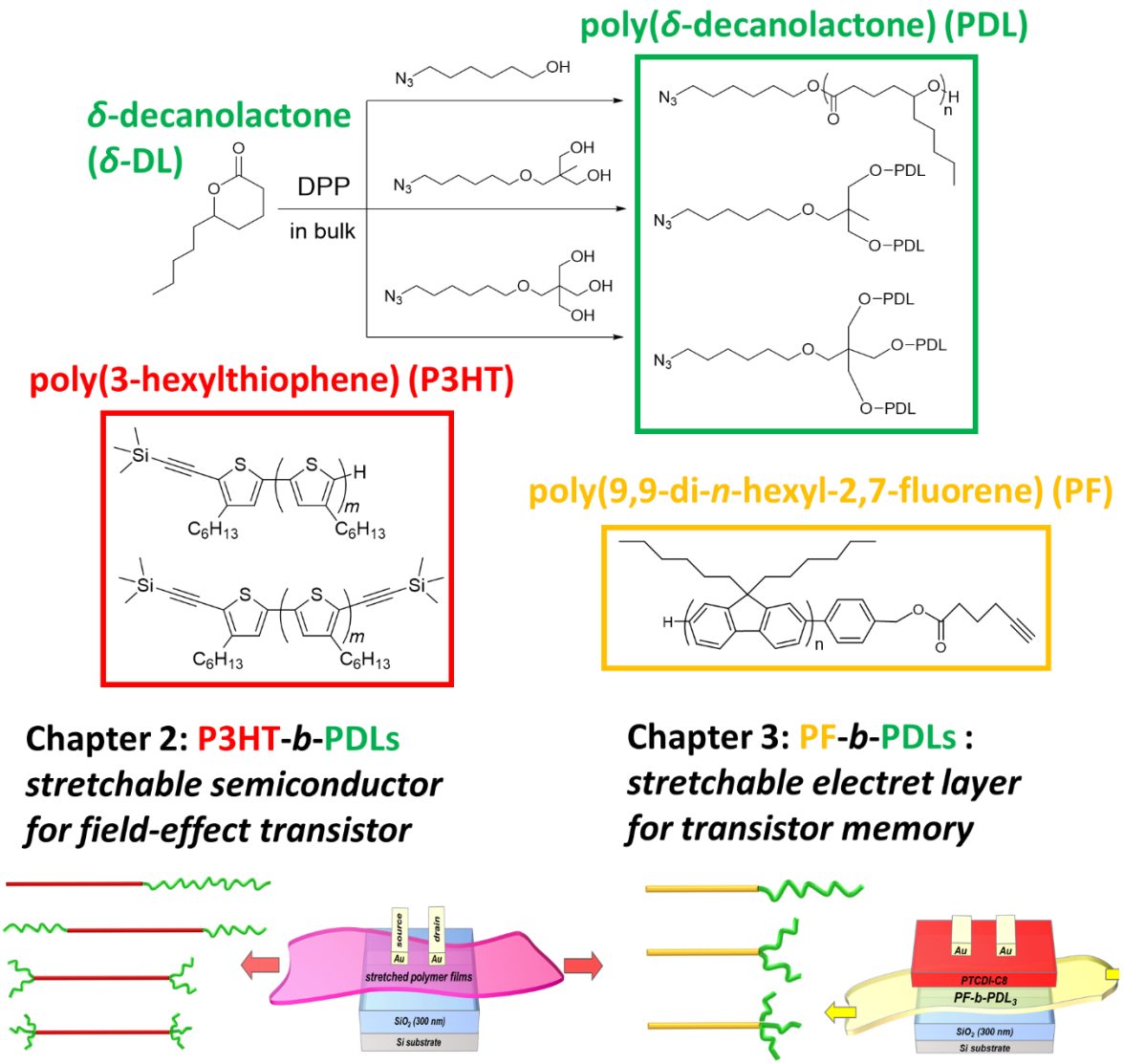

Fig. 1.11 Research objectives: Development of P3HT and PF based block copolymers containing linear and branched bio-based PDL segments for stretchable device applications.

1.4 Reference

1. H. Shirakawa, E. J. Louis, A. G. MacDiarmid, C. K. Chiang and A. J. Heeger, *J. Chem. Soc., Chem. Commun.*, 1977, 578-580.
2. J. H. Burroughes, D. D. Bradley, A. Brown, R. Marks, K. Mackay, R. H. Friend, P. Burns and A. Holmes, *Nature*, 1990, **347**, 539-541.
3. M. Kuik, G. J. A. Wetzelaer, H. T. Nicolai, N. I. Craciun, D. M. De Leeuw and P. W. Blom, *Adv. Mater.*, 2014, **26**, 512-531.
4. C. J. Brabec, N. S. Sariciftci and J. C. Hummelen, *Adv. Funct. Mater.*, 2001, **11**, 15-26.
5. M. Helgesen, R. Søndergaard and F. C. Krebs, *J. Mater. Chem.*, 2010, **20**, 36-60.
6. F. Garnier, R. Hajlaoui, A. Yassar and P. Srivastava, *Science*, 1994, **265**, 1684-1686.
7. H. Sirringhaus, *Adv. Mater.*, 2014, **26**, 1319-1335.
8. J. Ouyang, C.-W. Chu, C. R. Szmanda, L. Ma and Y. Yang, *Nat. Mater.*, 2004, **3**, 918.
9. P. Heremans, G. H. Gelinck, R. Muller, K.-J. Baeg, D.-Y. Kim and Y.-Y. Noh, *Chem. Mater.*, 2010, **23**, 341-358.
10. B. Adhikari and S. Majumdar, *Prog. Polym. Sci.*, 2004, **29**, 699-766.
11. L. Torsi, M. Magliulo, K. Manoli and G. Palazzo, *Chem. Soc. Rev.*, 2013, **42**, 8612-8628.
12. G. J. N. Wang, A. Gasperini and Z. Bao, *Adv. Electron. Mater.*, 2018, **4**, 1700429.
13. M. Stoppa and A. Chiolerio, *Sensors*, 2014, **14**, 11957-11992.
14. Y. Liu, M. Pharr and G. A. Salvatore, *ACS nano*, 2017, **11**, 9614-9635.
15. X. Wang, Z. Liu and T. Zhang, *Small*, 2017, **13**, 1602790.
16. J. S. Heo, J. Eom, Y. H. Kim and S. K. Park, *Small*, 2018, **14**, 1703034.
17. M. Ashizawa, Y. Zheng, H. Tran and Z. Bao, *Prog. Polym. Sci.*, 2019, 101181.
18. J. Onorato, V. Pakhnyuk and C. K. Luscombe, *Polym. J.*, 2017, **49**, 41-60.
19. M. Shin, J. Y. Oh, K. E. Byun, Y. J. Lee, B. Kim, H. K. Baik, J. J. Park and U. Jeong, *Adv. Mater.*, 2015, **27**, 1255-1261.
20. S. Savagatrup, A. S. Makaram, D. J. Burke and D. J. Lipomi, *Adv. Funct. Mater.*, 2014, **24**, 1169-1181.
21. J. Xu, S. Wang, G.-J. N. Wang, C. Zhu, S. Luo, L. Jin, X. Gu, S. Chen, V. R. Feig and J. W. To, *Science*, 2017, **355**, 59-64.
22. P. H. Chu, G. Wang, B. Fu, D. Choi, J. O. Park, M. Srinivasarao and E. Reichmanis, *Adv. Electron. Mater.*, 2016, **2**, 1500384.
23. T. Sun, J. I. Scott, M. Wang, R. J. Kline, G. C. Bazan and B. T. O'Connor, *Adv. Electron. Mater.*, 2017, **3**, 1600388.
24. H.-C. Wu, S. J. Benight, A. Chortos, W.-Y. Lee, J. Mei, J. W. To, C. Lu, M. He, J. B.-H. Tok and W.-C. Chen, *Chem. Mater.*, 2014, **26**, 4544-4551.
25. S. Savagatrup, X. Zhao, E. Chan, J. Mei and D. J. Lipomi, *Macromol. Rapid Commun.*, 2016, **37**, 1623-1628.

26. A. D. Printz, S. Savagatrup, D. J. Burke, T. N. Purdy and D. J. Lipomi, *RSC Adv.*, 2014, **4**, 13635-13643.
27. S. Savagatrup, A. D. Printz, D. Rodriquez and D. J. Lipomi, *Macromolecules*, 2014, **47**, 1981-1992.
28. H.-C. Wu, C.-C. Hung, C.-W. Hong, H.-S. Sun, J.-T. Wang, G. Yamashita, T. Higashihara and W.-C. Chen, *Macromolecules*, 2016, **49**, 8540-8548.
29. H.-F. Wen, H.-C. Wu, J. Aimi, C.-C. Hung, Y.-C. Chiang, C.-C. Kuo and W.-C. Chen, *Macromolecules*, 2017, **50**, 4982-4992.
30. Y.-C. Chiang, H.-C. Wu, H.-F. Wen, C.-C. Hung, C.-W. Hong, C.-C. Kuo, T. Higashihara and W.-C. Chen, *Macromolecules*, 2019, **52**, 4396-4404.
31. Y.-C. Lin, F.-H. Chen, Y.-C. Chiang, C.-C. Chueh and W.-C. Chen, *ACS Appl. Mater. Interfaces*, 2019, **11**, 34158-34170.
32. J. Y. Oh, S. Rondeau-Gagné, Y.-C. Chiu, A. Chortos, F. Lissel, G.-J. N. Wang, B. C. Schroeder, T. Kurosawa, J. Lopez and T. Katsumata, *Nature*, 2016, **539**, 411-415.
33. Y.-C. Lin, C.-K. Chen, Y.-C. Chiang, C.-C. Hung, M.-C. Fu, S. Inagaki, C.-C. Chueh, T. Higashihara and W.-C. Chen, *ACS Appl. Mater. Interfaces*, 2020, **12**, 33014-33027.
34. Y.-W. Huang, Y.-C. Lin, H.-C. Yen, C.-K. Chen, W.-Y. Lee, W.-C. Chen and C.-C. Chueh, *Chem. Mater.*, 2020, **32**, 7370-7382.
35. C. Müller, S. Goffri, D. W. Breiby, J. W. Andreasen, H. D. Chanzy, R. A. Janssen, M. M. Nielsen, C. P. Radano, H. Sirringhaus and P. Smith, *Adv. Funct. Mater.*, 2007, **17**, 2674-2679.
36. J.-T. Wang, S. Takshima, H.-C. Wu, C.-C. Shih, T. Isono, T. Kakuchi, T. Satoh and W.-C. Chen, *Macromolecules*, 2017, **50**, 1442-1452.
37. R. Peng, B. Pang, D. Hu, M. Chen, G. Zhang, X. Wang, H. Lu, K. Cho and L. Qiu, *J. Mater. Chem. C*, 2015, **3**, 3599-3606.
38. T. Higashihara, S. Fukuta, Y. Ochiai, T. Sekine, K. Chino, T. Koganezawa and I. Osaka, *ACS Appl. Polym. Mater.*, 2019, **1**, 315-320.
39. Y.-C. Chiang, S. Kobayashi, T. Isono, C.-C. Shih, T. Shingu, J.-J. Hung, H.-C. Hsieh, S.-H. Tung, T. Satoh and W.-C. Chen, *Polym. Chem.*, 2019, **10**, 5452-5464.
40. D. Neher, *Macromol. Rapid Commun.*, 2001, **22**, 1365-1385.
41. Q. Zhao, S. J. Liu and W. Huang, *Macromol. Chem. Phys.*, 2009, **210**, 1580-1590.
42. X.-D. Zhuang, Y. Chen, B.-X. Li, D.-G. Ma, B. Zhang and Y. Li, *Chem. Mater.*, 2010, **22**, 4455-4461.
43. T.-W. Kim, S.-H. Oh, H. Choi, G. Wang, H. Hwang, D.-Y. Kim and T. Lee, *Appl. Phys. Lett.*, 2008, **92**, 231.
44. J.-T. Wang, K. Saito, H.-C. Wu, H.-S. Sun, C.-C. Hung, Y. Chen, T. Isono, T. Kakuchi, T. Satoh and W.-C. Chen, *NPG Asia Mater.*, 2016, **8**, e298.
45. H.-C. Hsieh, C.-C. Hung, K. Watanabe, J.-Y. Chen, Y.-C. Chiu, T. Isono, Y.-C. Chiang,

R. R. Reghu, T. Satoh and W.-C. Chen, *Polym. Chem.*, 2018, **9**, 3820-3831.
46. D.-H. Jiang, S. Kobayashi, C.-C. Jao, Y. Mato, T. Isono, Y.-H. Fang, C.-C. Lin, T. Satoh, S.-H. Tung and C.-C. Kuo, *Polymers*, 2020, **12**, 84.
47. A.-N. Au-Duong, C.-C. Wu, Y.-T. Li, Y.-S. Huang, H.-Y. Cai, I. Jo Hai, Y.-H. Cheng, C.-C. Hu, J.-Y. Lai and C.-C. Kuo, *Macromolecules*, 2020, **53**, 4030-4037.
48. B. O'Connor, R. J. Kline, B. R. Conrad, L. J. Richter, D. Gundlach, M. F. Toney and D. M. DeLongchamp, *Adv. Funct. Mater.*, 2011, **21**, 3697-3705.
49. G. J. N. Wang, L. Shaw, J. Xu, T. Kurosawa, B. C. Schroeder, J. Y. Oh, S. J. Benight and Z. Bao, *Adv. Funct. Mater.*, 2016, **26**, 7254-7262.
50. S. Wang, J. Xu, W. Wang, G.-J. N. Wang, R. Rastak, F. Molina-Lopez, J. W. Chung, S. Niu, V. R. Feig and J. Lopez, *Nature*, 2018, **555**, 83.
51. A. D. Printz, S. Savagatrup, D. Rodriquez and D. J. Lipomi, *Sol. Energy Mater. Sol. Cells*, 2015, **134**, 64-72.
52. T. Kim, J.-H. Kim, T. E. Kang, C. Lee, H. Kang, M. Shin, C. Wang, B. Ma, U. Jeong and T.-S. Kim, *Nature communications*, 2015, **6**, 1-7.
53. W. Huang, Z. Jiang, K. Fukuda, X. Jiao, C. R. McNeill, T. Yokota and T. Someya, *Joule*, 2020, **4**, 128-141.
54. D. J. Lipomi, H. Chong, M. Vosgueritchian, J. Mei and Z. Bao, *Sol. Energy Mater. Sol. Cells*, 2012, **107**, 355-365.
55. L. Li, J. Liang, H. Gao, Y. Li, X. Niu, X. Zhu, Y. Xiong and Q. Pei, *ACS Appl. Mater. Interfaces*, 2017, **9**, 40523-40532.
56. J. Qin, L. Lan, S. Chen, F. Huang, H. Shi, W. Chen, H. Xia, K. Sun and C. Yang, *Adv. Funct. Mater.*, 2020, **30**, 2002529.
57. P. B. J. St. Onge, M. U. Ocheje, M. Selivanova and S. Rondeau-Gagné, *Chem. Rec.*, 2019, **19**, 1008-1027.
58. C.-C. Shih, W.-Y. Lee and W.-C. Chen, *Mater. Horiz.*, 2016, **3**, 294-308.
59. C.-L. Liu and W.-C. Chen, in *Electrical Memory Materials and Devices*, Royal Society of Chemistry, 2015, pp. 233-255.
60. Q.-D. Ling, D.-J. Liaw, C. Zhu, D. S.-H. Chan, E.-T. Kang and K.-G. Neoh, *Prog. Polym. Sci.*, 2008, **33**, 917-978.
61. Y.-C. Lai, Y.-C. Huang, T.-Y. Lin, Y.-X. Wang, C.-Y. Chang, Y. Li, T.-Y. Lin, B.-W. Ye, Y.-P. Hsieh and W.-F. Su, *NPG Asia Mater.*, 2014, **6**, e87.
62. C. Ban, X. Wang, Z. Zhou, H. Mao, S. Cheng, Z. Zhang, Z. Liu, H. Li, J. Liu and W. Huang, *Sci. Rep.*, 2019, **9**, 1-7.
63. K. Rajan, E. Garofalo and A. Chiolerio, *Sensors*, 2018, **18**, 367.
64. C. C. Hung, Y. C. Chiu, H. C. Wu, C. Lu, C. Bouilhac, I. Otsuka, S. Halila, R. Borsali, S. H. Tung and W. C. Chen, *Adv. Funct. Mater.*, 2017, **27**, 1606161.
65. C.-C. Hung, S. Nakahira, Y.-C. Chiu, T. Isono, H.-C. Wu, K. Watanabe, Y.-C. Chiang, S.

Takashima, R. Borsali and S.-H. Tung, *Macromolecules*, 2018, **51**, 4966-4975.
66. T. Iwata, *Angew. Chem. Int. Ed.*, 2015, **54**, 3210-3215.
67. S. M. Roopan, T. Surendra and G. Madhumitha, *Handbook of Polymers for Pharmaceutical Technologies; Wiley: Hoboken, NJ, USA*, 2015, **3**, 541-555.
68. R. P. Babu, K. O'connor and R. Seeram, *Progress in biomaterials*, 2013, **2**, 1-16.
69. V. Forti, C. P. Baldé, R. Kuehr, G. Bel, The Global E-Waste Monitor 2020: Quantities, Flows and the Circular Economy Potential, Bonn, Geneva, Rotterdam, 2020.
70. M. Irimia-Vladu, *Chem. Soc. Rev.*, 2014, **43**, 588-610.
71. K.-T. Huang, C.-C. Chueh and W.-C. Chen, Mater. Today Sustain., 2020, 100057.
72. C. J. Bettinger and Z. Bao, *Polym. Int.*, 2010, **59**, 563-567.
73. T. Lei, M. Guan, J. Liu, H.-C. Lin, R. Pfattner, L. Shaw, A. F. McGuire, T.-C. Huang, L. Shao and K.-T. Cheng, *Proc. Natl. Acad. Sci. U.S.A.,* 2017, **114**, 5107-5112.
74. J. W. Chang, C. G. Wang, C. Y. Huang, T. D. Tsai, T. F. Guo and T. C. Wen, *Adv. Mater.*, 2011, **23**, 4077-4081.
75. P. Stadler, K. Oppelt, T. B. Singh, J. G. Grote, R. Schwödiauer, S. Bauer, H. Piglmayer-Brezina, D. Bäuerle and N. S. Sariciftci, *Org. Electron.*, 2007, **8**, 648-654.
76. J.-Y. Lam, G.-W. Jang, C.-J. Huang, S.-H. Tung and W.-C. Chen, *ACS Sustain.Chem. Eng.*, 2020, **8**, 5100-5106.
77. K.-T. Huang, C.-C. Shih, B.-H. Jiang, R.-J. Jeng, C.-P. Chen and W.-C. Chen, *J. Mater. Chem. C*, 2019, **7**, 12572-12579.
78. K.-T. Huang, C.-P. Chen, B.-H. Jiang, R.-J. Jeng and W.-C. Chen, *Org. Electron.*, 2020, **87**, 105924.
79. R. Nie, A. Li and X. Deng, *J. Mater. Chem. A*, 2014, **2**, 6734-6739.
80. P.-C. Lin, Y.-T. Wong, Y.-A. Su, W.-C. Chen and C.-C. Chueh, *ACS Sustain. Chem. Eng.*, 2018, **6**, 14621-14630.
81. J. Dagar, M. Scarselli, M. De Crescenzi and T. M. Brown, *ACS Energy Lett.*, 2016, **1**, 510-515.
82. H. Liu, R. Jian, H. Chen, X. Tian, C. Sun, J. Zhu, Z. Yang, J. Sun and C. Wang, *Nanomaterials*, 2019, **9**, 950.
83. S. Bonardd, N. Morales, L. Gence, C. Saldías, F. A. Angel, G. Kortaberria and A. Leiva, *ACS Appl. Mater. Interfaces*, 2020, **12**, 13275-13286.
84. N. Maity and A. Dawn, *Polymers*, 2020, **12**, 709.
85. P. Cataldi, I. S. Bayer, F. Bonaccorso, V. Pellegrini, A. Athanassiou and R. Cingolani, *Adv. Electron. Mater.*, 2015, **1**, 1500224.
86. Y. Sakai-Otsuka, S. Zaioncz, I. Otsuka, S. Halila, P. Rannou and R. Borsali, *Macromolecules*, 2017, **50**, 3365-3376.
87. K. M. Zia, A. Noreen, M. Zuber, S. Tabasum and M. Mujahid, *Int. J. Biol. Macromol.*, 2016, **82**, 1028-1040.

88. C. J. Bettinger and Z. Bao, *Adv. Mater.*, 2010, **22**, 651-655.
89. G. Z. Papageorgiou, D. G. Papageorgiou, Z. Terzopoulou and D. N. Bikiaris, *Eur. Polym. J.*, 2016, **83**, 202-229.
90. S. K. Burgess, J. E. Leisen, B. E. Kraftschik, C. R. Mubarak, R. M. Kriegel and W. J. Koros, *Macromolecules*, 2014, **47**, 1383-1391.
91. J. Y. Lam, C. C. Shih, W. Y. Lee, C. C. Chueh, G. W. Jang, C. J. Huang, S. H. Tung and W. C. Chen, *Macromol. Rapid Commun.*, 2018, **39**, 1800271.
92. M. Labet and W. Thielemans, *Chem. Soc. Rev.*, 2009, **38**, 3484-3504.
93. I. Fortelny, A. Ujcic, L. Fambri and M. Slouf, *Front. Mater.*, 2019, **6**, 206.
94. T. Patrício, M. Domingos, A. Gloria and P. Bártolo, *Procedia Cirp*, 2013, **5**, 110-114.
95. F. Sugiyama, A. T. Kleinschmidt, L. V. Kayser, M. A. Alkhadra, J. M.-H. Wan, A. S.-C. Chiang, D. Rodriquez, S. E. Root, S. Savagatrup and D. J. Lipomi, *Macromolecules*, 2018, **51**, 5944-5949.
96. M. T. Martello, A. Burns and M. Hillmyer, *ACS Macro Lett.,* 2012, **1**, 131-135.
97. D. Tang, C. W. Macosko and M. A. Hillmyer, *Polym. Chem.*, 2014, **5**, 3231-3237.
98. D. K. Schneiderman, C. Gilmer, M. T. Wentzel, M. T. Martello, T. Kubo and J. E. Wissinger, *J. Chem. Educ.*, 2014, **91**, 131-135.
99. T. Isono, B. J. Ree, K. Tajima, R. Borsali and T. Satoh, *Macromolecules*, 2018, **51**, 428-437.
100. T. Isono, S. Nakahira, H.-C. Hsieh, S. Katsuhara, H. Mamiya, T. Yamamoto, W.-C. Chen, R. Borsali, K. Tajima and T. Satoh, *Macromolecules*, 2020, **53**, 5408-5417.
101. K. K. Bansal, D. Kakde, L. Purdie, D. J. Irvine, S. M. Howdle, G. Mantovani and C. Alexander, *Polym. Chem.*, 2015, **6**, 7196-7210.
102. R. Ferrari, A. Agostini, L. Brunel, L. Morosi and D. Moscatelli, *J. Polym. Sci., Part A: Polym. Chem.*, 2017, **55**, 3788-3797.
103. K. K. Bansal, J. Gupta, A. Rosling and J. M. Rosenholm, *Saudi. Pharm. J.*, 2018, **26**, 358-368.
104. T. Rali, S. W. Wossa and D. N. Leach, *Molecules*, 2007, **12**, 149-154.
105. Y. Gounaris, *Flavour. Fragr. J.*, 2010, **25**, 367-386.
106. K. Houk, A. Jabbari, H. Hall and C. Alemán, *J. Org. Chem.*, 2008, **73**, 2674-2678.
107. C. Aleman, O. Betran, J. Casanovas, K. Houk and H. Hall Jr, *J. Org. Chem.*, 2009, **74**, 6237-6244.
108. O. Coulembier, P. Degée, J. L. Hedrick and P. Dubois, *Prog. Polym. Sci.*, 2006, **31**, 723-747.
109. K. Makiguchi, T. Satoh and T. Kakuchi, *Macromolecules*, 2011, **44**, 1999-2005.
110. T. Isono, I. Otsuka, S. Halila, R. Borsali, T. Kakuchi and T. Satoh, *J. Photopolym. Sci. Technol.*, 2015, **28**, 635-642.
111. K. Saito, T. Isono, H.-S. Sun, T. Kakuchi, W.-C. Chen and T. Satoh, *Polym. Chem.*, 2015,

6, 6959-6972.

Chapter 2

Poly(3-hexylthiophene)-block-poly(δ-decanolactone)s: Toward High-Performance and Stretchable Semiconducting Material Through Branched Soft-Hard-Soft Type Triblock Copolymer Design

2.1 Background

In the development of stretchable electronic devices, one of the most challenging issues is to create a stretchable semiconducting materials.[1, 2] Conventional inorganic and small-molecule semiconducting materials could not meet the requirement for stretchable devices because of their brittle nature. Comparing to those counterparts, conjugated polymers are considered to be better alternatives for stretchable devices owing to their acceptable semiconducting properties and improved mechanical properties. However, due to the rigid polymer backbones, most of the conjugated polymers were still incapable of enduring strong mechanical strength for device applications.[3, 4]

To address this issue, one way is to incorporate rubber-like materials into the conjugated polymers to improve the stretchability of semiconductor thin film.[5, 6] In addition, controlling the regioregularity of the conjugated backbone[7, 8] or introducing flexible alkyl side chain[9, 10] could enhance the stretchability of conjugated polymers. Another useful approach is to synthesize conjugated block copolymers (BCPs) containing conjugated blocks and rubbery soft segments. The conjugated block possesses strong interchain π-π interaction to provide a conducting channel, and the insulating soft blocks to provide a degree of freedom for the movement of the polymer chain. For example, Chen and Satoh's research group prepared different kinds of linear diblock copolymers for stretchable electronic applications, such as polyfluorene-*block*-poly(pendent isoindigo) (PF-*b*-Piso),[11] poly(3-hexylthiophene)-*block*-

poly(*n*-butyl acrylate) (P3HT-*b*-PBA),[12] and polyfluorene-*block*-poly(*n*-butyl acrylate) (PF-*b*-PBA).[13] More recently, a hard-soft-hard type triblock copolymer, poly(3-hexylthiophene)-*block*-poly(octylene oxide)-*block*-poly(3-hexylthiophene) (P3HT-*b*-POO-*b*-P3HT) was designed for stretchable resistive memory applications.[14] The hard P3HT domains served as the physical crosslinking points linked with the soft segment in the middle of the polymer chain, which prevented the films from tearing apart under a high strain. Nevertheless, because of the incorporated insulating segments, the hard segment was separated and thus the π-conjugation of these polymers was interrupted, leading to lower charge mobilities from 10^{-4} to 10^{-3} $cm^2 V^{-1} s^{-1}$. To realize stretchable semiconductors with a high charge mobility using a hard-soft-hard architecture, the molecular weight of both soft and hard blocks must be increased, which may raise the difficulties for the polymer synthesis and the purification to remove the homopolymer impurities.[15-17] Therefore, it is essential to develop another synthetic and processing strategies for conjugated BCP to increase the stretchability of semiconducting block polymer without sacrificing its charge mobility.

In this study, I designed and synthesized a series of P3HT-based BCPs with different architectures, including AB, BAB, B_2AB_2, and B_3AB_3 (A: hard conjugated block, B: soft insulating block). The purpose of this architecture design is to tune the mechanical properties of the conjugated/insulating BCPs without breaking the conjugated block assembly. The soft-hard-soft polymer architecture was expected to be beneficial to confine the assembly of the

conjugated blocks through the microphase separation in the BCPs. On the other hand, the branched soft segments of poly(δ-decanolactone) (PDL) were introduced to tailor the crystallinity of conjugated block and the phase separation of BCP. Note that I chose PDL as the soft insulating building block of the target BCPs. PDL is an amorphous and bio-based polymer that can be derived from ring-opening polymerization of the bio-based δ-decanolactone monomer (δ-DL),[18, 19] which is thought to be a greener candidate for rubbery polymeric materials. Also, I adopted the diphenyl phosphate (DPP)-catalyzed ring-opening polymerization for the synthesis of PDL because it's a convenient, metal-free and nontoxic method for ring-opening polymerization[20] and it is applicable to delicate polymer architecture design.[21] Aside from the polymer design, solution process of the BCPs from different solvents including cyclohexane, THF and chloroform was conducted to achieve favorable thin-film morphology and to optimize the semiconducting property. Thin film morphologies and crystalline structure were studied by atom force microscope (AFM) and grazing incidence X-ray scattering (GIXS). Top contact organic field-effect transistors (OFETs) with the Si/SiO_2/polymer/Au structure were fabricated to examine the charge mobility of the prepared polymers. To evaluate the mechanical properties and stretchability of the polymer thin films, optical microscope (OM) and polarized-UV spectra of the stretched polymer films, and amplitude modulation-frequency modulation atomic force microscopy (AM-FM AFM) were performed. Finally, top contact OFETs with the stretched polymer thin films were fabricated to

discuss the effect of polymer architecture on the semiconducting property under strain.

2.2 Experimental Section

2.2.1 Materials

Tetrahydrofuran (THF, anhydrous, ≥99.9%), hydrochloric acid (HCl, 37%), methanol (anhydrous, 99.8%), dichloromethane (99.8%), toluene (≥99.8%), pyridine (99.8%), *n*-hexane (≥99%), cyclohexane (anhydrous, ≥99.5%), chloroform (≥99.9%), *tert*-butylmagnesium chloride solution (*t*-BuMgCl, 1.0 M in THF), tetra-*n*-butylammonium fluoride hydrate (TBAF, 98%), polydimethylsiloxane (PDMS, Sylgard 184), *N*,*N*,*N*',*N*'',*N*''-pentamethyldiethylenetriamine (PMDETA, 99%), copper(I) bromide (CuBr, 98%), and copper(I) iodide (CuI, 98%) were purchased from Sigma-Aldrich Co., Ltd. and used without purification. [1,3-Bis(diphenylphosphino)propane]nickel(II) dichloride (Ni(dppp)Cl_2), 2,5-dibromo-3-hexylthiophene (3HT) and *δ*-decanolactone (*δ*-DL, synthetic and racemic compound) were obtained from Tokyo Chemical Industry Co., Ltd.. 3HT and *δ*-DL were purified by distillation over CaH_2 before being used. Trimethylsilylacetylene (TMSA) was purchased from Shin-Etsu Chemical Co., Ltd. LiCl was purchased from Kanto Chemical Co., Inc. and dried overnight at 160 °C under high vacuum. 6-Azido-1-hexanol,[22] 2-[(6-azidohexyloxy)methyl]-2-methylpropane-1,3-diol, and 2-[(6-azidohexyloxy)methyl]-2-(hydroxymethyl)propane-1,3-diol[21] were synthesized following the previous reports.

2.2.2 Polymer Synthesis

The synthetic strategy for the target polymers is shown in **Scheme 2.1.** P3HT and PDL building blocks were prepared individually before the synthesis of the target BCPs. α-Functional and α,ω-bifunctional P3HTs with alkyne functional groups protected by trimethylsilyl (TMS) group (denoted as α-P3HT and α,ω-P3HT) were synthesized via the Kumada coupling reaction using a similar approach as previous report,[14] while the number averaged molecular weight was designed as 9k to provide enough conjugation for favorable charge transportation.[23, 24] Linear, two-armed, and three-armed PDLs with an azido functional group were synthesized via a living ring-opening polymerization. Diphenyl phosphate (DPP) was chose as a green catalyst, and azido functional alcohols with different number of hydroxyl groups were used as initiators[21] to prepare the PDL blocks with different structures. The BCPs with different architectures were then synthesized via Cu-catalyzed azido–alkyne click reaction (CuAAC) between alkyne functional P3HT and azido-functionalized PDL. The molecular weight of the prepared polymers was controlled precisely, which will be discussed in details later.

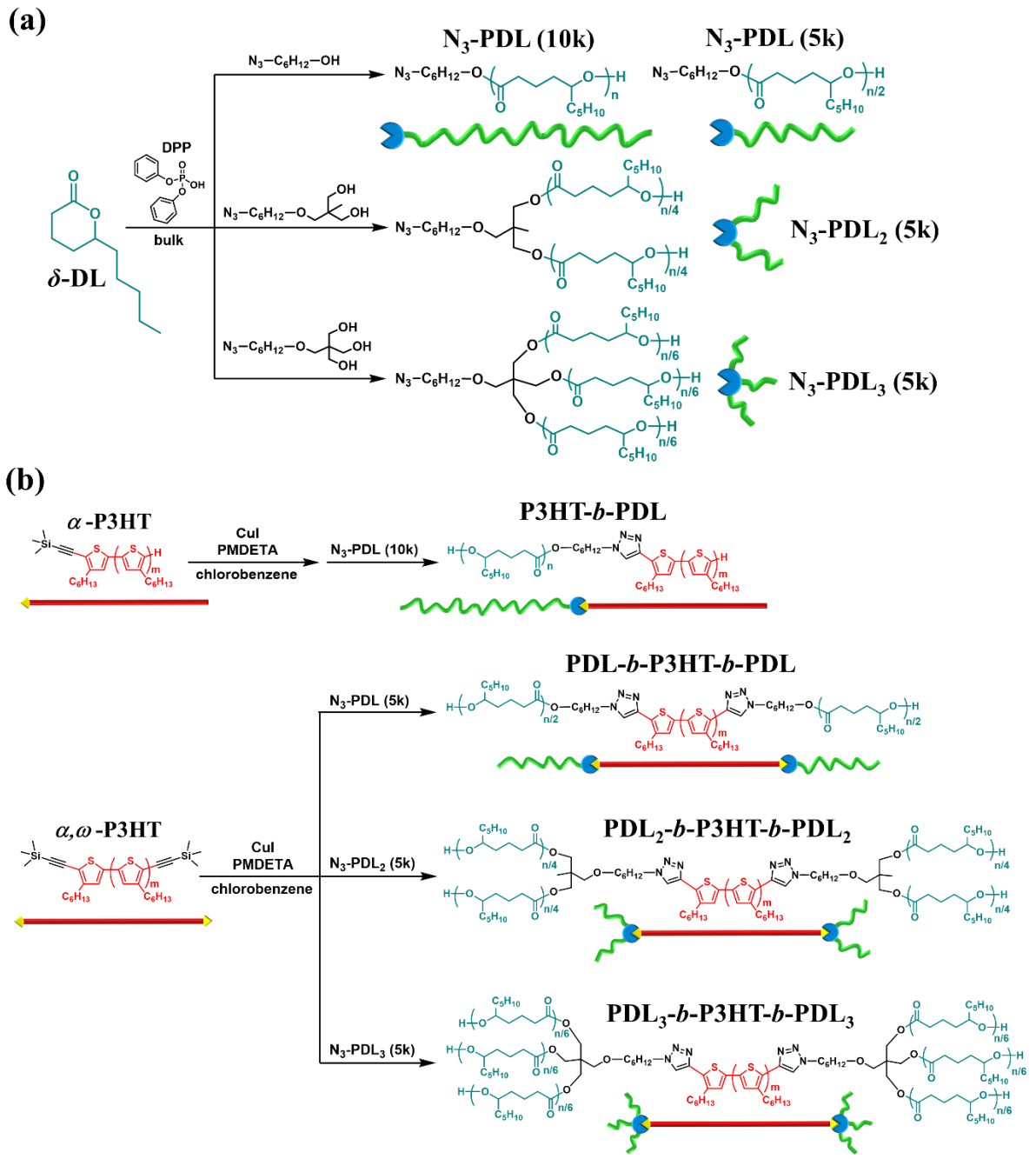

Scheme 2.1 Synthesis route for (a) linear, two-armed and three-armed azido functional PDLs, and (b) BCP series via click reaction between P3HTs and PDLs.

Synthesis of *α*-P3HT. The synthesis of P3HT were conducted in an argon-filled glove box. In a 20 ml vial were added the 3-hexylthiophene-2,5-diyl (2.00 g, 6.133 mmol), *t*-BuMgCl (1M in THF, 5425 mg, 5.827 mmol, 0.95 eq. to monomer), LiCl (263 mg, 6.195 mmol, 1.01

eq.), and THF (20 mL) and then stirred for at least 5 h. Then, Ni(dppp)Cl_2 (46 mg, 0.085 mmol, 0.0138 eq. to monomer) and THF (200 mL) were added into a 200 mL flask and stirred. Finally, the solution with the monomers and Grignard reagent was transferred into the flask to start polymerization. After 7 min, the reaction mixture was transferred out of glove box and quenched by adding 5M HCl. After removal of all the solvents by rotary evaporator, a short silica gel column was used to remove the metal catalyst. Next, the residue was dissolved in a little amount of THF and then poured into methanol. After vacuum filtration and washing with *n*-hexane, P3HT with bromide group at α position (α-bromo-P3HT) was obtained (540 mg, 27%).

Sonogashira reaction was then performed to introduce a TMS functional group at α position. α-bromo-P3HT (400mg, 44.4 μmol) was added into a 50 mL flask with CuBr (12.8 mg, 88.9 μmol, 2 eq. to P3HT), Pd(PPh_3)$_4$ (51.8 mg, 44.4 μmol, 1eq.), TMSA (437 mg, 4.44 mmol, 100 eq.), toluene (9 mL), and pyridine (3 ml). To totally remove oxygen, the reaction mixture was first purged with argon bubble for 30 min at room temperature, followed by three freeze-drying cycles. Finally, the reaction was conducted at 90°C for 2 days in argon environment. After reaction, the mixture was diluted by chloroform and purified by Al_2O_3 column to remove the copper catalyst. Then, the solution was washed by H_2O/diluted HCl for two times. The organic layer was collected and dried using Na_2SO_4. After evaporation, the solid part was dissolved in a little amount of THF and poured into MeOH to give pure α-P3HT (380

mg, 95%). ^{1}H NMR (400 MHz, $CDCl_3$, δ (ppm)): 6.98 (s, thiophene), 2.81 (t, thiophene-CH_2-), 1.80-1.65 (m, thiophene-CH_2-CH_2-), 1.51-1.25 (m, CH_3-(CH_2)$_3$-), 0.99-0.82 (m, -CH_3), and 0.26 (s, -Si-(CH_3)$_3$). $M_{n,NMR}$ (in $CDCl_3$) = 9000 g mol^{-1}, $M_{n,SEC}$ (in THF, calibrated with polystyrene standards) = 15000 g mol^{-1}, $Đ$= 1.10.

Synthesis of α,ω-P3HT. The synthesis of P3HT were conducted in an argon-filled glove box. In a 20 mL vial were added the 3-hexylthiophene-2,5-diyl (2.00 g, 6.133 mmol), *t*-BuMgCl (1M in THF, 5425 mg, 5.827 mmol, 0.95 eq. to monomer), LiCl (263 mg, 6.195 mmol, 1.01 eq.), and THF (20 mL) and then stirred for at least 5 h. Then, Ni(dppp)Cl_2 (46 mg, 0.085 mmol, 0.0138 eq. to monomer) and THF (200 mL) were added into a 200 ml flask and stirred. Finally, the solution with the monomers and Grignard reagent in the 20 mL vial was transferred into the flask to start polymerization. After 7 min, the reaction was quenched by a solution with TMSA (86 mg, 0.876 mmol, 0.143 eq.) and *t*-BuMgCl (816 mg, 0.876mmol, 10 eq.) in THF (15ml), which was also stirred for at least 5 h before using. The reaction mixture was then transferred out of glove box followed by removal of all the solvents by rotary evaporator. A short silica gel column was used to remove the metal catalyst. Next, the residue was dissolved by a little THF and then dropped in methanol. After vacuum filtration and washed by *n*-hexane, TMS-protected ω-alkynyl-functionalized P3HT (ω-P3HT) was obtained. (615mg, 31%)

Sonogashira reaction was then performed to introduce TMS functional group at α position. ω-P3HT (400mg, 44.9 μmol) was added into a 50mL flask with CuBr (12.9 mg, 89.9 μmol, 2

eq. to P3HT), $Pd(PPh_3)_4$ (51.9 mg, 44.9 μmol, 1eq.), TMSA (440 mg, 4.49mmol, 100 eq.), toluene (9 mL), and pyridine (3 mL). To totally remove oxygen, the reaction mixture was first purged with argon bubble for 30 min at room temperature, followed by three freeze-drying cycles. Finally, the reaction was conducted at 90°C for 2 days in argon environment. After reaction, the mixture was diluted by chloroform and purified by Al_2O_3 column to remove the copper catalyst. Then the solution was washed by H_2O/diluted HCl for two times. The organic layer was collected and dried using Na_2SO_4. After evaporation, the solid part was dissolved in a little amount of THF and poured into MeOH to give pure α,ω-P3HT product (376 mg, 94%). ^{1}H NMR (400 MHz, $CDCl_3$, δ (ppm)): 6.98 (s, thiophene), 2.81 (t, thiophene-CH_2-), 1.80-1.65 (m, thiophene-CH_2-CH_2-), 1.51-1.25 (m, CH_3-(CH_2)$_3$-), 0.99-0.82 (m, -CH_3), and 0.26 (s, -Si-(CH_3)$_3$). $M_{n,NMR}$ (in $CDCl_3$) = 8900 g mol^{-1}, $M_{n,\,SEC}$ (in THF, calibrated with polystyrene standards) = 14800 g mol^{-1}, $Đ$ = 1.13.

Synthesis of linear PDL (N_3-PDL (5k) and N_3-PDL (10k)). General procedure for the synthesis of N_3-PDL (5k) is described as below. In a glove box, δ-decanolactone (1.00 g, 5.87 mmol), DPP (16.3 mg, 0.065 mmol), and 6-azido-1-hexanol (18.7 mg, 0.131 mmol) were mixed in a vial and then closed by a cap. Then, the mixture was transferred out of glove box and heated at 40 °C to start polymerization. After 10 h and at the stage of 60%-70% conversion of the monomers, the mixture was cooled down to room temperature and diluted by dichloromethane. Finally, the mixture was purified by precipitation in methanol or dialysis to

remove unreacted monomer. After evaporation to remove the solvents, the dried product was viscous transparent liquid (720 mg, 72%). ^{1}H NMR (400 MHz, $CDCl_3$, δ (ppm)): 4.87 (m, main chain -CH_2-C*H*(C_5H_{11})O-), 4.06 (t, N_3-C_5H_{10}-C*H*$_2$-O-), 3.59 (s, chain end-CH_2C*H*(C_5H_{11})OH), 3.27 (t, N_3-C*H*$_2$-), 2.30 (m,-(C=O)C*H*$_2$$CH_2$-), 1.73-1.17 (m, -(C=O)$CH_2$C*H*$_2$C*H*$_2$CH(C*H*$_2$(C*H*$_2$)$_3$$CH_3$)O-, N_3-CH_2(C_4H_8)CH_2O-) , 0.88 ppm (t, -C*H*$_3$). $M_{n,NMR}$ (in $CDCl_3$) = 5060 g mol^{-1} , $M_{n,SEC}$ (in THF, calibrated with polystyrene standards) = 7100 g mol^{-1}, $Đ$ = 1.09.

Synthesis of N_3-PDL (10k) required less amount of DPP (22.9 mg, 0.091 mmol) and 6-azido-1-hexanol (9.3 mg, 0.065 mmol). The reaction took 40 h and the purification steps were the same as the synthesis of N_3-PDL (5k) (745mg, 75%). ^{1}H NMR (400 MHz, $CDCl_3$, δ (ppm)): 4.87 (m, main chain -CH_2-C*H*(C_5H_{11})O-), 4.06 (t, N_3-C_5H_{10}-C*H*$_2$-O-), 3.59 (s, chain end-CH_2C*H*(C_5H_{11})OH), 3.27 (t, N_3-C*H*$_2$-), 2.30 (m,-(C=O)C*H*$_2$$CH_2$-), 1.73-1.17 (m, -(C=O)$CH_2$C*H*$_2$C*H*$_2$CH(C*H*$_2$(C*H*$_2$)$_3$$CH_3$)O-, N_3-CH_2(C_4H_8)CH_2O-) , 0.88 ppm (t, -C*H*$_3$). $M_{n,NMR}$ (in $CDCl_3$) = 9900 g mol^{-1} , $M_{n,SEC}$ (in THF, calibrated with polystyrene standards) = 12600 g mol^{-1} , $Đ$ = 1.10.

Synthesis of two-armed PDL (N_3-PDL_2 (5k)). In a glove box, δ-decanolactone (1.00 g, 5.87 mmol), DPP (20.6 mg, 0.082 mmol), and 2-[(6-azidohexyloxy)methyl]-2-methylpropane-1,3-diol (28.8 mg, 0.117mmol) were mixed in a vial and then closed by a cap. Then the mixture was transferred out of glove box and heated at 40 °C to start polymerization. After 4 h and at

the stage of 60%-70% conversion of the monomers, the mixture was cooled down to room temperature and diluted by dichloromethane. Finally, the mixture was purified by precipitation in methanol or dialysis to remove unreacted monomer. The dried product was viscous transparent liquid (643 mg, 64%). ^{1}H NMR (400 MHz, $CDCl_3$, δ (ppm)): 4.87 (m, main chain -CH_2-C*H*(C_5H_{11})O-), 3.99 (s, -C(CH_3)(C*H*$_2$O-**PDL**)$_2$), 3.59 (s, chain end-CH_2C*H*(C_5H_{11})OH), 3.36 (t, N_3-C_5H_{10}C*H*$_2$O-), 3.31-3.22 (m, N_3C*H*$_2$$C_5H_{10}$OC*H*$_2$-), 2.30 (m,-(C=O)C*H*$_2$$CH_2$-), 1.73-1.17 (m, -(C=O)$CH_2$C*H*$_2$C*H*$_2$CH(C*H*$_2$(C*H*$_2$)$_3$$CH_3$)O-, -$N_3$-$CH_2$($C_4H_8$)$CH_2$O-) , 0.96 (s, -C(C*H*$_3$)((C*H*$_2$O-**PDL**)$_2$)), 0.88 (t, -C*H*$_3$). $M_{n,NMR}$ (in $CDCl_3$) = 5030 g mol^{-1} , $M_{n,SEC}$ (in THF, calibrated with polystyrene standards) = 6500 g mol^{-1} , $Đ$ = 1.08.

Synthesis of three-armed PDL (N_3-PDL_3 (5k)). In a glove box, δ-decanolactone (1.00 g, 5.87 mmol), DPP (14.7 mg, 0.059 mmol) and 2-[(6-azidohexyloxy)methyl]-2-(hydroxymethyl)propane-1,3-diol (30.7 mg, 0.117mmol) were mixed in a vial and then closed by a cap. Then, the mixture was transferred out of glove box and heated at 40 °C to start polymerization. After 4 h and at the stage of 60%-70% conversion of the monomers, the mixture was cooled down to room temperature and diluted by dichloromethane. Finally, the mixture was purified by precipitation in methanol or dialysis to remove unreacted monomer. After evaporation, the dried product was viscous transparent liquid (562 mg, 56%). ^{1}H NMR (400 MHz, $CDCl_3$, δ (ppm)): 4.87 (m, main chain -CH_2-C*H*(C_5H_{11})O-), 4.10 (s, -C(C*H*$_2$O-**PDL**)$_3$), 3.59 (s, chain end-CH_2C*H*(C_5H_{11})OH), 3.43-3.33 (m, N_3-C_5H_{10}C*H*$_2$OC*H*$_2$-), 3.30-3.24

(t, N_3CH_2), 2.30 (m,-(C=O)CH_2CH_2-), 1.73-1.17 (m, -(C=O)$CH_2CH_2CH_2CH(CH_2(CH_2)_3CH_3)$O-, N_3-$CH_2(C_4H_8)CH_2O$-) , 0.96 (s, -$C(CH_3)((CH_2O$-**PDL**$)_2)$), 0.88 (t, -CH_3). $M_{n,NMR}$ (in $CDCl_3$) = 5050 g mol^{-1} , $M_{n,SEC}$ (in THF, calibrated with polystyrene standards) = 6400 g mol^{-1} , $Đ$ = 1.14.

Synthesis of P3HT-*b*-PDL (AB). α-P3HT and N_3-PDL (10k) were used for the preparation of P3HT-*b*-PDL. A Schlenk flask was added P3HT (100 mg, 11.1 μmol) and CuI (10.6 mg, 55.6 μmol 5 eq. to P3HT). The mixture was dried under vacuum for more than 30 min, and then purged by argon. N_3-PDL (121 mg, 12.2 μmol, 1.1 eq. to the alkyne group on P3HT) and PMDETA (19.3 mg, 111.1 μmol, 10 eq. to P3HT) were mixed in a vial with chlorobenzene (5 mL), followed by three freeze-drying cycles to remove oxygen. Next, the PDL/PMDETA mixture was added into the Schlenk flask by a syringe. TBAF (1M in THF, 56 μL, 55.6 μmol, 5 eq. to P3HT) was added by the syringe to deprotect the TMS group in the P3HT and the reaction mixture was stirred at 80ºC for at least 12 h. The reaction mixture was filtered through a short Al_2O_3 column and the solvent was removed by evaporation. The dried mixture was dissolved in a little amount of THF and poured into methanol/acetone (2/1 to 3/1, v/v) to remove unreacted N_3-PDL. The unreacted P3HT homopolymer was then separated by preparative SEC using chloroform as eluent. Finally, the product was collected by precipitation again in methanol/acetone (95 mg, 43%). ^{1}H NMR (400 MHz, $CDCl_3$, δ (ppm)): 7.61 (s, thiazole), 6.98 (s, thiophene), 4.87 (m, main chain -CH_2-$CH(C_5H_{11})$O-), 4.06 (t, N_3-C_5H_{10}-CH_2-

O-), 3.59 (s, chain end-$CH_2CH(C_5H_{11})OH$), 3.27 (t, N_3-CH_2-), 2.81 (t, thiophene-CH_2-), 2.30 (m,-(C=O)CH_2CH_2-), 1.92-0.54 (aliphatic signal on **P3HT** and **PDL**). $M_{n,NMR}$ (in $CDCl_3$) = 19200 g mol^{-1} , $M_{n,SEC}$ (in THF, calibrated with polystyrene standards) = 29600 g mol^{-1} , $Đ$ = 1.12.

Synthesis of PDL-*b*-P3HT-*b*-PDL (BAB). The procedure was the same as the synthesis of P3HT-*b*-PDL. α,ω-P3HT (100 mg, 11.2 μmol) and N_3-PDL (5k) (125 mg, 24.7 μmol, 1.1 eq. to the alkyne group on P3HT) were used for the preparation of the BCP, and the rest of the other reagents were used with the same equivalent to P3HT. Preparative SEC was not required for purification steps due to perfect conversion of the click reaction. Yield: 175 mg (77%). ^{1}H NMR (400 MHz, $CDCl_3$, δ (ppm)): 7.61 (s, thiazole), 6.98 (s, thiophene), 4.87 (m, main chain -CH_2-$CH(C_5H_{11})$O-), 4.06 (t, N_3-C_5H_{10}-CH_2-O-), 3.59 (s, chain end-$CH_2CH(C_5H_{11})OH$), 3.27 (t, N_3-CH_2-), 2.81 (t, thiophene-CH_2-), 2.30 (m,-(C=O)CH_2CH_2-), 1.92-0.54 (aliphatic signal on **P3HT** and **PDL**). $M_{n,NMR}$ (in $CDCl_3$) = 18900 g mol^{-1} , $M_{n,SEC}$ (in THF, calibrated with polystyrene standards) = 26300 g mol^{-1} , $Đ$ = 1.17.

Synthesis of PDL_2-*b*-P3HT-*b*-PDL_2 (B_2AB_2). The procedure was the same as the synthesis of P3HT-*b*-PDL. α,ω-P3HT (100 mg, 11.2 μmol) and N_3-PDL_2 (5k) (124 mg, 24.7 μmol, 1.1 eq. to the alkyne group on P3HT) were used for the preparation of the BCP, and the rest of the other reagents were used with the same equivalent to P3HT. Preparative SEC was not required for purification steps due to perfect conversion of the click reaction. Yield: 185

mg (82%). ^{1}H NMR (400 MHz, $CDCl_3$, δ (ppm)): 7.61 (s, thiazole), 6.98 (s, thiophene), 4.87 (m, main chain -CH_2-C*H*(C_5H_{11})O-), 3.99 (s, -C(CH_3)(C*H*$_2$O-**PDL**)$_2$), 3.59 (s, chain end-CH_2C*H*(C_5H_{11})OH), 3.36 (t, N_3-C_5H_{10}C*H*$_2$O-), 3.31-3.22 (m, N_3C*H*$_2$$C_5H_{10}$OC*H*$_2$-), 2.81 (t, thiophene-C*H*$_2$-), 2.30 (m,-(C=O)C*H*$_2$$CH_2$-), 1.92-0.54 (aliphatic signal on **P3HT** and **PDL**). $M_{n,NMR}$ (in $CDCl_3$) = 18800 g mol^{-1} , $M_{n,SEC}$ (in THF, calibrated with polystyrene standards) = 25000 g mol^{-1} , $Đ$ = 1.19.

Synthesis of PDL$_3$-*b*-P3HT-*b*-PDL$_3$ (B$_3$AB$_3$). The procedure was the same as the synthesis of P3HT-*b*-PDL. *α,ω*-P3HT (100 mg, 11.2 μmol) and N_3-PDL_3 (5k) (125 mg, 24.7 μmol, 1.1 eq. to the alkyne group on P3HT) were used for the preparation of the BCP, and the rest of the other reagents were used with the same equivalent to P3HT. Preparative SEC was not required for purification steps due to perfect conversion of the click reaction. Yield: 176 mg (80%). ^{1}H NMR (400 MHz, $CDCl_3$, δ (ppm)): 7.61 (s, thiazole), 6.98 (s, thiophene), 4.87 (m, main chain -CH_2-C*H*(C_5H_{11})O-), 4.10 (s, -C(C*H*$_2$O-**PDL**)$_3$), 3.59 (s, chain end-CH_2C*H*(C_5H_{11})OH), 3.43-3.33 (m, N_3-C_5H_{10}C*H*$_2$OC*H*$_2$-), 3.30-3.24 (t, N_3C*H*$_2$), 2.81 (t, thiophene-C*H*$_2$-), 2.30 (m,-(C=O)C*H*$_2$$CH_2$-), 1.92-0.54 (aliphatic signal on **P3HT** and **PDL**). $M_{n,NMR}$ (in $CDCl_3$) = 18800 g mol^{-1} , $M_{n,SEC}$ (in THF, calibrated with polystyrene standards) = 24800 g mol^{-1} , $Đ$ = 1.16.

2.2.3 Characterization

Polymer structure characterization. ^{1}H NMR spectra were recorded by a JEOL JNM-ECS400 using deuterated chloroform as d-solvent. Size exclusion chromatography (SEC) measurement of the polymers were performed at 40 °C using a Jasco GPC-900 system equipped with two Shodex KF-804L columns (8 mm × 300 mm), where THF was used as the eluent solvent at a flow rate of 1.0 mL min^{-1}. Number-average molecular weight ($M_{n,SEC}$) and dispersity ($Đ$) of the studied polymers were calculated on the basis of a polystyrene standard. Fourier transform infrared spectroscopy (FT-IR) analysis was studied by a PerkinElmer Frontier MIR spectrometer equipped with a single reflection diamond universal attenuated total reflection (ATR) accessory.

Thermal Properties. Thermal gravimetric analysis (TGA) was performed through a TA Instruments Q50 with a heating rate of 10 °C min^{-1} from 100 °C to 800 °C under nitrogen flow. Differential scanning calorimetry (DSC) analysis were performed by a TA Instruments Q100 in which 3-5 mg of samples were heated at a rate of 10 °C min^{-1} from -90 °C to 270 °C.

Optical, Electrical Properties and Thin Film Morphology. All the thin film samples were prepared by spin-coating of polymer solution (3g L^{-1}) on top of bare silicon wafer, quartz substrate or ITO glass depending on requirements. The Si substrates were modified with octadecyltrichlorosilane (ODTS) self-assembled monolayers according to the reported method

to enhance the orientation and molecular packing of the studied polymer thin films.[25] The annealing process for polymer thin film was carried out at 140 °C under vacuum for 20 min. The samples for solution-state UV-vis absorption spectra were prepared by polymer solution with the concentration of 0.025 g L^{-1}. For the polymer solution in cyclohexane, the solution in a 4ml vial was settled inside an aluminum heat block insert and was heated on a hot plate at 90ºC for 10 minutes to ensure the uniform heating of the solution. After heating, the polymer solution with light orange color was removed from the hotplate and quickly transferred to the quartz cell by a glass Pasteur pipette, and then settled in the UV machine. Solution and solid-state UV absorption spectra were recorded by a Hitachi U4100 spectrometer. Cyclic voltammetry (CV) was measured by a CHI 627E electrochemical analyzer using a three-electrode cell system, where an ITO glass was used as working electrode and a platinum wire was used as auxiliary electrode. The Ag/AgCl, KCl (sat.) reference electrode was used to define the cell potential. The electrochemical properties of the polymer films were measured using 0.1 M tetrabutylammonium perchlorate in anhydrous acetonitrile as the electrolyte. The nanostructure of polymer thin films was visualized with a HITACHI AFM5000II operated in the tapping mode under ambient atmosphere, and the cantilever was SI-DF40 with the spring constant of 15 N m^{-1} and the frequency of 271 kHz. Synchrotron grazing incidence X-ray scattering (GIXS) measurements of the unstretched polymer films were carried out at the 3C beamline of Pohang Accelerator Laboratory (PAL). The GIXS measurements were conducted

at room temperature by using an X-ray radiation source of λ = 1.2296 Å and a two-dimensional (2D) charge-coupled detector (CCD) (model Rayonix 2D SX 165, Rayonix, Evanston, IL, USA). The incidence angle of X-ray beam with respect to polymer film plane was set in the range of 0.12°-0.15°.

Mechanical Properties and Strain-aligned Morphology of the Polymer Thin Films. For optical microscopy (OM) and polarized-UV measurements of the stretched polymer films, the films were first transferred from the ODTS-modified wafer to the PDMS elastomer, and then were stretched at different loadings and clamped onto glass substrates. OM images were acquired from an OLYMPUS BX51. Polarized-UV absorption was recorded by a Hitachi U-4100 spectrometer with the polarized light parallel and perpendicular to the strain direction. Dichroic ratio was calculated by the ratio of the absorbance of the film with parallel light to the absorbance with perpendicular light at the peak absorption wavelength of the parallel polarized light. Elastic modulus of polymer thin films was studied by the amplitude modulation-frequency modulation (AM-FM) viscoelastic mapping technique using a generalized Hertz model.[26-28] The experiments were kindly supported by Oxford Instruments Nihombashi Lab, Tokyo, Japan using their Cypher ES AFM, and the cantilever was Biosphere B30 (Nanotools USA LLC) with radius of 32 nm and Poisson's ratio of 0.36.

Device Fabrication. Bottom-gate-top-contact organic field-effect transistors (OFETs) with the Si/SiO_2/polymer/Au configuration were fabricated to evaluate the electrical properties

of the studied polymers. The polymer thin films with a thickness around 40 nm were spin-coated onto the ODTS-modified SiO_2 (300nm)/Si substrates followed by annealing process at 140 ºC for 20 min. 60 nm-thick gold source and drain electrodes were then subsequently thermal evaporated through a regular shadow mask with channel length (L) and width (W) of 50 and 1000 μm, respectively. For the OFET prepared from the stretched polymer thin films (depicted in **Fig. 2.1**), the thermally annealed polymer thin films developed on the ODTS-modified SiO_2/Si substrates were first transferred to a PDMS substrate (reagent A:B = 14:1 (w/w)). Next, the polymer films on PDMS substrate were stretched at different strain levels and clamped on a glass substrate. The polymer films were then transferred on a silicon wafer with 300 nm SiO_2 layer. Finally, gold source and drain electrodes with 60 nm thickness were developed by thermal evaporation through the shadow mask with channel length (L) and width (W) of 50 and 1000 μm. The fabrication process of the devices is summarized and illustrated in Fig. S1 (*Supporting Information*, *SI*). Current-Voltage characteristics (I_{ds}-V_g) of the fabricated OFETs were recorded in a N_2-filled glovebox using a Keithley 4200 semiconductor parametric analyzer (Keithley Instruments Inc., Cleveland, OH).

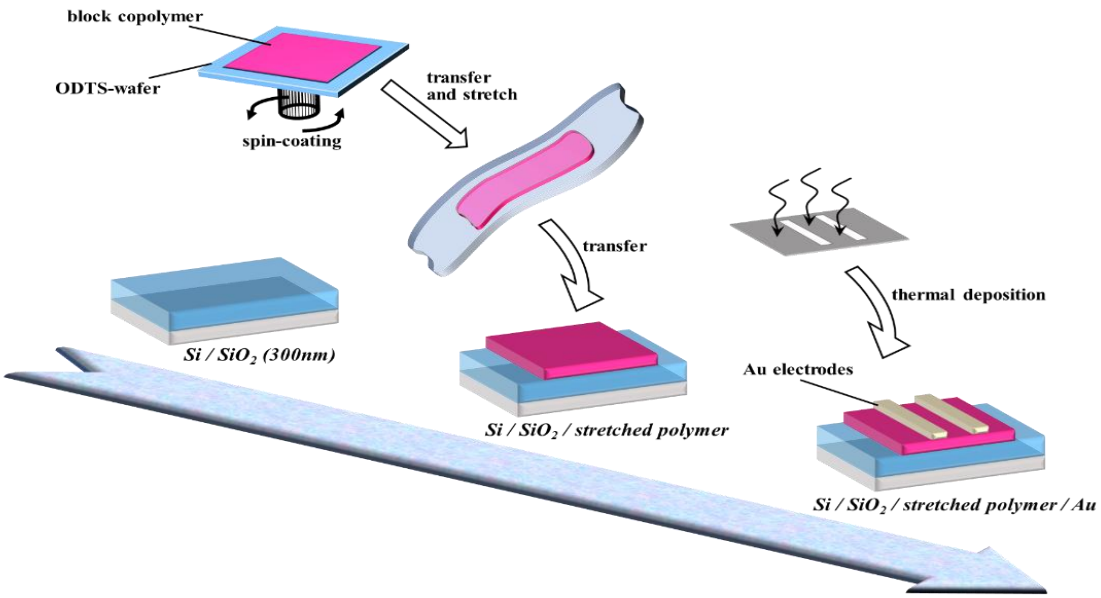

Fig. 2.1 The illustration of the fabrication of field-effect transistor devices with the stretched and transferred polymer film as the semiconducting layer.

2.3 Results and Discussion

2.3.1 Polymer Characterization

The information of molecular weight, dispersity ($Đ$), and composition of the studied polymer are summarized in **Table 2.1.** α-P3HT and α,ω-P3HT with controlled molecular weights were successfully prepared by the Kumada coupling followed by the Sonogashira reaction. ^{1}H NMR spectra of the P3HTs are provided in **Fig. 2.2a**. MALDI-TOFF mass spectra of α-P3HT (**Fig. 2.2b**) and α,ω-P3HT (**Fig. 2.2c**) show a periodic peak pattern with an interval of m/z of 166 and without any significant minor peak, suggesting the successful end-functionalization of the P3HTs. Number-averaged molecular weight calculated by ^{1}H NMR ($M_{n,NMR}$) of α-P3HT and α,ω-P3HT are 9000 and 8900, respectively, and the $Đ$ value is 1.10 and 1.13. The ^{1}H NMR spectra of N_3-PDL (10k), N_3-PDL (5k), N_3-PDL_2 (5k), and N_3-PDL_3 (5k) synthesized by a living ring-opening polymerization with a DPP catalyst are shown in **Fig. 2.3**. $M_{n,NMR}$ of each sample is precisely controlled and $Đ$ values ranged from 1.08 to 1.14. These results suggest that the prepared homopolymers could be used as the building blocks of the desired P3HT-*b*-PDL BCPs.

Table 2.1 Molecular characteristics of the studied polymers.

sample	$M_{n,NMR}$ [a]	$M_{n,SEC}$ [b]	$Đ$ [b]	w_{P3HT} [a] (%)	E_g [c] (eV)	HOMO [d] (eV)	LUMO [e] (eV)
α-P3HT	9000	15000	1.10	100%	-	-	-
α,ω-P3HT	8900	14800	1.13	100%	1.93	-4.94	-3.02
N_3-PDL (10k)	9900	12600	1.10	0%	-	-	-
N_3-PDL (5k)	5060	7100	1.09	0%	-	-	-
N_3-PDL_2 (5k)	5030	6500	1.08	0%	-	-	-
N_3-PDL_3 (5k)	5050	6400	1.14	0%	-	-	-
P3HT-*b*-PDL	19200	29600	1.12	47.6%	1.93	-4.95	-3.02
PDL-*b*-P3HT-*b*-PDL	18900	26300	1.17	46.8%	1.93	-4.95	-3.02
PDL_2-*b*-P3HT-*b*-PDL_2	18800	25000	1.19	46.9%	1.93	-4.95	-3.02
PDL_3-*b*-P3HT-*b*-PDL_3	18800	24800	1.16	46.8%	1.92	-4.95	-3.03

[a] Determined by ^{1}H NMR in $CDCl_3$. [b] Determined by SEC in THF based on a polystyrene calibration. [c] Determined from the absorption onset of the spin-cast film from chloroform solution on quartz. [d] Calculated from the onset oxidation potential measured by CV. [e] Calculated using the formula of LUMO = HOMO + E_g.

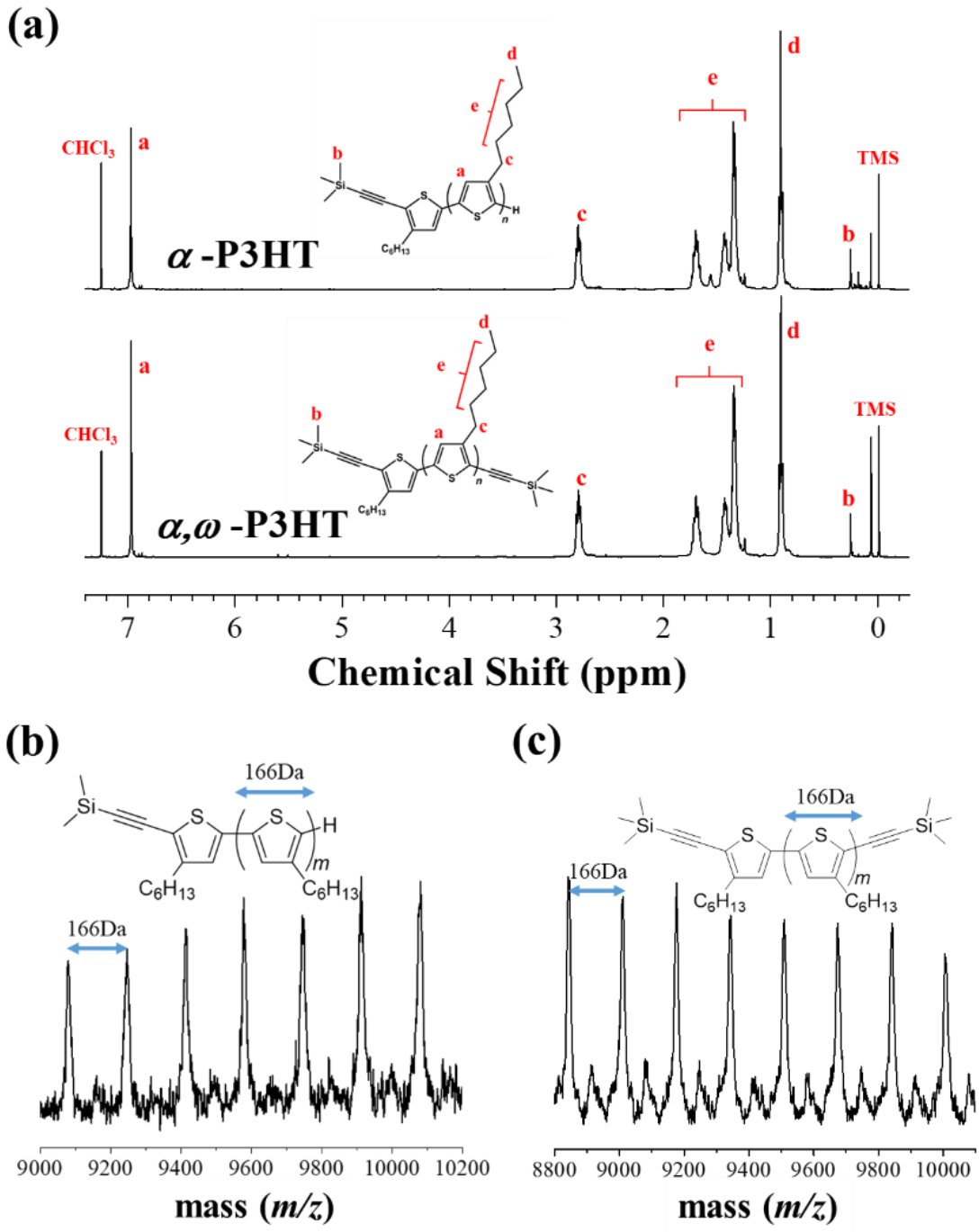

Fig. 2.2 (a) ^{1}H NMR spectra of α-P3HT and α,ω-P3HT (in $CDCl_3$). MALDI-TOF mass spectra of (b) α-P3HT and (c) α,ω-P3HT.

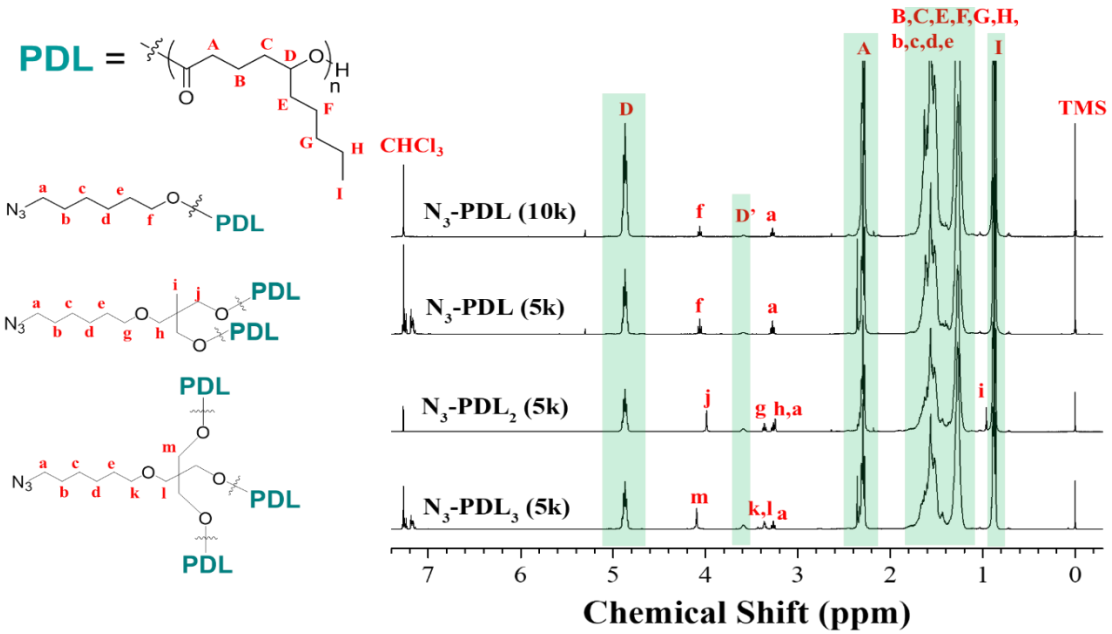

Fig. 2.3 ^{1}H NMR spectra of PDL homopolymers (in $CDCl_3$).

The click reactions were performed at 80 °C using chlorobenzene as solvent since chlorobenzene was a good solvent for both P3HT and PDL and its high boiling point (132 °C) is beneficial for performing the reaction at elevated temperature. SEC traces of P3HT-*b*-PDL and its homopolymer (**Fig. 2.4a**) show that the elution peak clearly shifted to a higher molecular weight region upon the click reaction, indicating the formation of the BCP. However, the residual α-P3HT is found in the SEC trace (**Fig. 2.4a**, orange curve) after removing excess amount of N_3-PDL by precipitation. This phenomenon is common in the synthesis of BCPs with a high molecular weight via CuAAC owing to the poor solubility of polymers and low miscibility between two blocks with high molecular weights. Therefore, the preparative SEC is required to remove the unreacted α-P3HT and to collect the pure product (**Fig. 2.4a**, black

curve). In the synthesis of PDL-*b*-P3HT-*b*-PDL, on the contrary, the SEC trace of the product after precipitation (**Fig. 2.4b**, black curve) does not show any significant peak representing the unreacted α,ω-P3HT, indicating the click reaction between two blocks is completed. The SEC traces of PDL_2-*b*-P3HT-*b*-PDL_2 and PDL_3-*b*-P3HT-*b*-PDL_3 (**Fig. 2.4c and d**) also suggest high conversion of the click reaction. This result indicates that the triblock copolymers (PDL-*b*-P3HT-*b*-PDL, PDL_2-*b*-P3HT-*b*-PDL_2, and PDL_3-*b*-P3HT-*b*-PDL_3) can be more efficiently prepared by the click reaction with a high yield comparing to their linear diblock copolymer counterpart (P3HT-*b*-PDL). It is probably due to the higher solubility of the low-molecular-weight PDLs and the improved miscibility of P3HT and PDL. Chemical structure of the BCPs was then characterized by FTIR and ^{1}H NMR spectra. For the synthesis of P3HT-*b*-PDL, FTIR spectra of the BCPs (**Fig. 2.5**) show that the absorption band representing the alkyne group from α-P3HT (2138 cm^{-1}) and azido group from N_3-PDL (2097 cm^{-1}) disappears after the click reaction, indicating the effective coupling between the alkyne and azido groups. ^{1}H NMR spectrum of each of the BCP (**Fig. 2.6**) exhibits the signals from the both P3HT and PDL building blocks, along with two additional peaks at 7.61 ppm and 4.18 ppm, which indicate the proton on the triazole group and the two protons on the adjacent carbon, respectively. These results ensure that the target BCPs were successfully prepared. To the best of our knowledge, this work is the first example of the synthesis on the dumbbell type triblock copolymer (B_2AB_2 and B_3AB_3) containing conjugated polymer in the middle.

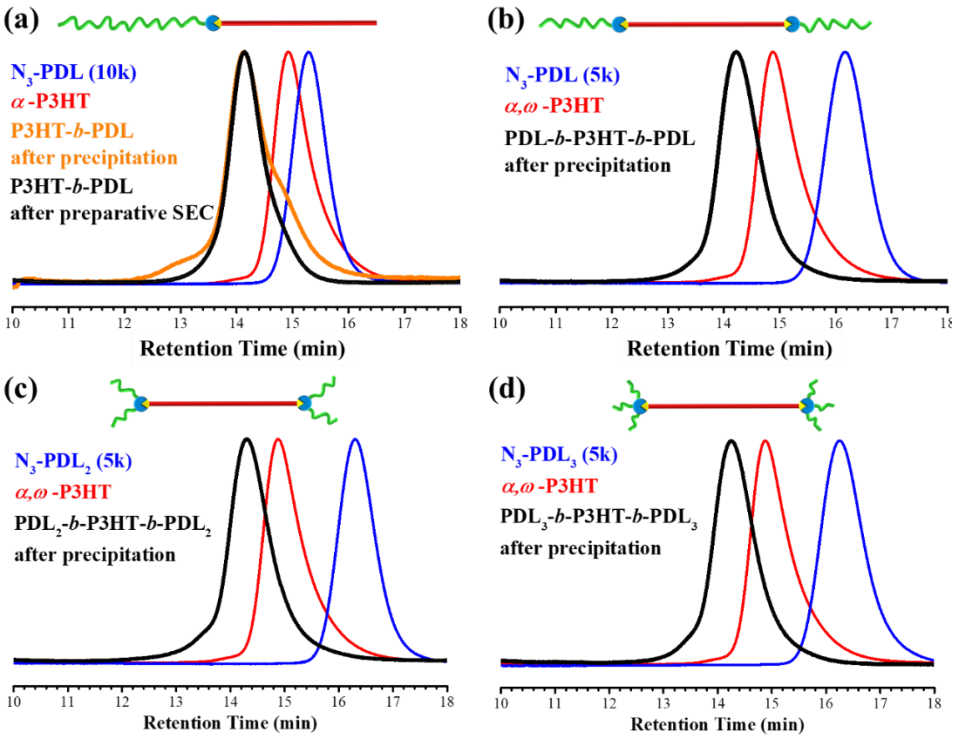

Fig. 2.4 SEC traces of (a) P3HT-*b*-PDL, (b) PDL-*b*-P3HT-*b*-PDL, (c) PDL_2-*b*-P3HT-*b*-PDL_2 and (b) PDL_3-*b*-P3HT-*b*-PDL_3 and their starting materials.

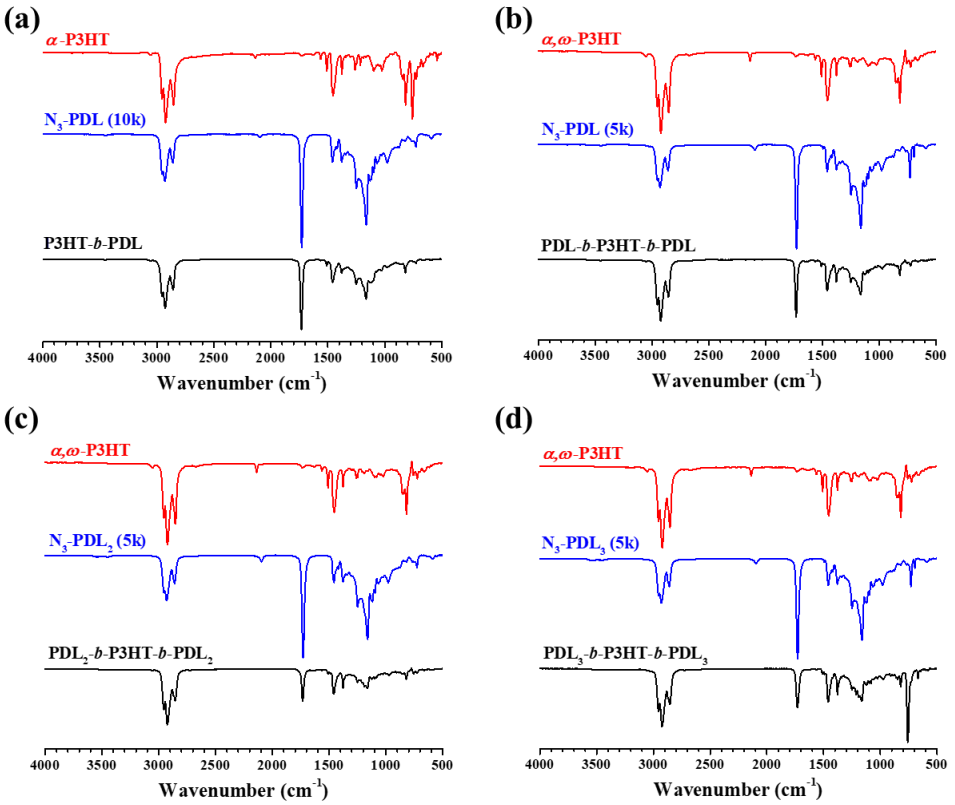

Fig. 2.5 FTIR spectra of (a) P3HT-*b*-PDL, (b) PDL-*b*-P3HT-*b*-PDL, (c) PDL_2-*b*-P3HT-*b*-PDL_2 and (d) PDL_3-*b*-P3HT-*b*-PDL_3 and their starting materials.

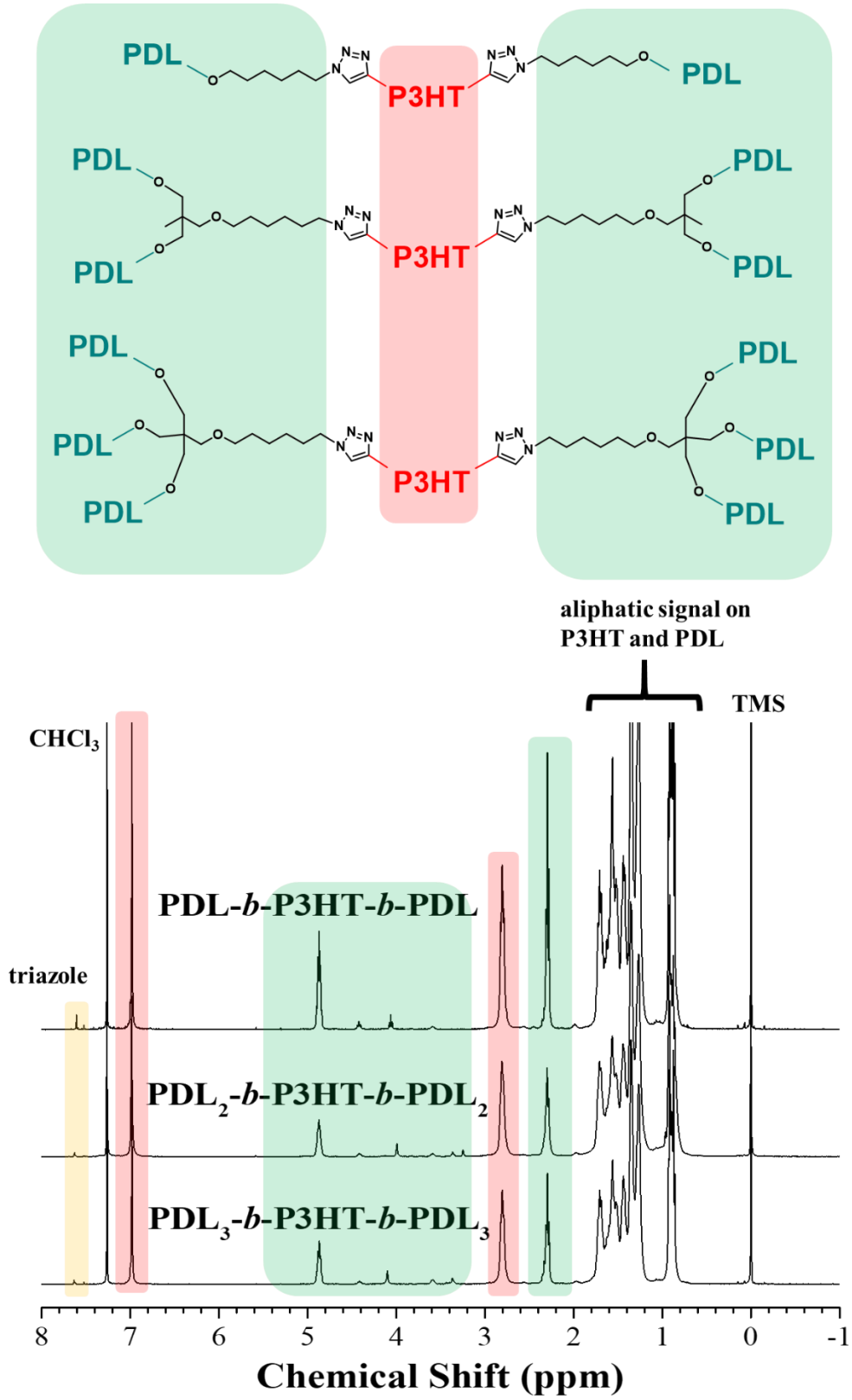

Fig. 2.6 ^{1}H NMR spectra of (a) P3HT-*b*-PDL, (b) PDL-*b*-P3HT-*b*-PDL, (c) PDL_2-*b*-P3HT-*b*-PDL_2 and (d) PDL_3-*b*-P3HT-*b*-PDL_3 and their starting materials.

In summary, I have prepared BCPs with the AB, BAB, B_2AB_2 and B_3AB_3 architecture (A: P3HT, B: PDL) with a narrow *Đ* (1.12, 1.17, 1.19 and 1.16, respectively). Also, the molecular weights of P3HT and PDL blocks in one polymer chain are controlled at 9000 and 10000, respectively, and the compositions of P3HT by weight in the BCPs is between 46.8% and 47.6%. In this case, the relationships between the architecture of BCPs and their properties can be discussed without any other possible effect derived from the difference in the A/B block ratios.

2.3.2 Thermal Properties

Thermal properties of the bulk polymer samples were studied by TGA and DSC**.** Two-step thermal degradation behavior is observed in all the BCPs, in which the first (range from 302 ºC to 318 ºC) and second degradation (around 435 ºC) corresponded to the PDL and P3HT blocks, respectively (**Fig. 2.7**). Note that the first degradation temperature ($T_{d\,95\%}$) of the AB, BAB, B_2AB_2 and B_3AB_3 type BCPs are 318 ºC, 311 ºC, 301 ºC and 302 ºC, respectively, suggesting that the triblock copolymers with branched PDL segments possess relatively lower thermal stability. The polyesters made by the ring-opening polymerization of cyclic esters (lactones and lactides) are thought to be thermally decomposed through a nucleophilic attack at the carbonyl carbon by the hydroxyl group at polymer chain end.[29, 30] Therefore, the highly branched BCP with a shorter PDL chain length and a higher hydroxyl group content could be

thermally decomposed more easily comparing to the linear BCP counterparts. In the DSC first cooling curves (**Fig. 2.8a**), the crystallization enthalpy of P3HT segments in P3HT-*b*-PDL, PDL-*b*-P3HT-*b*-PDL, PDL_2-*b*-P3HT-*b*-PDL_2, and PDL_3-*b*-P3HT-*b*-PDL_3 are 26.5, 29.6, 29.4 and 28.5 J g^{-1}, respectively, which show no significant difference depending on the polymer architecture. In the second heating curve (**Fig. 2.8b**), the bimodal melting peaks of the BCPs are observed, which is associated with the melt-recrystallize-melt process of semicrystalline polymers.[31-33] This phenomenon was also reported in a previous study on P3HT-containing miktoarm star copolymers.[34] The first melting peaks (T_m) of P3HT-*b*-PDL, PDL-*b*-P3HT-*b*-PDL, PDL_2-*b*-P3HT-*b*-PDL_2, and PDL_3-*b*-P3HT-*b*-PDL_3 are observed at 216.5, 208.6, 203.3 and 203.8ºC, respectively, and the second melting peaks of P3HT-*b*-PDL, PDL-*b*-P3HT-*b*-PDL, PDL_2-*b*-P3HT-*b*-PDL_2, and PDL_3-*b*-P3HT-*b*-PDL_3 are assigned to be at 238.3, 227.7, 220.0, and 220.6ºC, respectively. It suggests that T_m could be lowered not only by introducing the triblock architecture,[35] but also by introducing the branched soft segments. The smaller T_m of the branched polymers (PDL_2-*b*-P3HT-*b*-PDL_2 and PDL_3-*b*-P3HT-*b*-PDL_3) may be due to the more disarranged packing and the smaller crystallite size of P3HT affected by the branched soft segments.[34] Moreover, the higher intensity of the second melting peaks of the triblock copolymers (PDL-*b*-P3HT-*b*-PDL, PDL_2-*b*-P3HT-*b*-PDL_2, and PDL_3-*b*-P3HT-*b*-PDL_3) indicates the stronger crystallization behavior of the P3HT block[33] comparing to that of the linear diblock copolymer (P3HT-*b*-PDL). The crystallinity of the bulk polymer samples was

calculated by the enthalpy of fusion (ΔH_m) in the second heating curves (**Fig. 2.8b**). The enthalpy of fusion of the perfect P3HT crystal (ΔH_m^o) derived from the modified Flory's approach is 76J/g.[36] Therefore, the calculated P3HT crystallinity (X_{P3HT}) of α,ω-P3HT, PDL-*b*-P3HT-*b*-PDL, PDL_2-*b*-P3HT-*b*-PDL_2, and PDL_3-*b*-P3HT-*b*-PDL_3 are 28.4%, 31.2%, 35.0%, 33.4%, 32.2%, respectively. The results suggest that all the BCP possess a higher X_{P3HT} than the pristine P3HT. Also, the triblock copolymers (BAB, B_2AB_2 and B_3AB_3) exhibit a higher X_{P3HT} than the diblock copolymer (AB), indicating the benefit of triblock architecture for the crystallization of P3HT. Moreover, B_2AB_2 and B_3AB_3 type polymers possess a relatively lower X_{P3HT} than BAB type polymer which may be due to the interrupted assembly of P3HT at the P3HT/PDL interfaces, since branched architecture could provide higher surface curvature between the P3HT and PDL blocks. DSC studies provide an important insight about how the crystallization process of the hard segment in the BCP could be tuned by the structure of the neighbored soft segment, which is useful for the structural design of BCP to tune its thermal and mechanical properties.

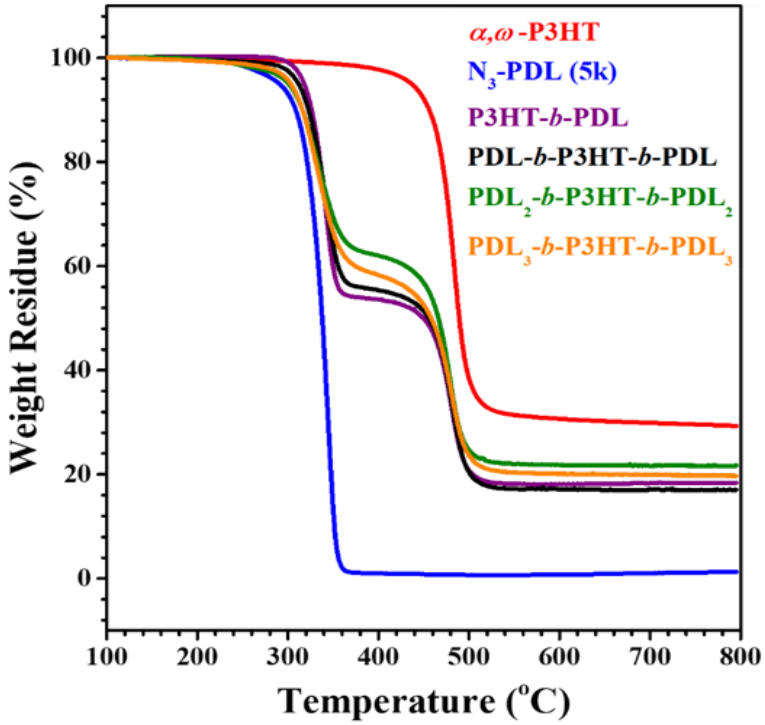

Fig. 2.7 TGA traces of the studied polymers.

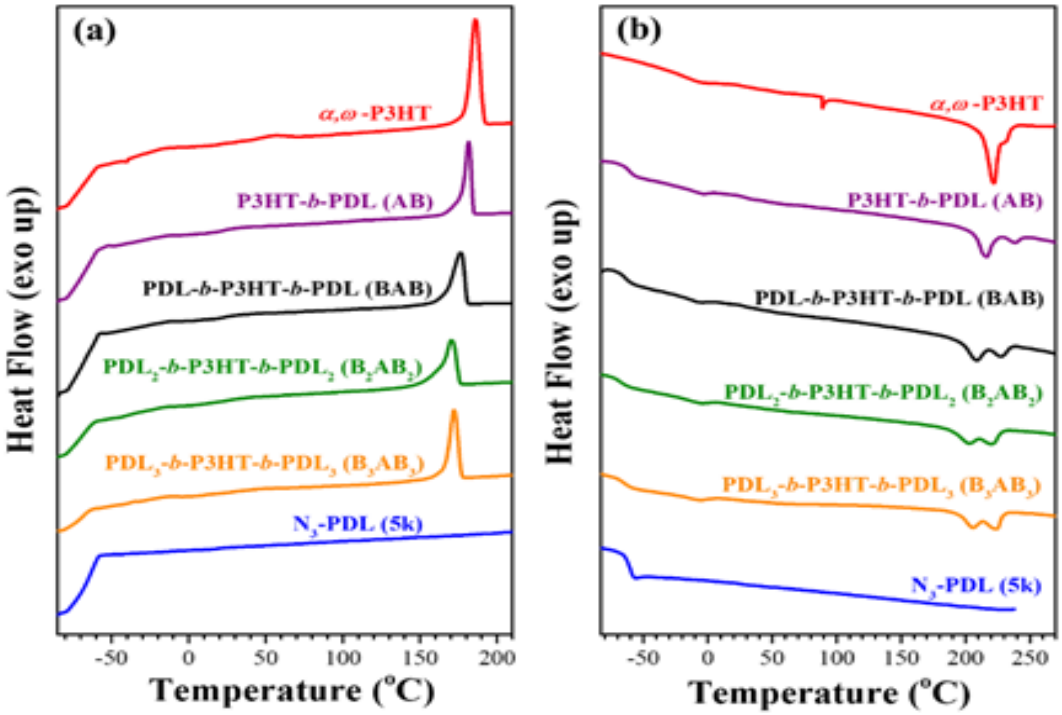

Fig. 2.8 DSC traces of the studied polymers during (a) 1st cooling and (b) 2nd heating processes.

2.3.3 Selective Solvent Process Versus Optical and Electrochemical Properties

Selective solvent process and optical properties. In the development of high-performance organic-based electronic devices, the processing solvent is also an important issue apart from the material design. In this study, the thin film properties and device performance of the BCPs using different solvents including cyclohexane, chloroform and THF were examined. The results suggest that the selective solvent that favored the soft segment (cyclohexane in this study) was beneficial to the solution process of the BCPs. It is known that conjugated polymers are generally soluble in a few of non-polar organic solvents such as chloroform, THF, toluene and chlorobenzene. In this research, the introduction of PDL segment to conjugated BCP helps to improve solution processibility of polymer. Cyclohexane is a representative non-polar solvent with low P3HT solubility (0.058 g L^{-1}),[37] but it can easily dissolve PDL. Therefore, it is a "selective solvent" for PDL segment in our BCPs. Aside from cyclohexane, chloroform and THF were used for comparison since they are regarded as "good solvents" for both P3HT and PDL segments, and they are common solvents for solution process of P3HT. The prepared BCPs were partially soluble in cyclohexane at room temperature, but they were totally dissolved after heating up to 90 °C. As can be seen in **Fig. 2.9a**, the polymer solution with concentration of 3 g L^{-1} after heating at 90 °C shows an orange color, indicating that the P3HT chains in the BCP are well swollen in the solution without precipitation. After

cooling down to room temperature, the aggregates of P3HT starts to grow in the solution and thus the color of the polymer solution becomes darker. The heating and cooling processes are reversible and steady thus the aggregation of P3HT segment could be controlled right before the following spin-coating process.

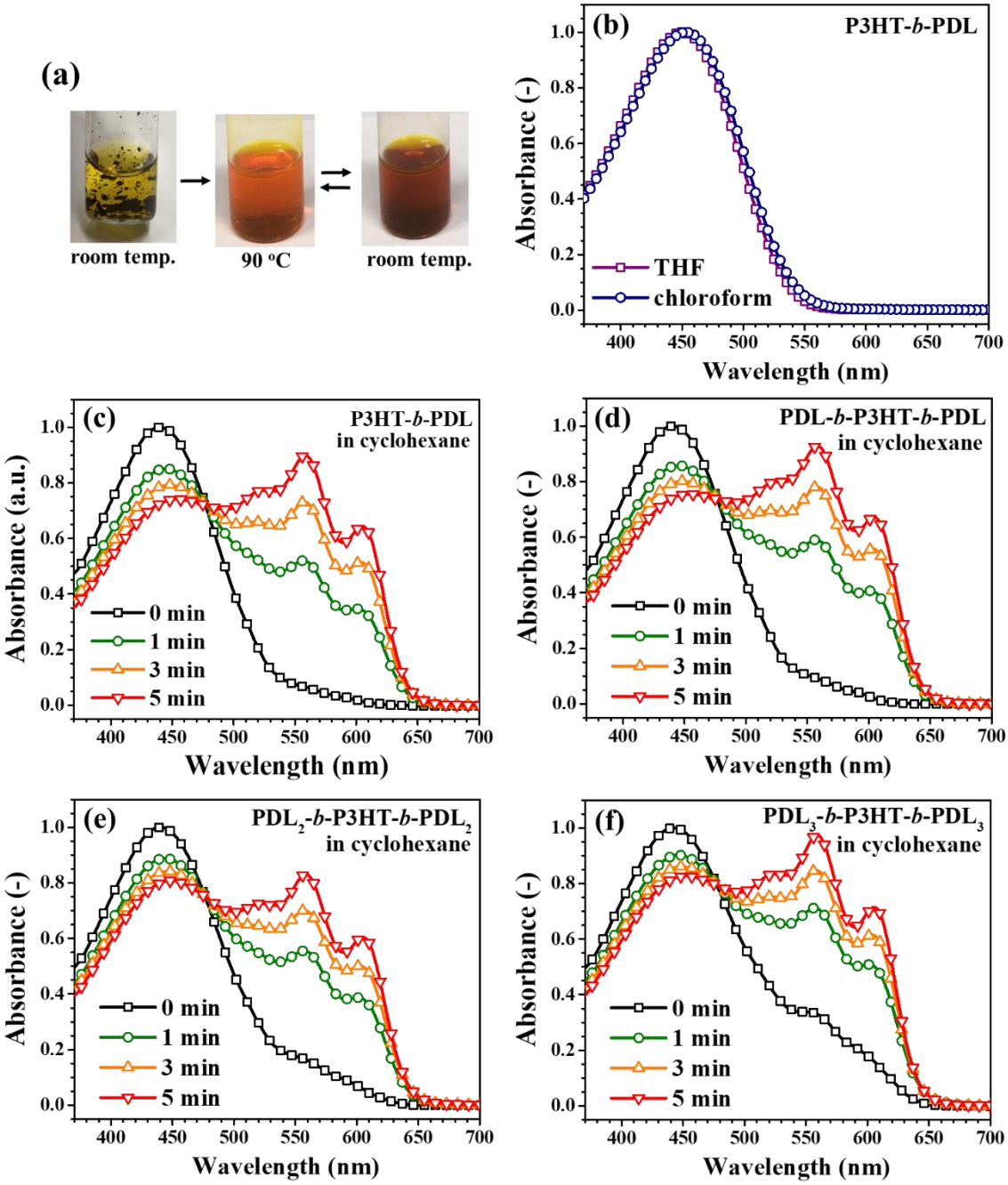

Fig. 2.9 (a) Photographs of P3HT-*b*-PDL solution in cyclohexane (3g L^{-1}) at different temperatures. (b) Solution UV-vis absorption spectra of P3HT-*b*-PDL in THF and chloroform, Solution UV-vis absorption spectra of (c) P3HT-*b*-PDL, (d) PDL-*b*-P3HT-*b*-PDL, (e) PDL_2-*b*-P3HT-*b*-PDL_2 and (f) PDL_3-*b*-P3HT-*b*-PDL_3 in cyclohexane, which the spectra were recorded from 0 to 5 min after quenching from 90 °C to room temperature.

To study the behavior of BCP in solution in more details, solution-state UV-vis absorption spectra were recorded using diluted polymer solution (0.025 g L^{-1}). The solution of P3HT-*b*-PDL in chloroform and THF (**Fig. 2.9b**) exhibits only one strong absorption band at 453 and 450 nm, respectively, suggesting that the P3HT segment is well dissolved in these solvents at room temperature. In contrast, in the time-dependent UV-vis absorption spectra of the preheated cyclohexane solution (**Fig. 2.9c**), after cooling down the solution at room temperature, absorption bands at 520, 559 and 606 nm increase gradually over time. It indicates the formation and growing of the P3HT aggregates in the cyclohexane solution, similar to the solvatochromic method for P3HT and P3HT-based BCPs.[38, 39] Since the uneven evaporation in two-solvent system in solvatochromic method may affect the film formation and create defects in polymer films, the solution process to control polymer aggregates using only one selective solvent, cyclohexane, could be more attracting for thin film preparation of BCPs. Solution UV-vis spectra of the other BCPs in cyclohexane also show a similar behavior, which are provided in **Fig. 2.9d-f**.

In the next step, solid-state UV-vis absorption of the BCP thin films processed by cyclohexane, THF and chloroform were studied, as shown in **Fig. 2.10**. For the preparation of BCP thin films from cyclohexane process, after cooling down the preheated polymer solution (3 g L^{-1}) at room temperature for 3 min, the solutions were spin-coated onto quartz substrate with 5000 rpm. Note that suitable aging time of BCP solution is critical in this experiment.

When the BCP solution in cyclohexane is aged for over 5 min, large aggregation of polymer will be formed as judged by the solution color turning black, deteriorating uniformity and smoothness of thin film derived from spin-coating. In THF and chloroform process, on the other hand, the polymer solution was directly spin-coated onto the substrate. Note that the relatively higher boiling point of cyclohexane (81 °C) to chloroform (61 °C) and THF (66 °C) would also facilitate molecular packing and crystallization of P3HT. As can be seen, the individual BCP thin films processed by cyclohexane and THF exhibit a higher 0-0 absorption at around 600 nm than the film processed by chloroform, indicating stronger interchain (π-π) interactions between polymer backbone. It is worth to mention that the polymer films of each polymer processed by different solvents have almost the same on-set absorption wavelength, revealing that the optical bandgap and energy levels of polymer may not be affected by processing methods. Also, except for PDL-*b*-P3HT-*b*-PDL (BAB), the 0-0 absorption of the polymer films prepared from cyclohexane is stronger than the film made by THF solution. These results highlight the importance of the processing methods on the molecular assembly of BCPs. The polymer thin films fabricated by the cyclohexane process were overlapped and were compared in **Fig. 2.11**. As can be seen, the maximum 0-1 absorption showed slight blue-shift from 559 nm to 553 nm and the 0-0 absorption (around 600 nm) is relatively weaker compared to the pristine P3HT (represented by the α,ω -P3HT made by the solution in chloroform), which is probably resulted from the altered assemblies within P3HT domain. The

$A_{0\text{-}0}/A_{0\text{-}1}$ ratio of the BCPs ranged from 0.69 to 0.74, suggesting weak H-aggregates in the P3HT crystalline region.[40] Note that polymer films made by PDL_2-*b*-P3HT-*b*-PDL_2 and PDL_3-*b*-P3HT-*b*-PDL_3 exhibit a relatively stronger 0-0 absorption comparing to PDL-*b*-P3HT-*b*-PDL, indicating stronger interchain (π-π) interactions between polymer backbone. It suggests that introducing the branch soft segment of BCP may not weaken the interchain (π-π) interactions of the hard segment. The UV-absorption measurements highlight the importance of polymer architecture as well as the processing methods on the molecular assembly of BCP.

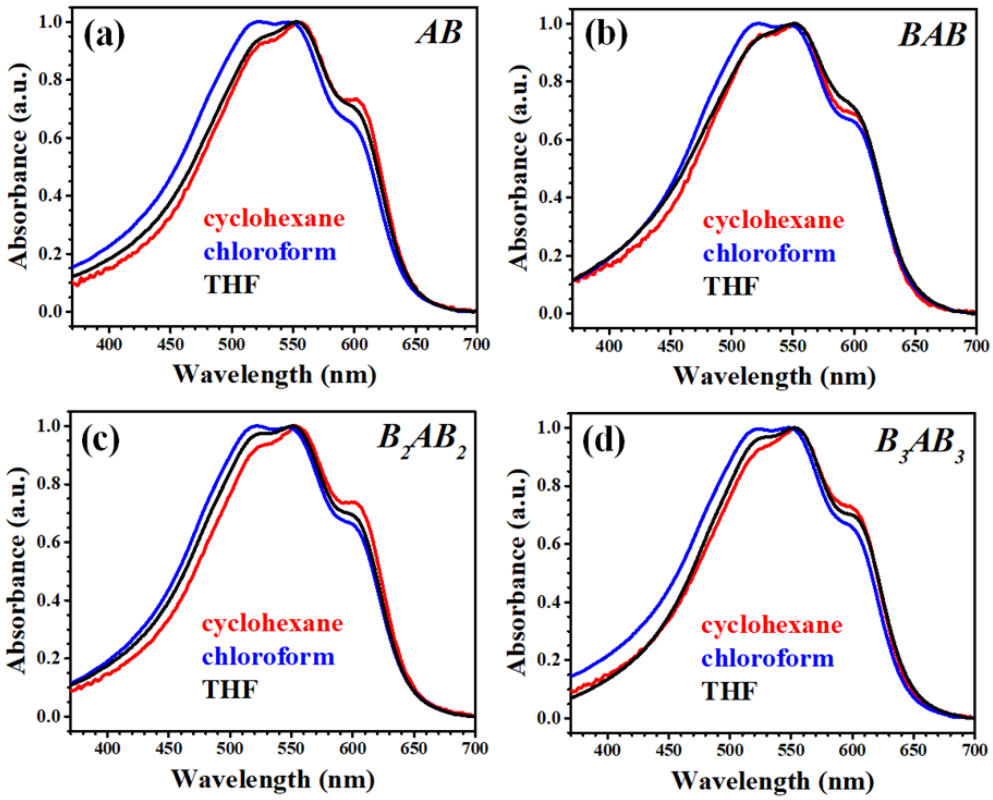

Fig. 2.10 Effect of the processing solvents on UV-absorption of the annealed polymer thin films.

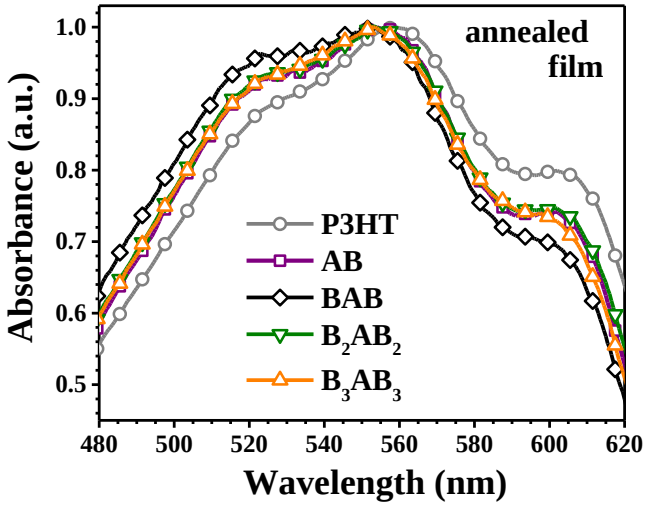

Fig. 2.11 Partial solid-state UV-vis absorption of the thermally annealed (140ºC, 20 min) polymer thin films spin-coated from P3HT (3g L^{-1} in chloroform) and the BCP (3g L^{-1} in cyclohexane) solutions.

Energy level calculations. In order to verify the energy levels of the studied polymers, UV-vis absorption spectra (**Fig. 2.10 and Fig. 2.11**) and CV profiles (**Fig. 2.12**) of the polymer films processed by THF were combined to determine the exact value. The optical bandgaps (E_g) extracted from the absorption onset for α,ω-P3HT, P3HT-*b*-PDL, PDL-*b*-P3HT-*b*-PDL, PDL_2-*b*-P3HT-*b*-PDL_2 and PDL_3-*b*-P3HT-*b*-PDL_3 range from 1.92 to 1.93 eV. Electrochemical properties were measured by CV and presented in **Fig. 2.12**. The highest occupied molecular orbital (HOMO) levels of the studied polymers were calculated by the onset oxidation potential, and the corresponding lowest unoccupied molecular orbital (LUMO) levels were then calculated by the equation of LUMO = HOMO + E_g. The HOMO/LUMO levels of α,ω-P3HT, PDL-*b*-P3HT, PDL-*b*-P3HT-*b*-PDL, PDL_2-*b*-P3HT-*b*-PDL_2 and PDL_3-*b*-P3HT-*b*-PDL_3 are -4.94/-3.02, -4.95/-3.02, -4.95/-3.02, -4.95/-3.02 and -4.95/-3.03, respectively. The E_g, HOMO and LUMO levels are summarized in **Table 2.1**. The energy levels of the studied polymers maintained in a similar level after introducing insulated PDL segments with different architectures. The result elucidates the optical and electrochemical properties of the studied polymers are mainly attributed to the P3HT conjugated backbone.[12]

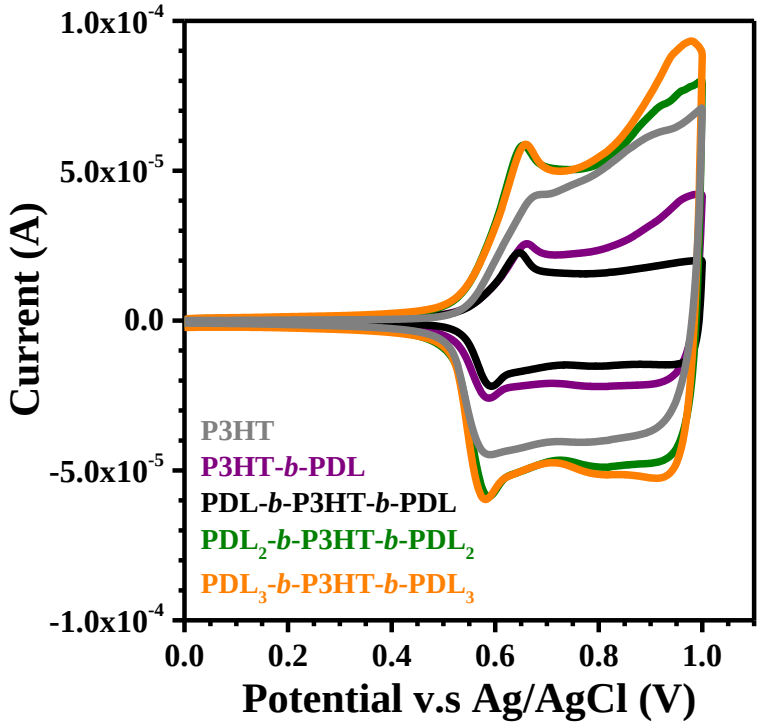

Fig. 2.12 CV measurements of the studied polymers.

2.3.4 Thin-film Morphology, Phase Separation and Crystallinity

AFM images. To investigate the morphologies of the polymer thin films, AFM and grazing-incidence X-ray scattering (GIXS) experiments were performed on the thin film samples prepared on octadecyltrichlorosilane (ODTS)–modified bare silicon wafer substrate. The silane-modified substrate with hydrophobic surface could facilitate the molecular assembly of conjugated polymer during spin-coating and annealing, and could help the polymer film being transferred to another soft substrate for stretching test.[25, 41] For the AFM and grazing incidence wide angle X-ray (GI-WAXS) measurements, the 40-50 nm-thick polymer films prepared with the same spin-coating parameters were examined. For the grazing incidence

small angle X-ray (GI-SAXS) measurement, film thickness was tuned up to 70-80 nm for the detection of microphase separation within the polymer films. The AFM images of the polymer thin films are shown in **Fig. 2.13**. As can be seen in the figure, the PDL-*b*-P3HT-*b*-PDL thin film processed by chloroform shows no phase separation in the phase image (**Fig. 2.13a**). Also, the height image **(Fig. 2.13g)** is very smooth with the root mean squared surface roughness (R_q) of 0.36 nm. The BAB thin film made by the solution in THF possesses a more obvious phase separation in the phase image (**Fig. 2.13b**), but with a much higher R_q calculated by the height image (R_q = 3.74 nm, **Fig. 2.13h**). Compared to the above results, the P3HT-*b*-PDL, PDL-*b*-P3HT-*b*-PDL, PDL_2-*b*-P3HT-*b*-PDL_2, and PDL_3-*b*-P3HT-*b*-PDL_3 thin films processed by cyclohexane (**Fig. 2.13c-f**) exhibit a distinct phase separating domain of P3HT with the nanofibrillar structure, along with a small R_q of 0.56 nm, 0.61 nm, 0.73 nm and 0.86 nm (from height image, **Fig. 2.13i-l**), respectively. Moreover, two-dimensional fast Fourier transformation (2D FFT) images of **Fig. 2.13c-f** exhibit ring-like patterns attributed to uniform in-plane phase separation within the BCP thin films. It suggests that the selective solvent approach on the BCP system is able to create polymer thin film with a smooth surface and to induce the formation of P3HT nanofibrils with a specific fiber width. Compared to the phase image of the diblock copolymer (**Fig. 2.13c**), the triblock copolymers (**Fig. 2.13d-f**) exhibit the P3HT nanofibrils with a smaller fiber width probably owing to the confined movement of the P3HT block in the middle of the polymer chain. Phase separation of the BCPs and the average

distance between P3HT nanofibers was investigated in more detail by GI-SAXS experiments, which would be discussed later.

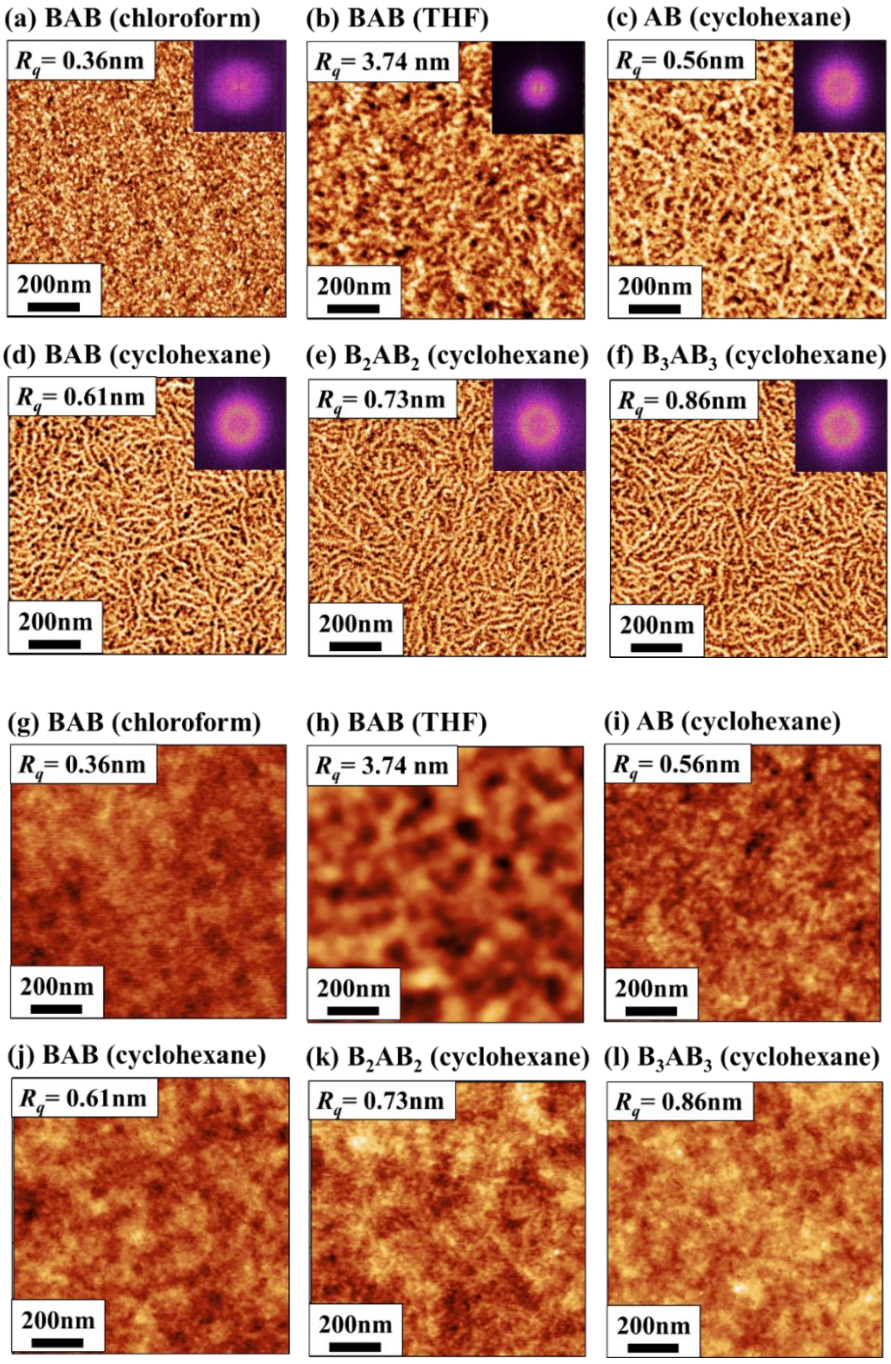

Fig. 2.13 AFM phase (a-f) and height (g-l) images of the annealed BAB films spin-coated from (a, g) chloroform and (b, h) THF solutions, and the (c, i) AB, (d, j) BAB, (e, k) B_2AB_2 and (f, l) B_3AB_3 films spin-coated from the solution in cyclohexane. The insets show 2D FFT images (upper right of a-f) and, R_q (upper left of g-l) and scale bars (lower left).

GIXS experiments. For the GIXS measurements of the BCPs, I mainly focused on the thin films processed by polymer solution in cyclohexane (**Fig. 2.14**), and the domain spacing was summarized in **Table 2.2** along with the thermal properties of the studied polymers. GI-WAXS measurements were performed to understand the orientation and molecular packing of the P3HT chains, and an open source software (GIXSAnalysis) was employed to convert the 2-D plots into pole figures.[42] Note that the GI-WAXS experiments were also conducted on the α,ω-P3HT and N_3-PDL film, representing the P3HT and PDL building blocks of the BCP (**Fig. 2.15a and b**). Also, the GI-WAXS 2D images of the BAB film from the chloroform and THF process were provided for comparison (**Fig. 2.15c and d**). As shown in **Fig. 2.14a-d**, the BCP thin films processed by cyclohexane have strong layer stacking patterns up to third order along the out-of-plane direction, denoted as (100), (200), and (300), and π-π stacking pattern along the in-plane direction, denoted as (010), representing the P3HT crystallites with edge-on orientation.[41] Similar patterns were observed in the BCP film from the THF process (**Fig. 2.15d**) but not from the chloroform process (**Fig. 2.15c**). The layer stacking distance (d_{layer}) and π-π stacking distance ($d_{\pi\text{-}\pi}$) of the studied BCPs calculated by 1-D cuts of the scattering profile **(Fig. 2.14e, f**) are summarized in **Table 2.2**. The d_{layer} and $d_{\pi\text{-}\pi}$ values of the BCPs are 16.74 - 16.89 Å and from 3.84 - 3.87 Å respectively, which are very close to the d-spacing of the pristine P3HT (d_{layer} = 16.69 Å, $d_{\pi\text{-}\pi}$ = 3.84 Å). These results indicate that P3HT crystallites with good quality could be formed in the prepared BCPs which is not affected by the introduction of the

branch PDL blocks, thus the conducting channel in P3HT domain for intermolecular (π-π) charge transfer could be maintained.

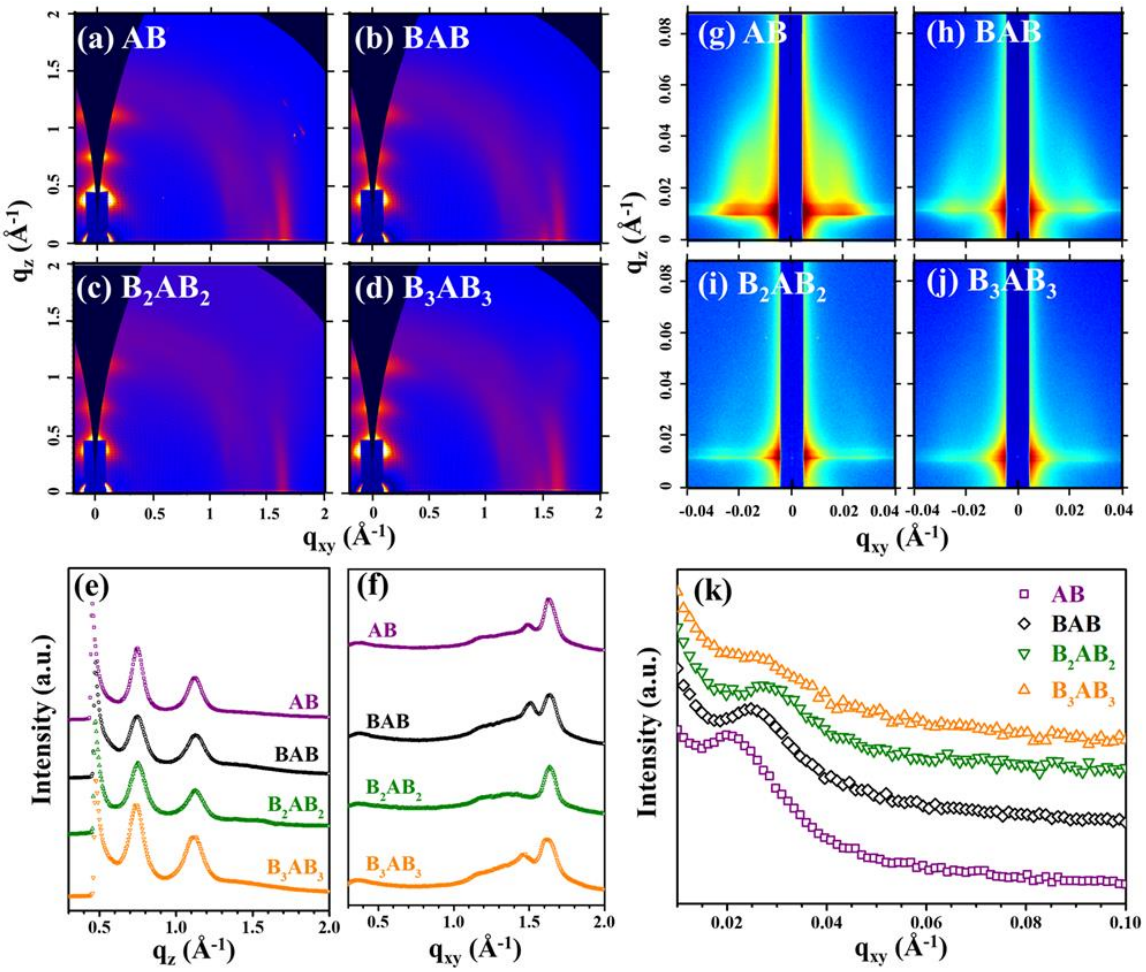

Fig. 2.14 GI-WAXS (a-d) and GI-SAXS (g-j) 2D patterns of the (a, g) AB, (b, h) BAB, (c, i) B_2AB_2 and (d, j) B_3AB_3 thin films prepared from the cyclohexane solutions. The 1D (e) out-of-plane and (f) in-plane cut profiles of the GI-WAXS 2D patterns, and (k) the 1D in-plane cut profiles of the GI-SAXS 2D patterns. The concentration of the solutions for spin-coating was 3g L^{-1} and all the thin film samples were annealed at 140 ºC for 20 min.

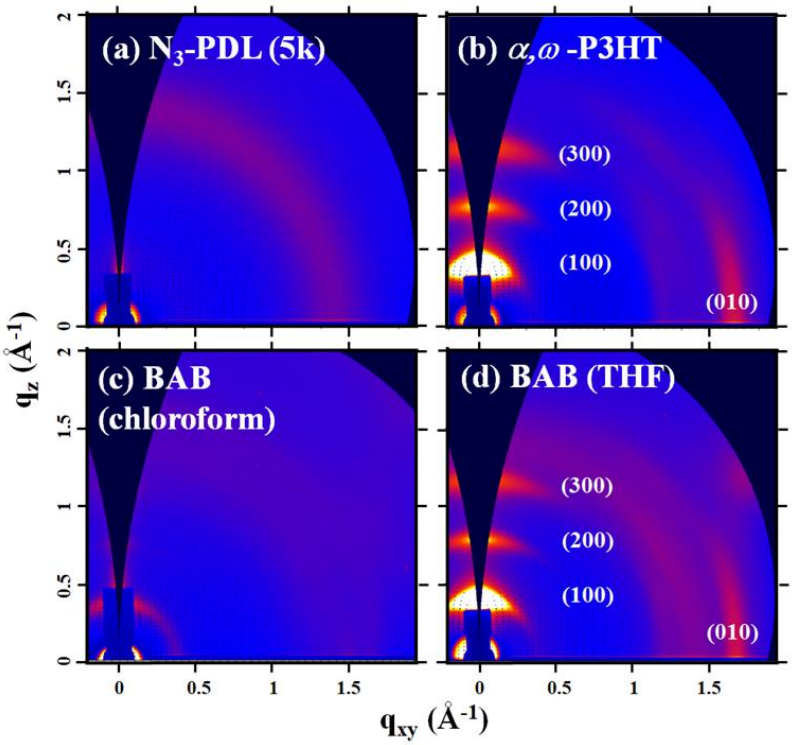

Fig. 2.15 GI-WAXS 2d patterns of the thin films spin-coated by (a) N_3-PDL (5k) solution in THF (10g L^{-1}), (b) α,ω-P3HT solution in THF (10g L^{-1}), (c) BAB solution in chloroform (3g L^{-1}), and (d) BAB solution in THF (3g L^{-1}). For **Fig. 2.15a**, the as-casted film was measured. For **Fig. 2.15b-d**, the samples were thermally annealed at 140 °C for 20 min before measurement.

Table 2.2 Melting temperature (T_m), domain spacings, OFET device performance, and stretchability of the studied polymers.

sample	T_m [a] (°C)	X_{P3HT} [a] (%)	d_{layer} [b] (Å)	$d_{\pi-\pi}$ [b] (Å)	d_{SAXS} [c] (Å)	crack onset [d] (%)
P3HT[e]	222.1, 231.7	28.4%	16.69	3.84	-	<20%
AB	216.5, 238.3	29.6%	16.82	3.85	305.0	25~50%
BAB	208.6, 227.7	33.6%	16.89	3.84	257.1	~50%
B_2AB_2	203.3, 220.0	32.5%	16.74	3.84	224.4	75~100%
B_3AB_3	203.8, 220.6	31.4%	16.77	3.87	225.8	~100%

[a] Determined from the 2nd heating curves of DSC traces (**Fig. 2.8b**). [b] Determined from GI-WAXS 1D cuts (**Fig. 2.14e and f**). [c] Determined from GI-SAXS 1D horizontal cuts (**Fig. 2.14k**). [d] Determined from the OM images of the stretched polymer thin films (**Fig. 2.19**). [e] α,ω-P3HT was used to represent P3HT for all the characterizations.

As mentioned before, GI-SAXS measurements provide the information of microphase separation in the range between tens to hundreds nanometers, which is suitable for the analysis of the prepared BCPs. 2-D GI-SAXS patterns of the BCP thin films are shown in **Fig. 2.14g-j**. As shown in the figures, the scattering signals of the PDL_2-*b*-P3HT-*b*-PDL_2 and PDL_3-*b*-P3HT-*b*-PDL_3 thin films along the in-plane direction are weaker than those of P3HT-*b*-PDL and PDL-*b*-P3HT-*b*-PDL, suggesting the more random phase separation of the branched polymers. This phenomenon can be explained by the interrupted assembly of P3HT near P3HT/PDL interfaces in branch polymers and more P3HT amorphous phase created within the P3HT domain. Horizontal 1-D cuts of the GI-SAXS profile were performed (**Fig. 2.14k**) to

verify the relationships between the domain-spacing and BCP architecture. Domain spacing sizes for the P3HT-*b*-PDL, PDL-*b*-P3HT-*b*-PDL, PDL_2-*b*-P3HT-*b*-PDL_2, and PDL_3-*b*-P3HT-*b*-PDL_3 thin films calculated by GI-SAXS 1-D cuts (d_{SAXS}) are 305.0 Å, 257.1 Å, 224.4 Å and 225.8 Å, respectively, which is also summarized in **Table 2.2**. The linear triblock copolymer (PDL-*b*-P3HT-*b*-PDL) shows a smaller d_{SAXS} than diblock copolymer (P3HT-*b*-PDL), which agrees well with our previous study about the relationship between block sequence and the phase separation of P3HT based BCPs.[14] Moreover, by introducing branched soft segments to the triblock copolymers (PDL_2-*b*-P3HT-*b*-PDL_2 and PDL_3-*b*-P3HT-*b*-PDL_3), the domain spacing size of the BCPs could be further decreased by more than 30 Å (13% of d_{SAXS} of PDL-*b*-P3HT-*b*-PDL).

Considering the DSC and GIXS experiments, I propose the phase separation behavior of the prepared linear and branched triblock copolymers. As illustrated in **Fig. 2.16**, due to confined assembly of P3HT in soft-hard-soft type triblock BCP, P3HT crystallites with the same quality can be achieved in PDL-*b*-P3HT-*b*-PDL, PDL_2-*b*-P3HT-*b*-PDL_2, and PDL_3-*b*-P3HT-*b*-PDL_3, but the size of P3HT crystallites decreases slightly after introducing the branch soft segments, due to the interrupted assembly of P3HT near the P3HT/PDL interfaces. The author also suggests that the smaller domain spacing (d_{SAXS}) of the branched BCPs is mainly attributed to the shrink of PDL domain between two P3HT fibers. Introduction of branched PDL segments leads to a spatially crowded P3HT/PDL interface and creates higher interfacial

curvature between P3HT and PDL, thus the amorphous PDL chains tend to distribute "nonplanarly" between the neighboring P3HT fibers. Moreover, because of almost the same PDL weight ratio in each BCP, each PDL chain in the branched BCP is shorter than the PDL chain in linear BCP. Therefore, it can be expected that the average length of PDL domain between two P3HT fibers in branched BCPs is shorter than the length of PDL domain in linear BCPs. The proposed triblock architecture design with branched soft segments could tailor crystallization behavior of P3HT and phase separation of BCP without affecting interchain (π-π) interaction within the P3HT crystalline domain, which is potential in developing semiconducting material with high carrier mobility and advanced mechanical property.

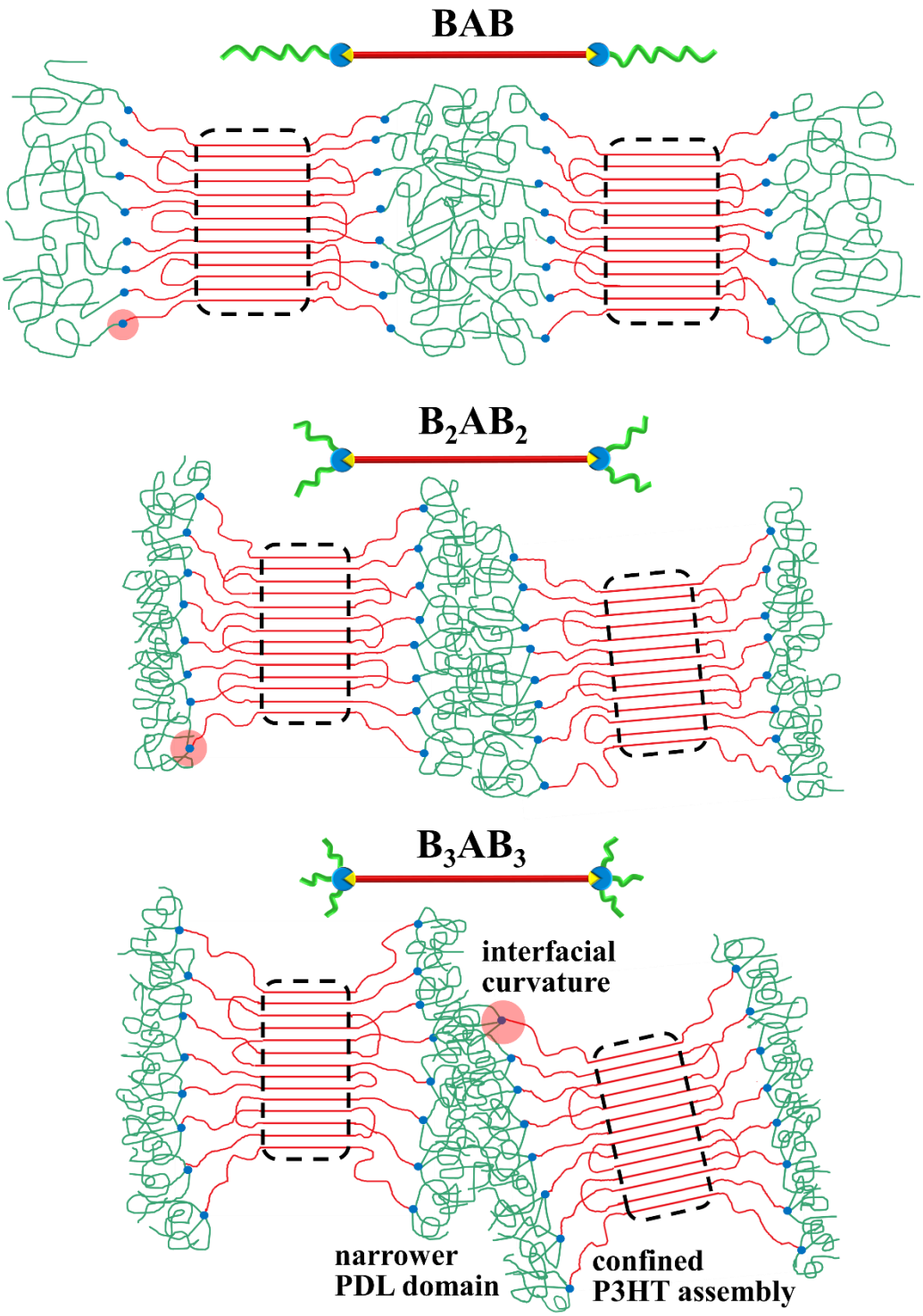

Fig. 2.16 Schematic diagram of the proposed phase-separated structures in PDL-*b*-P3HT-*b*-PDL (BAB), PDL_2-*b*-P3HT-*b*-PDL_2 (B_2AB_2), and PDL_3-*b*-P3HT-*b*-PDL_3 (B_3AB_3). The red and green parts represent the P3HT and PDL chains, respectively. The area enclosed in the black squares represents the P3HT crystalline region.

2.3.5 Charge mobility and Mechanical Properties

Charge mobility. Bottom-gate-top-contact OFETs with Si/SiO_2/polymer/Au configuration, illustrated in **Fig. 2.17a**, were fabricated using the synthesized BCPs as a semiconducting layer to evaluate the transistor characteristics. The polymer solution in cyclohexane, chloroform, and THF were used to prepare the polymer thin films on top of the ODTS-modified 300 nm wafer. Note that the synthesized α,ω-P3HT was used to fabricate the pristine P3HT devices, which could be used as a reference sample to prove the impact of the soft segment. Current-Voltage (I_{ds}-V_g) characteristics of the transistor devices fabricated by polymer solutions using different solvents are summarized in **Fig. 2.17b-d**. As can be seen, the OFETs fabricated by the BCP solutions in cyclohexane **Fig. 2.17b**) show remarkably higher on-current than the BCP devices processed by the other solvents (**Fig. 2.17c and d**). The superior performance of the devices processed by cyclohexane is due to the smooth polymer films with the well-developed P3HT nanofibrillar structure, supported by the thin film morphology analysis. **Fig. 2.17e and f** summarize the charge mobility and on/off current ratio calculated from the I_{ds}-V_g characteristics. As can be seen, the mobilities (**Fig. 2.17e**) of the P3HT-*b*-PDL, PDL-*b*-P3HT-*b*-PDL, PDL_2-*b*-P3HT-*b*-PDL_2, and PDL_3-*b*-P3HT-*b*-PDL_3 devices processed by cyclohexane are 0.088 $cm^2\ V^{-1}\ S^{-1}$, 0.085 $cm^2\ V^{-1}\ S^{-1}$, 0.089 $cm^2\ V^{-1}\ S^{-1}$, and 0.045 $cm^2\ V^{-1}\ S^{-1}$, respectively, which are more than ten times higher than the mobilities of the devices processed by the other solvents, and are comparable with the pristine P3HT device

(0.116 cm^2 V^{-1} S^{-1}). The cyclohexane process can also provide high on/off current ratios (over 6.5×10^4) to all the BCP devices. Within the BCP devices processed from the cyclohexane solution, except for PDL_3-*b*-P3HT-*b*-PDL_3, the charge mobility of the OFETs seems to be not related to the polymer architecture. I expect that the mobility of the devices was optimized to the maximum value in this P3HT based BCP system. Therefore, the mobility of B_2AB_2 could reach the same level as AB and BAB device even with a lower crystallinity and a smaller crystallite size. In the case of B_3AB_3, the mobility of OFET cannot reach the same level as the other BCP devices. I speculate that the slightly lower mobility of the B_3AB_3 device may result from the defects formed in the polymer thin film and the lower crystallinity of the polymer. **Table 2.3** summarizes the charge mobility, on/off current ratio, and turn-on voltage of the OFETs made by the studied polymers using the cyclohexane, chloroform and THF process. Also, the output characteristics of the OFETs made by P3HT in chloroform and the BCPs in cyclohexane are provided in **Fig. 2.18**. These results suggest that the semiconducting properties of the prepared BCPs could reach the same level as the pristine P3HT homopolymer by controlling the phase separation of the BCPs.

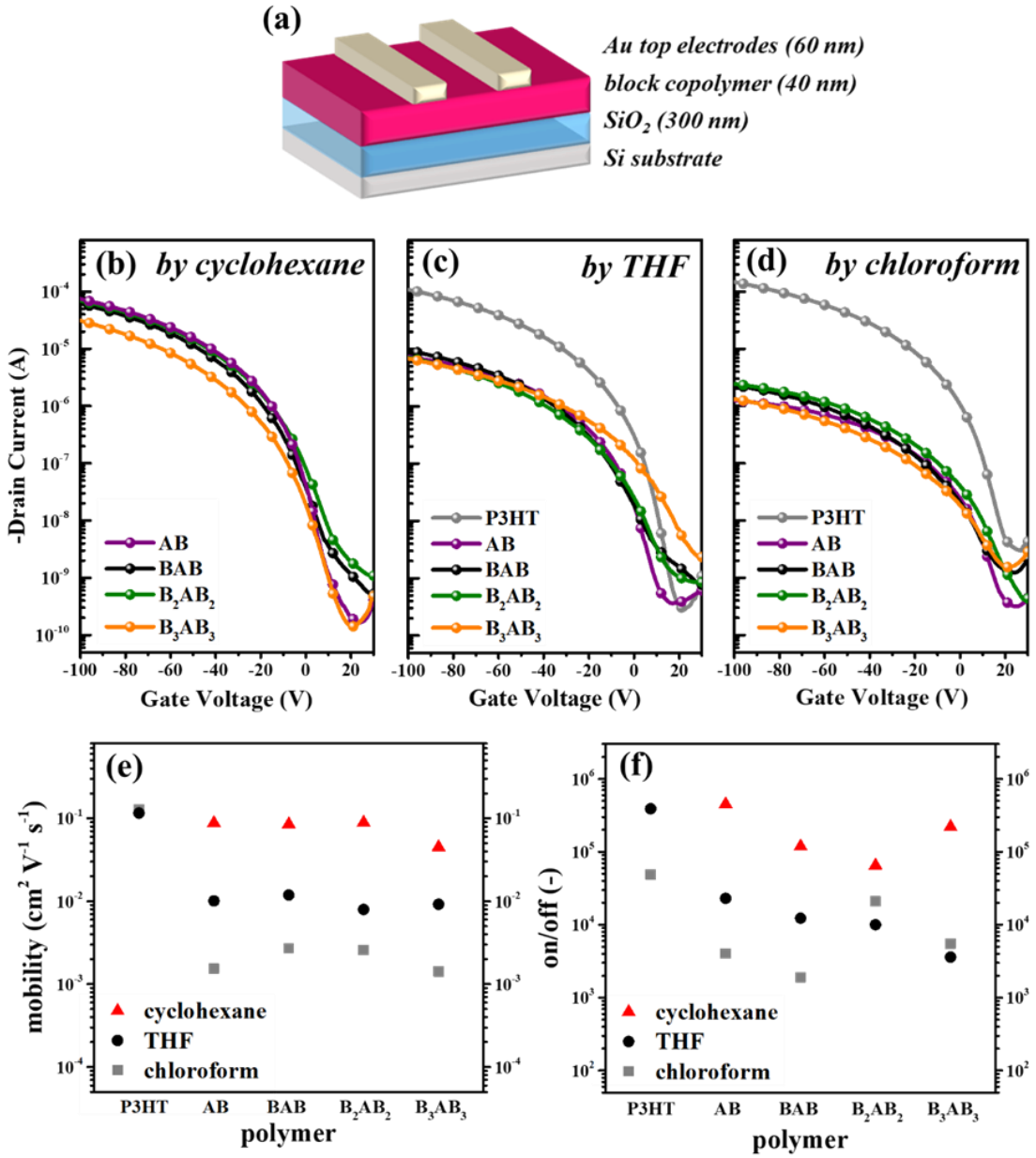

Fig. 2.17 (a) Device structure of the OFETs in this study. $I_{ds} - V_g$ characteristics of the OFET devices made by the studied polymers using (b) cyclohexane, (c) THF and (d) chloroform as processing solvent. Comparison of (e) charge mobility and (f) on/off current ratio of the OFETs. All of the device performance were calculated by at least 10 devices with three different batches.

Table 2.3 Device performances of the OFETs processed from cyclohexane, THF and chloroform solutions.

solvent	sample	μ ($cm^2 V^{-1} s^{-1}$)	on/off (-)	V_{on} (V)
cyclohexane	AB	8.8×10^{-2}	4.5×10^{5}	-2.6
	BAB	8.5×10^{-2}	1.2×10^{5}	-3.9
	B_2AB_2	8.9×10^{-2}	6.5×10^{4}	-2.1
	B_3AB_3	4.5×10^{-2}	2.2×10^{5}	-3.5
THF	P3HT	1.2×10^{-1}	3.9×10^{5}	1.5
	AB	1.0×10^{-2}	2.3×10^{4}	0.8
	BAB	1.2×10^{-2}	1.2×10^{4}	-1.4
	B_2AB_2	8.0×10^{-3}	1.0×10^{4}	1.9
	B_3AB_3	9.2×10^{-3}	3.6×10^{3}	12.2
chloroform	P3HT	1.3×10^{-1}	4.9×10^{4}	6.0
	AB	1.5×10^{-3}	4.0×10^{3}	10.8
	BAB	2.7×10^{-3}	1.9×10^{3}	6.0
	B_2AB_2	2.6×10^{-3}	2.1×10^{4}	10.4
	B_3AB_3	1.4×10^{-3}	5.5×10^{3}	10.1

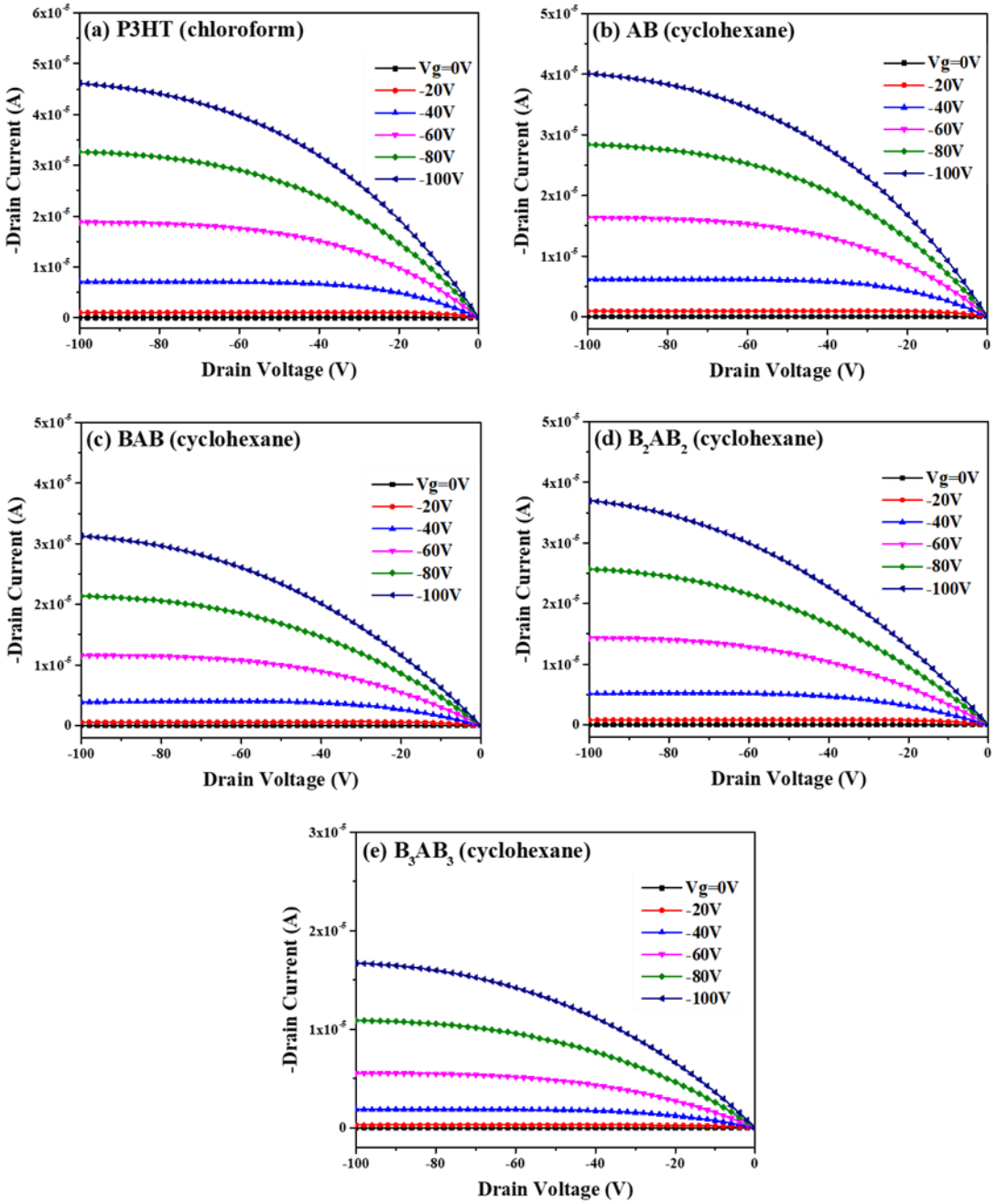

Fig. 2.18 Output characteristics of the OFETs made by (a) P3HT, (b) P3HT-*b*-PDL (AB), (c) PDL-*b*-P3HT-*b*-PDL (BAB), (d) PDL_2-*b*-P3HT-*b*-PDL_2 (B_2AB_2) and (e) PDL_3-*b*-P3HT-*b*-PDL_3 (B_3AB_3). 3g L^{-1} polymer solution in chloroform was used for **Fig. 2.18a**, and 3g L^{-1} polymer solution in cyclohexane was used for **Fig. 2.18b-e**.

Mechanical Properties. The mechanical properties of the polymers were investigated by optical microscopy (OM), polarized UV absorption and amplitude modulation-frequency modulation atomic force microscopy (AM-FM) viscoelastic mapping techniques. To study the stretchability of the polymer thin films, the crack onset points[14] are determined by OM images of the stretched polymer films and those values are summarized in **Table 2.2**. **Fig. 2.19** shows the OM images of the stretched films on the top of a PDMS substrate. Different from the pristine P3HT film (represented by α,ω-P3HT) which could only endure limited strain and show significant cracks at 20% strain, the BCP thin films exhibit a higher stretchability owing to the incorporated PDL soft segments. For example, some small cracks are found in the P3HT-*b*-PDL film at 25% strain and those cracks become larger up to the 50% strain. The PDL-*b*-P3HT-*b*-PDL film exhibits a relatively higher stretchability than P3HT-*b*-PDL since nearly no crack is found at 25% strain. However, continuous cracks are found at over 50% strain. Moreover, the triblock copolymers with the branched soft segments (PDL_2-*b*-P3HT-*b*-PDL_2 and PDL_3-*b*-P3HT-*b*-PDL_3) show significantly improved stretchability than the linear diblock and triblock copolymers (P3HT-*b*-PDL and PDL-*b*-P3HT-*b*-PDL). For example, in the OM images of PDL_2-*b*-P3HT-*b*-PDL_2, no crack is found until the 75% strain, and then continuous cracks on the polymer films are found at 100% strain. In the OM images of PDL_3-*b*-P3HT-*b*-PDL_3, localized small cracks with a low density are found at 75% strain and the cracks become slightly longer at the 100% strain. On top of that, the density of the cracks at 100% strain is

less than those in the PDL_2-*b*-P3HT-*b*-PDL_2 film, indicating that the polymer thin films made by PDL_3-*b*-P3HT-*b*-PDL_3 is the most stretchable among all the studied BCPs. Thus, the order of the stretchability of the BCPs depending on polymer architecture can be summarized as: AB < BAB < B_2AB_2 < B_3AB_3. Note that some defects (black dots in OM images) can be found in the B_3AB_3 film, which are probably the big P3HT aggregates formed during the spin-coating process. It may result in the slightly lower device performance of the B_3AB_3 device (**Fig. 2.18b and e**). To understand if the cracks were formed in P3HT hard domains or PDL soft domains, it would be interesting to investigate the detailed phase images of the stretched polymer films by atomic force microscopy in future studies.

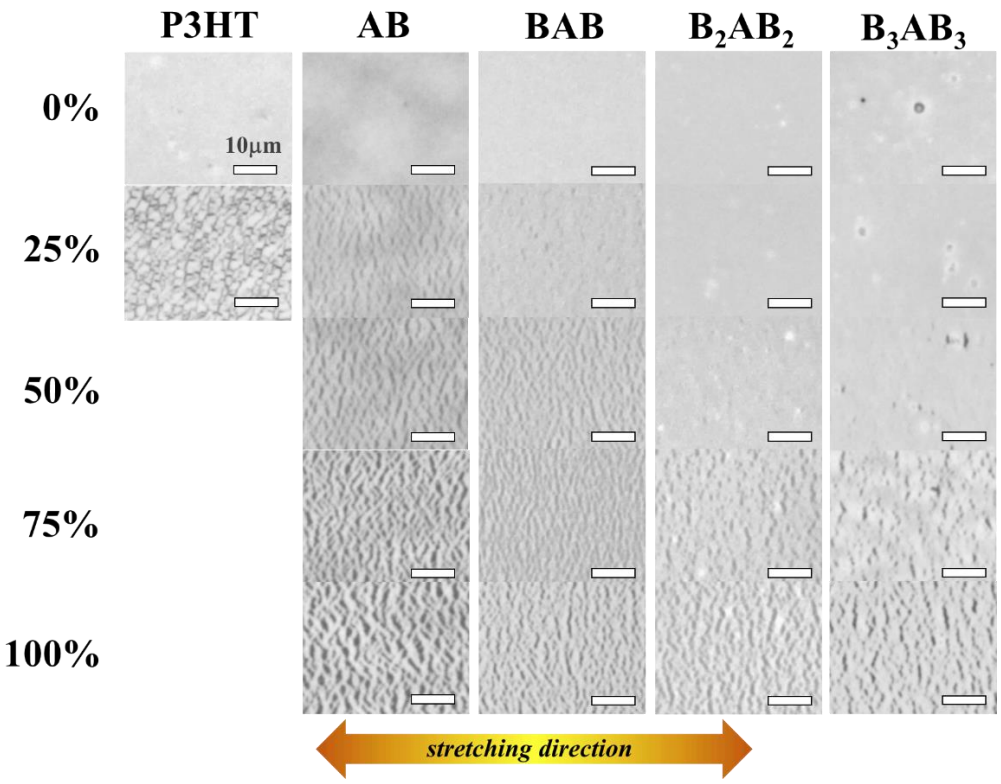

Fig. 2.19 OM images of the stretched polymer films on PDMS substrate. P3HT film was prepared from a solution in THF, and BCP films were prepared from solutions in cyclohexane.

Moreover, **Fig. 2.20** summarizes the elastic modulus of the polymer films through AM-FM viscoelastic mapping experiments. AM-FM is an AFM technique which can map topology and nanomechanical properties of sample simultaneously. Utilizing this technique, the Young's modulus of the studied polymers can be calculated and compared at thin-film state. As shown in **Fig. 2.20a-d**, the elastic modulus mapping images with the same scale bar suggest the order of modulus of the polymers: P3HT > PDL-*b*-P3HT-*b*-PDL > PDL_2-*b*-P3HT-*b*-PDL_2 > PDL_3-*b*-P3HT-*b*-PDL_3. Based on **Fig. 2.20a-d**, elastic modulus of the α,ω-P3HT, PDL-*b*-P3HT-*b*-PDL, PDL_2-*b*-P3HT-*b*-PDL_2, and PDL_3-*b*-P3HT-*b*-PDL_3 films are compared by counts in **Fig. 2.20e**. The peak center of elastic modulus by counts for the α,ω-P3HT, PDL-*b*-P3HT-*b*-PDL, PDL_2-*b*-P3HT-*b*-PDL_2, and PDL_3-*b*-P3HT-*b*-PDL_3 films is 1.64, 1.46, 1.30 and 1.08 GPa, respectively, which is consistent with the findings on the improvement of stretchability through the branch BCP design, as investigated by OM. As illustrated in **Fig. 2.16**, the introduction of the branched PDL segments to the triblock copolymers may affect the assembly of P3HT, leading to more random phase separation of the BCPs and smaller size of P3HT crystallites, thus enhancing the stretchability of the branched triblock copolymers.

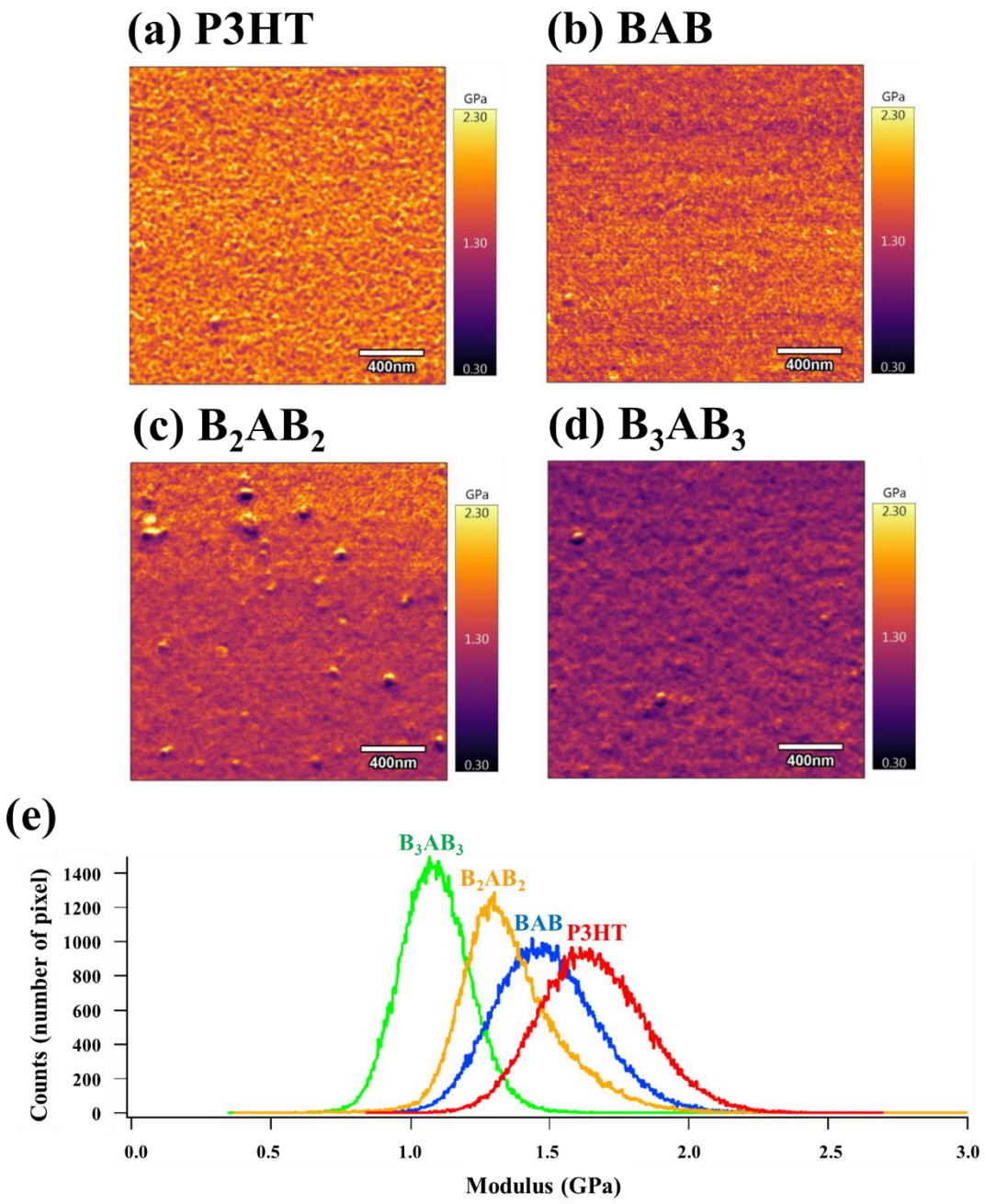

Fig. 2.20 Elastic modulus mapping of (a) α,ω-P3HT (P3HT), (b) PDL-*b*-P3HT-*b*-PDL (BAB), (c) PDL_2-*b*-P3HT-*b*-PDL_2 (B_2AB_2), and (d) PDL_3-*b*-P3HT-*b*-PDL_3 (B_3AB_3) determined by AM-FM viscoelastic mapping with the same scale bar from 0.30 to 2.30 GPa. (e) The comparison of the modulus of the studied polymers by counts using **Fig. 2.20 a-d**.

Aside from the micrometer-scale cracks formed in polymer thin films which were observed by OM (**Fig. 2.19**), the orientation of conjugated polymer on substrate may also affect

the performance of thin-film electronic devices.[41] Here I report the investigation of the chain alignment and crystallite orientation of P3HT within the stretched polymer thin films by polarized-UV (**Fig. 2.21**). The polymer film samples were first deposited on ODTS-wafer and transferred to PDMS substrate, and then were stretched to different strain levels for polarized UV measurements. Fig. **2.21a-j** show the normalized absorbance spectra of each polymer recorded with the polarized light perpendicular (**Fig. 2.21a, c, e, g**) and parallel (**Fig. 2.21b, d, f, h**) to the strain direction. Moreover, to compare the ability of chain alignment under stretching, the dichroic ratio at different strain level, $A_{\parallel}/A_{\perp}$, is summarized in **Fig. 2.21k,** where A is the absorbance of the film with polarized light parallel (||) and perpendicular ($\perp$) to the strain direction at the peak absorption wavelength. Unlike the absorption spectra of α,ω-P3HT (**Fig. 2.21a and b**), which show slightly enhancement of 0-0 absorption (around 600nm) according to strain, nearly no difference in the 0-0 absorption can be found in the spectra of the BCP films (**Fig. 2.21c-j**) in both directions under up to 100% strain, revealing no change of interchain (π-π) interactions and local conformational order according to the strain. As shown in **Fig. 2.21k**, the dichroic ratio of α,ω-P3HT increases to 1.06 at 25% strain, and then drops to around 1.02-1.03 at higher strain level, which is due to the poor stretchability of the pristine P3HT. On the other hand, the dichroic ratios of the BCPs gradually increase from 1.0 to 1.3-1.4 after applying 100% of strain, suggesting that the incorporated soft PDL segments may facilitate the chain-alignment of P3HT. However, the ability of chain alignment upon strain is

still weaker than the reported high-molecular-weight P3HT (molecular weight: 62000) with dichroic ratio of 3 at 90% strain.[41] Based on the above results, it can be inferred that the studied BCP thin films possess weak morphological anisotropy according to strain, which is probably due to the slightly tilted P3HT crystallites in the BCP films under stretching.

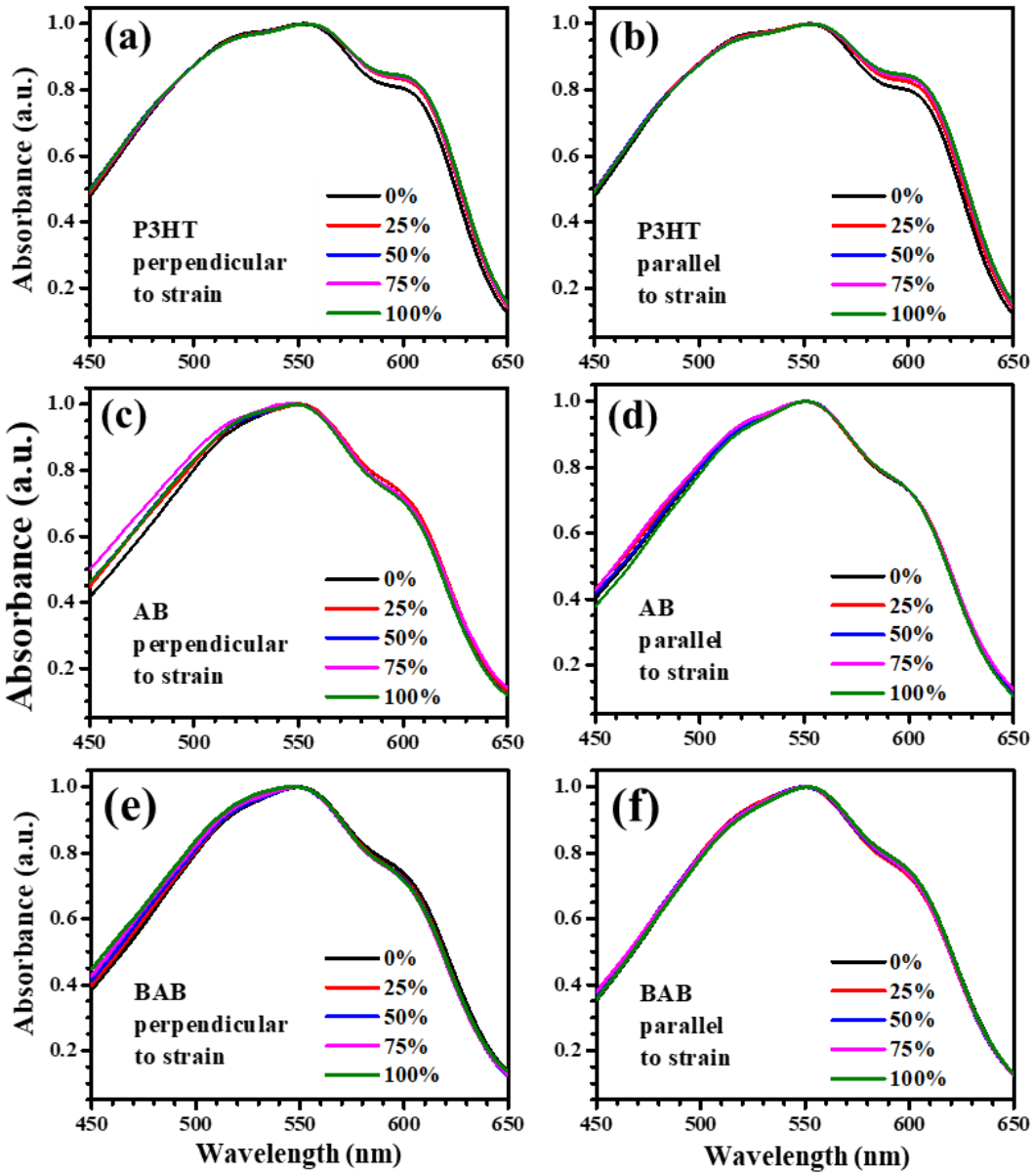
(a)
P3HT
perpendicular
to strain
(b)
P3HT
parallel
to strain
(c)
AB
perpendicular
to strain
(d)
AB
parallel
to strain
(e)
BAB
perpendicular
to strain
(f)
BAB
parallel
to strain
0%
25%
50%
75%
100%
Absorbance (a.u.)
Wavelength (nm)

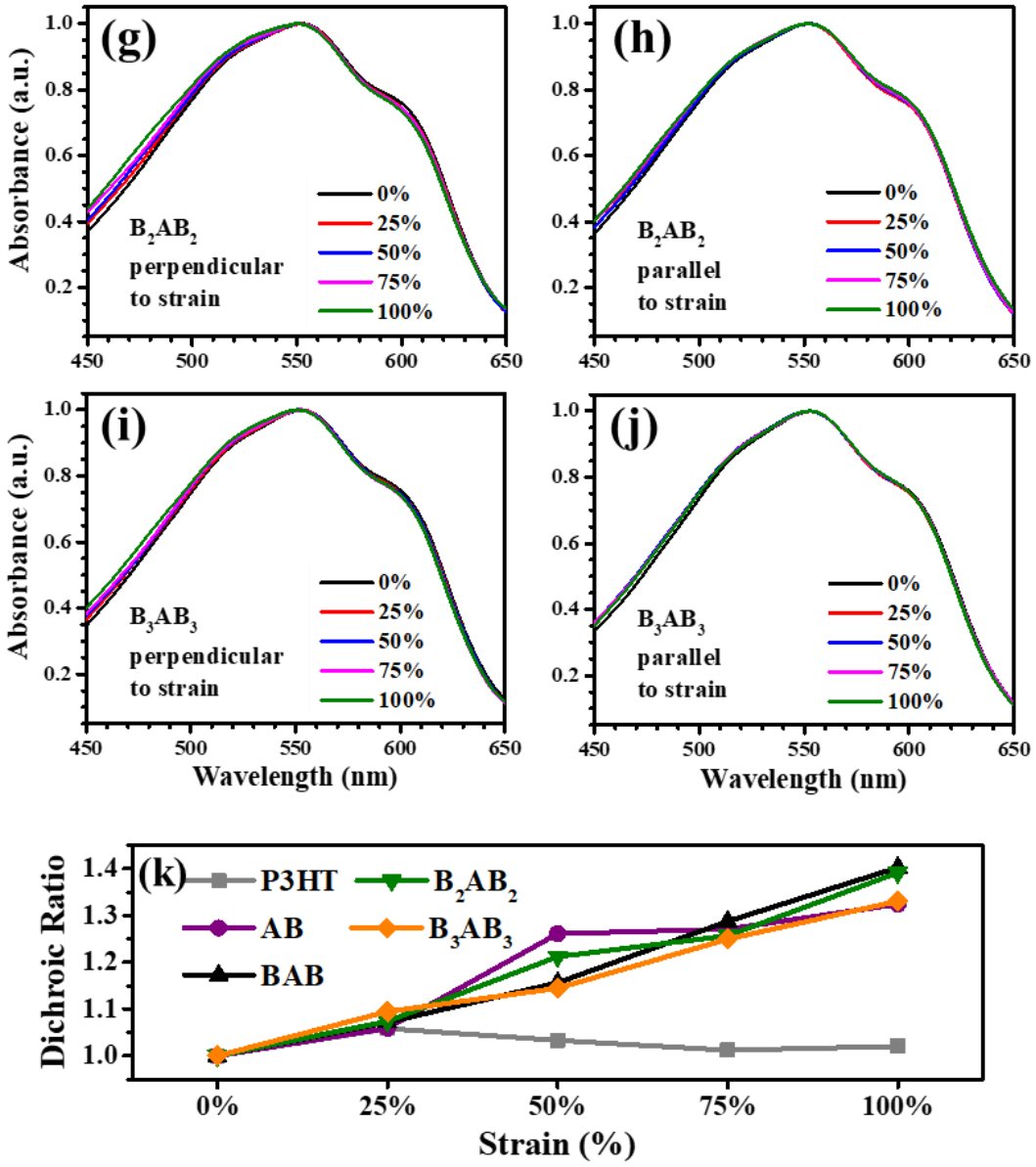

Fig. 2.21 Normalized UV absorption spectra of (a, b) *α,ω*-P3HT (P3HT), (c, d) P3HT-*b*-PDL, (e, f) PDL-*b*-P3HT-*b*-PDL, (g, h) PDL_2-*b*-P3HT-*b*-PDL_2 and (i, j) PDL_3-*b*-P3HT-*b*-PDL_3 with the polarized light (a, c, e, g, i) perpendicular and (b, d, f, h, j) parallel to the strain direction. (k) Dichroic ratio of the studied polymers with the strain from 0% to 100%.

2.3.6 Stretchable OFET Applications

The semiconducting properties of the stretched polymer thin films were studied by bottom-gate-top-contact OFETs with Si/SiO_2 (300nm)/stretched polymer/Au (60 nm) structure with the polymer films stretched at 0%, 25%, 50%, 75% and 100%. The pristine P3HT device was fabricated by the α,ω-P3HT solution in chloroform, and the BCP devices were made by the solution in cyclohexane. Note that the device performance in this section is weaker than the OFETs with the semiconducting layer directly deposit on top of the ODTS-modified wafer. It is due to the defect formed between SiO_2 layer and semiconducting layer after film transferring. The I_{ds}-V_g characteristics were measured with the charge transport channel parallel (∥) and perpendicular (⊥) to the strain direction, as shown in **Fig. 2.22a-i**. The device performance is summarized in **Table 2.4**, and the output curves of the devices at 75% strain with the channel parallel to strain are also provided in **Fig. 2.23**. For the further discussion, charge mobility (μ) and mobility retentions (μ/μ_0) of the prepared OFETs are plotted in **Fig. 2.22j and k**. Mobility anisotropy according to different strain level was calculated by the ratio between charge mobility measured with charge transporting channel parallel and perpendicular to strain direction, which is shown in **Fig. 2.24**. As can be seen in the figure, all of the OFETs in this research show small difference in charge mobility in parallel and perpendicular direction with mobility anisotropy below 1.2 at the strain level up to 100% strain, which is quite different from the report on strain-aligned P3HT (molecular weight: 62000) showing 5-time mobility

anisotropy of the OFET for 75% strain.[41] Therefore, I suggest that the performance of the stretchable devices do not change significantly with the direction due to the weak structural anisotropy, as explained in the polarized-UV experiments and dichroic ratio (**Fig. 2.21**), and the device performance is mainly deteriorated by the micrometer-scale cracks formed in the films, which can be observed in optical microscopes (**Fig. 2.19**).

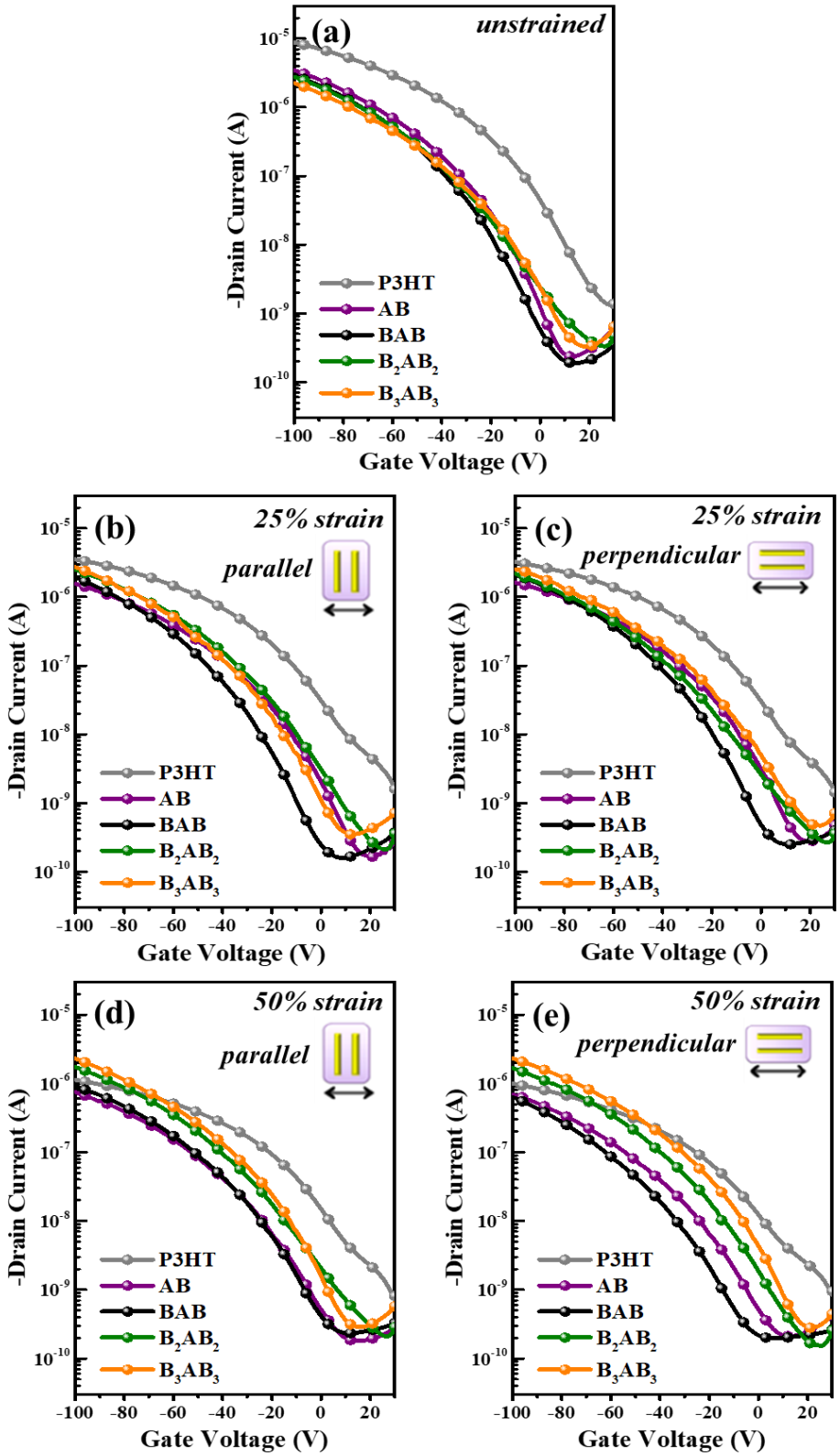
(a)
unstrained
(b)
25% strain
parallel
(c)
25% strain
perpendicular
(d)
50% strain
parallel
(e)
50% strain
perpendicular
-Drain Current (A)
Gate Voltage (V)
P3HT
AB
BAB
B2AB2
B3AB3

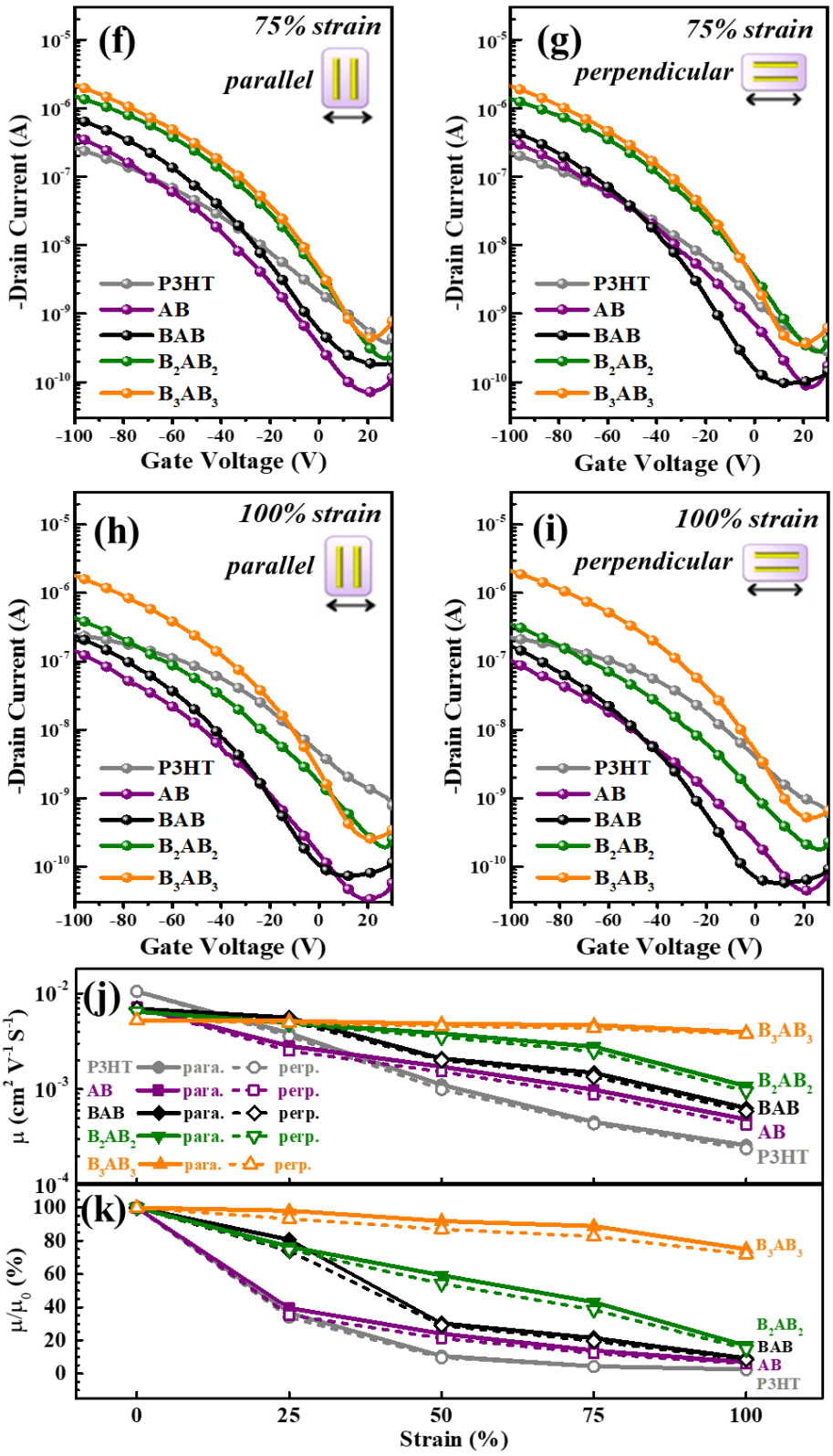

Fig. 2.22 (a) $I_{ds} - V_g$ curves of OFETs made by the (a) unstrained, (b, c) 25%, (d, e) 50%, (f, g) 75%, and (h, i) 100% stretched polymer films with charge transport channel (b, d, f, h) parallel and (c, e, g, i) perpendicular to the stretching direction. (j) Charge mobility (μ) and (k) mobility retentions (μ/μ_0) of the polymers with different stretch loadings.

Table 2.4 OFET performance of the devices made by the stretched and transferred polymer films (strain: 0%-100%).

	P3HT			AB		
strain	**μ ($cm^2 V^{-1} s^{-1}$)**	**on/off (-)**	**V_{on} (V)**	**μ ($cm^2 V^{-1} s^{-1}$)**	**on/off (-)**	**V_{on} (V)**
0%	1.05×10^{-2}	6.6×10^{3}	-7.0	7.14×10^{-3}	1.5×10^{4}	-29.1
25%∥	3.84×10^{-3}	2.2×10^{3}	2.9	2.82×10^{-3}	9.4×10^{3}	-21.5
25%⊥	3.57×10^{-3}	2.2×10^{3}	4.8	2.52×10^{-3}	5.9×10^{3}	-15.2
50%∥	1.11×10^{-3}	1.4×10^{3}	9.3	1.72×10^{-3}	4.2×10^{3}	-29.5
50%⊥	9.93×10^{-4}	1.0×10^{3}	7.3	1.52×10^{-3}	3.3×10^{3}	-30.6
75%∥	4.55×10^{-4}	7.1×10^{2}	-23.2	9.90×10^{-4}	5.6×10^{3}	-36.6
75%⊥	4.34×10^{-4}	8.3×10^{2}	-27.8	8.72×10^{-4}	3.9×10^{3}	-37.7
100%∥	2.59×10^{-4}	3.2×10^{2}	7.7	4.84×10^{-4}	4.3×10^{3}	-40.7
100%⊥	2.38×10^{-4}	3.7×10^{2}	7.6	4.23×10^{-4}	2.3×10^{3}	-38.7

	B_2AB_2			B_2AB_2		
strain	**μ ($cm^2 V^{-1} s^{-1}$)**	**on/off (-)**	**V_{on} (V)**	**μ ($cm^2 V^{-1} s^{-1}$)**	**on/off (-)**	**V_{on} (V)**
0%	6.92×10^{-3}	1.6×10^{4}	-34.2	6.45×10^{-3}	8.4×10^{3}	-32.4
25%∥	5.59×10^{-3}	1.2×10^{4}	-39.0	4.94×10^{-3}	1.2×10^{4}	-28.1
25%⊥	5.12×10^{-3}	8.5×10^{3}	-35.0	4.82×10^{-3}	8.3×10^{3}	-32.0
50%∥	2.09×10^{-3}	3.9×10^{3}	-31.8	3.82×10^{-3}	8.3×10^{3}	-31.7
50%⊥	2.01×10^{-3}	3.2×10^{3}	-35.2	3.50×10^{-3}	1.1×10^{4}	-26.9
75%∥	1.48×10^{-3}	3.9×10^{3}	-35.2	2.78×10^{-3}	6.7×10^{3}	-20.5
75%⊥	1.35×10^{-3}	5.0×10^{3}	-37.1	2.48×10^{-3}	4.9×10^{3}	-19.2
100%∥	6.36×10^{-4}	3.2×10^{3}	-38.6	1.08×10^{-3}	2.3×10^{3}	-34.4
100%⊥	5.85×10^{-4}	2.9×10^{3}	-41.3	9.53×10^{-4}	2.0×10^{3}	-38.9

	B_3AB_3		
strain	**μ ($cm^2 V^{-1} s^{-1}$)**	**on/off (-)**	**V_{on} (V)**
0%	5.25×10^{-3}	6.8×10^{3}	-30.3
25%∥	5.16×10^{-3}	8.3×10^{3}	-29.6
25%⊥	4.90×10^{-3}	5.4×10^{3}	-31.2
50%∥	4.83×10^{-3}	8.1×10^{3}	-34.7
50%⊥	4.57×10^{-3}	8.2×10^{3}	-28.0
75%∥	4.67×10^{-3}	5.0×10^{3}	-31.4
75%⊥	4.34×10^{-3}	6.0×10^{3}	-30.0
100%∥	3.94×10^{-3}	7.0×10^{3}	-32,0
100%⊥	3.78×10^{-3}	4.1×10^{3}	-28.4

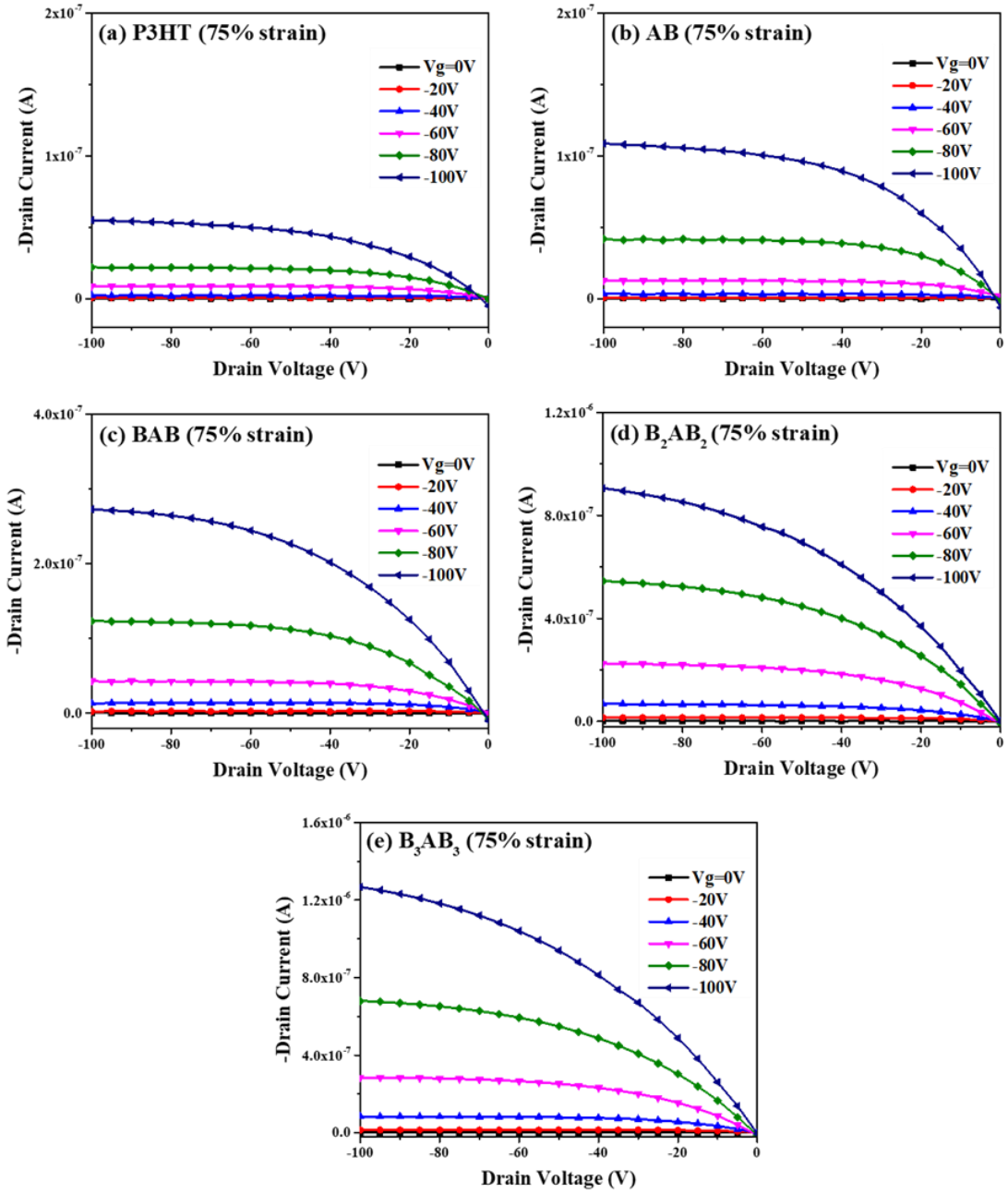

Fig. 2.23 Output characteristics of the OFETs made by the stretched and transferred (a) α,ω-P3HT (P3HT), (b) P3HT-*b*-PDL (AB), (c) PDL-*b*-P3HT-*b*-PDL (BAB), (d) PDL_2-*b*-P3HT-*b*-PDL_2 (B_2AB_2) and (e) PDL_3-*b*-P3HT-*b*-PDL_3 (B_3AB_3) films at 75% strain (parallel to strain direction).

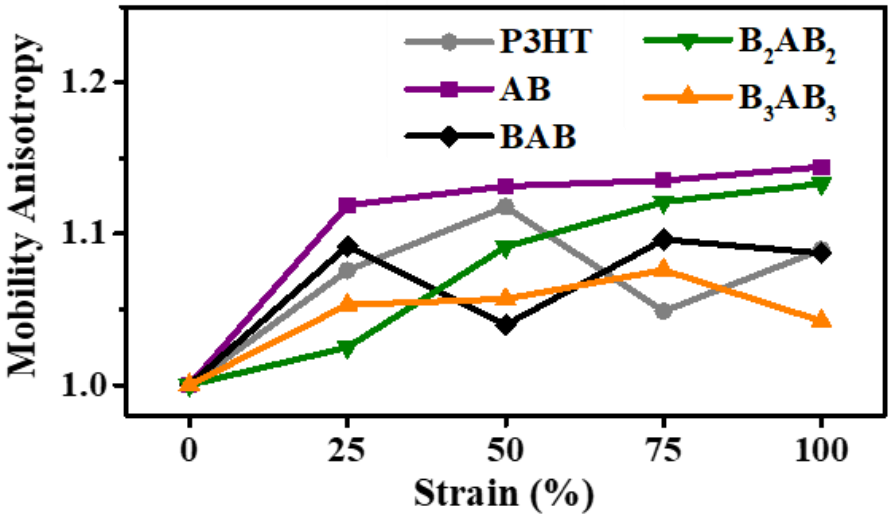

Fig. 2.24 Mobility anisotropy at different strain level calculated by the ratio between charge mobility with charge transporting channel parallel and perpendicular to strain direction.

As shown in **Fig. 2.22j**, the OFETs made by all the P3HT-*b*-PDLs exhibit charge mobility from 5.25×10^{-3} $cm^2V^{-1}S^{-1}$ to 7.14×10^{-3} cm^2 $V^{-1}S^{-1}$ under 0% strain, which is slightly lower than the P3HT device (1.05×10^{-2} $cm^2V^{-1}S^{-1}$). The charge mobility of the OFETs made by α,ω-P3HT, P3HT-*b*-PDL, PDL-*b*-P3HT-*b*-PDL, PDL_2-*b*-P3HT-*b*-PDL_2, and PDL_3-*b*-P3HT-*b*-PDL_3 at 50% strain are 9.93×10^{-4} $cm^2V^{-1}S^{-1}$ (⊥) - 1.11×10^{-3} $cm^2V^{-1}S^{-1}$ (∥), 1.52×10^{-3} $cm^2V^{-1}S^{-1}$ (⊥) - 1.72×10^{-3} $cm^2V^{-1}S^{-1}$ (∥), 2.01×10^{-3} $cm^2V^{-1}S^{-1}$ (⊥) - 2.09×10^{-3} $cm^2V^{-1}S^{-1}$ (∥), 3.50×10^{-3} $cm^2V^{-1}S^{-1}$ (⊥) - 3.82×10^{-3} $cm^2V^{-1}S^{-1}$ (∥), and 4.57×10^{-3} $cm^2V^{-1}S^{-1}$ (⊥) - 4.83×10^{-3} $cm^2V^{-1}S^{-1}$ (∥), respectively, showing that all the BCP devices exhibit higher performance than the pristine P3HT device at 50% strain. Moreover, charge mobilities of the branched block polymers (PDL_2-*b*-P3HT-*b*-PDL_2 and PDL_3-*b*-P3HT-*b*-PDL_3) become higher than the linear BCPs (AB and BAB) at 50% strain because of the enhanced stretchability of the polymer films. The charge

mobility of the PDL_2-*b*-P3HT-*b*-PDL_2 continually decreases to 2.48×10^{-3} $cm^2V^{-1}S^{-1}$ (⊥) - 2.78×10^{-3} $cm^2V^{-1}S^{-1}$ (∥) at 75% strain and significantly drops to 9.53×10^{-4} $cm^2V^{-1}S^{-1}$ (⊥) - 1.08×10^{-3} $cm^2V^{-1}S^{-1}$ (∥) at 100% strain, which may be due to the localized cracks formed at 75% strain and those cracks become continuous at 100% strain. On top of that, no significant decrease of the charge mobility is found in the OFET made by PDL_3-*b*-P3HT-*b*-PDL_3 under every stretching condition, and the charge mobility at 100% strain are 3.78×10^{-3} $cm^2V^{-1}S^{-1}$ (⊥) - 3.94×10^{-3} $cm^2V^{-1}S^{-1}$ (∥). It is correlated with the studies on the mechanical properties of PDL_3-*b*-P3HT-*b*-PDL_3, which possesses the lowest modulus among all the prepared polymers and show no continuous cracks observed by OM at 100% strain. The mobility retentions (**Fig. 2.22k**) of *α,ω*-P3HT, P3HT-*b*-PDL, PDL-*b*-P3HT-*b*-PDL, PDL_2-*b*-P3HT-*b*-PDL_2 and PDL_3-*b*-P3HT-*b*-PDL_3 at 100% strain in the parallel and perpendicular cases (∥, ⊥) are (2.5, 2.3), (6.8, 5.9), (9.2, 8.5), (16.7, 14.8) and (75.0, 72.0), respectively, indicating the superior charge mobility retention of B_3AB_3 type BCP under strain conditions.

Finally, the device performance of the OFETs made by PDL-*b*-P3HT-*b*-PDL and PDL_3-*b*-P3HT-*b*-PDL_3 under 0-500 stretch-release cycles at 50% strain was evaluated. I_{ds}-V_g curves of the devices after cycling test are provided in **Fig. 2.25a-d**, and the device performance is summarized in **Table 2.5**. **Fig. 2.25e** summarize the charge mobility of these two devices after cycling test. As can be seen, the charge mobility of the PDL-*b*-P3HT-*b*-PDL device drastically dropped from 6.92×10^{-3} cm^2 V^{-1} S^{-1} to 1.52×10^{-4} $cm^2V^{-1}S^{-1}$ (⊥) - 1.68×10^{-4} cm^2 $V^{-1}S^{-1}$ (∥) after

500 cycles. On the other hand, charge mobility of the PDL_3-*b*-P3HT-*b*-PDL_3 device dropped marginally from 5.25×10^{-3} $cm^2V^{-1}S^{-1}$ to 3.72×10^{-3} $cm^2V^{-1}S^{-1}$ (⊥) (perpendicular) - 3.93×10^{-3} $cm^2V^{-1}S^{-1}$ (∥). Unlike the BAB device show poor mobility retention (3%) after the cycling test, the B_3AB_3 device exhibit 71%-75% mobility retention after 500 stretch-release cycles (**Fig. 2.25f**), showing the excellent performance of the OFET made by the highly branched BCP. Note that among all the studied BCPs in this study, B_3AB_3 polymer has the best stretchability, while showing slightly lower charge mobility (0.045 cm^2 V^{-1} S^{-1}) before being stretched and transferred. In addition, B_2AB_2 has good charge mobility (0.089 cm^2 V^{-1} S^{-1}) with the same level as linear BCPs, but stretchability is not as good as B_3AB_3. This result reveals a trade-off between stretchability and semiconducting property of conjugated BCP in my architecture design. Aside from improving solution process, the author suggests to further increase P3HT weight ratio in B_3AB_3 polymer, or to decrease P3HT weight ratio in B_2AB_2 polymer to reach optimum conditions for making high-performance and stretchable semiconductor.

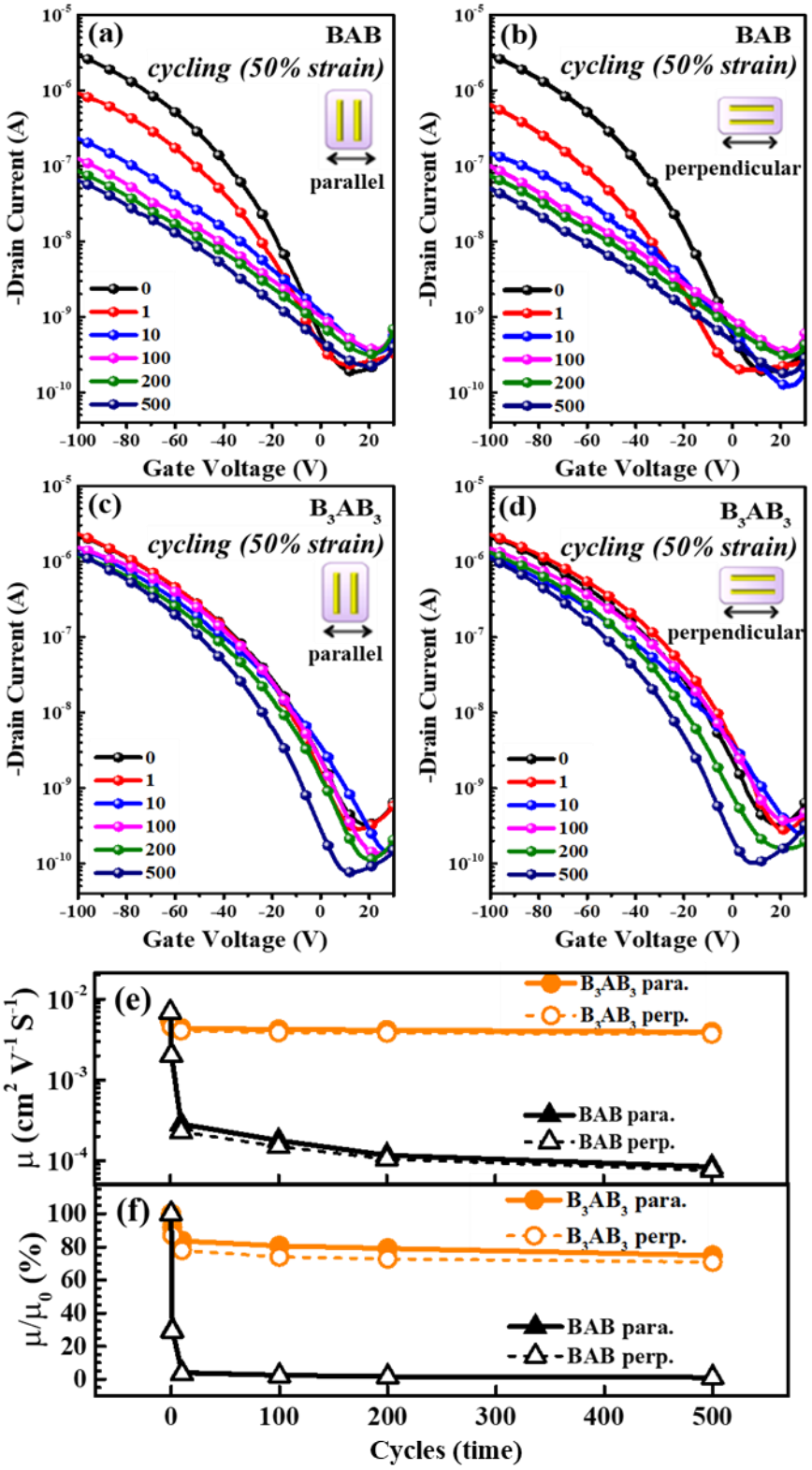

Fig. 2.25 I_{ds}-V_g curves of the (a, b) PDL-*b*-P3HT-*b*-PDL (BAB) and (c, d) PDL_3-*b*-P3HT-*b*-PDL_3 (B_3AB_3) devices after 0-500 stretch-release cycles at 50% strain ((a, c): parallel, (b, d): perpendicular). (e) Charge mobility (μ) and (f) mobility retentions (μ/μ_0) of the devices after stretch-release cycles.

Table 2.5 OFET performance of the devices made by PDL-*b*-P3HT-*b*-PDL (BAB) and PDL_3-*b*-P3HT-*b*-PDL_3 (B_3AB_3) films after 0-500 stretch-release cycles at 50% strain.

	BAB			**B_3AB_3**		
cycles	**μ ($cm^2 V^{-1} s^{-1}$)**	**on/off (-)**	**V_{on} (V)**	**μ ($cm^2 V^{-1} s^{-1}$)**	**on/off (-)**	**V_{on} (V)**
0	6.92×10^{-3}	1.6×10^{4}	-34.2	5.25×10^{-3}	6.8×10^{3}	-30.3
1∥	2.09×10^{-3}	3.9×10^{3}	-31.8	4.83×10^{-3}	8.1×10^{3}	-34.7
1⊥	2.01×10^{-3}	3.2×10^{3}	-35.2	4.57×10^{-3}	8.2×10^{3}	-28.0
10∥	5.22×10^{-4}	6.9×10^{2}	-33.0	4.39×10^{-3}	1.0×10^{4}	-30.5
10⊥	4.77×10^{-4}	1.2×10^{3}	-23.4	4.09×10^{-3}	4.7×10^{3}	-30.3
100∥	3.56×10^{-4}	3.3×10^{2}	-36.3	4.23×10^{-3}	1.2×10^{4}	-22.9
100⊥	3.01×10^{-4}	2.8×10^{2}	-36.9	3.88×10^{-3}	4.1×10^{3}	-22.8
200∥	2.34×10^{-4}	2.7×10^{2}	-33.6	4.15×10^{-3}	1.0×10^{4}	-27.6
200⊥	2.10×10^{-4}	2.5×10^{2}	-35.5	3.82×10^{-3}	8.4×10^{3}	-29.2
500∥	1.68×10^{-4}	2.9×10^{2}	-35.9	3.93×10^{-3}	1.7×10^{4}	-34.9
500⊥	1.52×10^{-4}	2.8×10^{2}	-36.9	3.72×10^{-3}	1.1×10^{4}	-36.7

2.4 Summary

I have synthesized poly(3-hexylthiophene)-*block*-poly(*δ*-decanolactone)s with AB, BAB, B_2AB_2, and B_3AB_3 architectures, and investigated their thermal properties, mechanical properties and the OFET devices. Through the selective solvent process, smooth BCP thin films with a well-defined P3HT nanofibrillar structure were achieved, leading to outstanding device performance of the field-effect transistors made by the BCPs with charge mobility from 0.045 $cm^2V^{-1}S^{-1}$ to 0.089 $cm^2V^{-1}S^{-1}$. Moreover, the triblock copolymer with branched soft segments (PDL_2-*b*-P3HT-*b*-PDL_2 and PDL_3-*b*-P3HT-*b*-PDL_3) were considered to possess smaller P3HT crystallites and more random phase separation judged from DSC heating curves and GIXS experiments. Consequently, these polymers exhibited lower elastic modulus and higher stretchability for enduring a higher strain level. Studied from the OFETs made by the stretched and transferred polymer thin films, the PDL_3-*b*-P3HT-*b*-PDL_3 device could maintain 72-75% of its charge mobility under 100% strain, as well as 71-75% of its charge mobility after 500 stretch-release cycles at 50% strain, suggesting the best semiconducting property under strain conditions among all the studied BCPs. This study provides a new way to advance stretchability of semiconducting polymer without sacrificing charge mobility by the architecture design of conjugated/elastic BCPs.

2.5 Reference

1. C. Ban, X. Wang, Z. Zhou, H. Mao, S. Cheng, Z. Zhang, Z. Liu, H. Li, J. Liu and W. Huang, *Sci. Rep.*, 2019, **9**, 1-7.
2. J. A. Rogers, T. Someya and Y. Huang, *Science*, 2010, **327**, 1603-1607.
3. G. J. N. Wang, A. Gasperini and Z. Bao, *Adv. Electron. Mater.*, 2018, **4**, 1700429.
4. T. Q. Trung and N. E. Lee, *Adv. Mater.*, 2017, **29**, 1603167.
5. M. Shin, J. Y. Oh, K. E. Byun, Y. J. Lee, B. Kim, H. K. Baik, J. J. Park and U. Jeong, *Adv. Mater.*, 2015, **27**, 1255-1261.
6. J. Xu, S. Wang, G.-J. N. Wang, C. Zhu, S. Luo, L. Jin, X. Gu, S. Chen, V. R. Feig and J. W. To, *Science*, 2017, **355**, 59-64.
7. J.-S. Kim, J.-H. Kim, W. Lee, H. Yu, H. J. Kim, I. Song, M. Shin, J. H. Oh, U. Jeong and T.-S. Kim, *Macromolecules*, 2015, **48**, 4339-4346.
8. S. Y. Son, J.-H. Kim, E. Song, K. Choi, J. Lee, K. Cho, T.-S. Kim and T. Park, *Macromolecules*, 2018, **51**, 2572-2579.
9. B. O'Connor, E. P. Chan, C. Chan, B. R. Conrad, L. J. Richter, R. J. Kline, M. Heeney, I. McCulloch, C. L. Soles and D. M. DeLongchamp, *Acs Nano*, 2010, **4**, 7538-7544.
10. B. Roth, S. Savagatrup, N. V. de los Santos, O. Hagemann, J. E. Carlé, M. Helgesen, F. Livi, E. Bundgaard, R. R. Søndergaard and F. C. Krebs, *Chem. Mater.*, 2016, **28**, 2363-2373.
11. J.-T. Wang, K. Saito, H.-C. Wu, H.-S. Sun, C.-C. Hung, Y. Chen, T. Isono, T. Kakuchi, T. Satoh and W.-C. Chen, *NPG Asia Mater.*, 2016, **8**, e298.
12. J.-T. Wang, S. Takshima, H.-C. Wu, C.-C. Shih, T. Isono, T. Kakuchi, T. Satoh and W.-C. Chen, *Macromolecules*, 2017, **50**, 1442-1452.
13. H.-C. Hsieh, C.-C. Hung, K. Watanabe, J.-Y. Chen, Y.-C. Chiu, T. Isono, Y.-C. Chiang, R. R. Reghu, T. Satoh and W.-C. Chen, *Polym. Chem.*, 2018, **9**, 3820-3831.
14. Y.-C. Chiang, S. Kobayashi, T. Isono, C.-C. Shih, T. Shingu, J.-J. Hung, H.-C. Hsieh, S.-H. Tung, T. Satoh and W.-C. Chen, *Polym. Chem.*, 2019, **10**, 5452-5464.
15. R. Peng, B. Pang, D. Hu, M. Chen, G. Zhang, X. Wang, H. Lu, K. Cho and L. Qiu, *J. Mater. Chem. C*, 2015, **3**, 3599-3606.
16. T. Higashihara, S. Fukuta, Y. Ochiai, T. Sekine, K. Chino, T. Koganezawa and I. Osaka, *ACS Appl. Polym. Mater.*, 2019, **1**, 315-320.
17. F. Ge, Z. Liu, F. Tian, Y. Du, L. Liu, X. Wang, H. Lu, Z. Wu, G. Zhang and L. Qiu, *Polym. Chem.*, 2018, **9**, 4517-4522.
18. M. T. Martello, A. Burns and M. Hillmyer, *ACS Macro Lett.,* 2012, **1**, 131-135.
19. T. Isono, B. J. Ree, K. Tajima, R. Borsali and T. Satoh, *Macromolecules*, 2018, **51**, 428-437.
20. K. Makiguchi, T. Satoh and T. Kakuchi, *Macromolecules*, 2011, **44**, 1999-2005.

21. T. Isono, I. Otsuka, Y. Kondo, S. Halila, S. Fort, C. Rochas, T. Satoh, R. Borsali and T. Kakuchi, *Macromolecules*, 2013, **46**, 1461-1469.
22. A. E. Speers, G. C. Adam and B. F. Cravatt, *J. Am. Chem. Soc.*, 2003, **125**, 4686-4687.
23. R. J. Kline, M. D. McGehee, E. N. Kadnikova, J. Liu and J. M. Frechet, *Adv. Mater.*, 2003, **15**, 1519-1522.
24. R. J. Kline, M. D. McGehee, E. N. Kadnikova, J. Liu, J. M. Fréchet and M. F. Toney, *Macromolecules*, 2005, **38**, 3312-3319.
25. Y. Ito, A. A. Virkar, S. Mannsfeld, J. H. Oh, M. Toney, J. Locklin and Z. Bao, *J. Am. Chem. Soc.*, 2009, **131**, 9396-9404.
26. A. Labuda, M. Kocuń, W. Meinhold, D. Walters and R. Proksch, *Beilstein J. Nanotechnol.*, 2016, **7**, 970-982.
27. H. K. Nguyen, M. Ito and K. Nakajima, *Jpn. J. Appl. Phys.*, 2016, **55**, 08NB06.
28. Z. N. Mahani and M. Tajvidi, *Int. J. Adhes. Adhes.*, 2017, **79**, 59-66.
29. J. Tang and E. Y. X. Chen, *J. Polym. Sci., Part A: Polym. Chem.*, 2018, **56**, 2271-2279.
30. M. Hong and E. Y.-X. Chen, *Nat. Chem.*, 2016, **8**, 42.
31. P. Kohn, S. Huettner, H. Komber, V. Senkovskyy, R. Tkachov, A. Kiriy, R. H. Friend, U. Steiner, W. T. Huck and J.-U. Sommer, *J. Am. Chem. Soc.*, 2012, **134**, 4790-4805.
32. G. Strobl, *Prog. Polym. Sci.*, 2006, **31**, 398-442.
33. H. Park, B. S. Ma, J.-S. Kim, Y. Kim, H. J. Kim, D. Kim, H. Yun, J. Han, F. S. Kim and T.-S. Kim, *Macromolecules*, 2019, **52**, 7721-7730.
34. J. Park, C. Choi, S. Hyun, H. C. Moon, K. L. Vincent Joseph and J. K. Kim, *Macromolecules*, 2016, **49**, 616-623.
35. H. Lim, C.-Y. Chao and W.-F. Su, *Macromolecules*, 2015, **48**, 3269-3281.
36. M. Alizadehaghdam, B. Heck, S. Siegenführ, F. Abbasi and G. n. Reiter, *Macromolecules*, 2019, **52**, 2487-2494.
37. M. Roesing, J. Howell and D. Boucher, *J. Polym. Sci., Part B: Polym. Phys.*, 2017, **55**, 1075-1087.
38. O. Inganäs, W. Salaneck, J.-E. Österholm and J. Laakso, *Synth. Met.*, 1988, **22**, 395-406.
39. L. He, S. Pan and J. Peng, *J. Polym. Sci., Part B: Polym. Phys.*, 2016, **54**, 544-551.
40. H. Yamagata and F. C. Spano, *J. Chem. Phys.*, 2012, **136**, 184901.
41. B. O'Connor, R. J. Kline, B. R. Conrad, L. J. Richter, D. Gundlach, M. F. Toney and D. M. DeLongchamp, *Adv. Funct. Mater.*, 2011, **21**, 3697-3705.
42. J. Mai, T.-K. Lau, J. Li, S.-H. Peng, C.-S. Hsu, U.-S. Jeng, J. Zeng, N. Zhao, X. Xiao and X. Lu, *Chem. Mater.*, 2016, **28**, 6186-6195.

Chapter 3

Poly(9,9-di-n-hexyl-2,7-fluorene)-block-poly(δ-decanolactone)s: Effect of Soft Segment Branching on Electronic Properties of Stretchable Polymer Electret

3.1 Background

Memory device is an essential part in wearable electronic gadgets due to the requirements of data storage and monitoring in such applications. Such device should be able endure a certain degree of mechanical deformation while maintaining its memory performance.[1, 2] Among various types of organic memory devices, organic field-effect transistor (OFET) memories are particularly attractive owing to their non-destructive read-out and manufacturing compatibility with integrated circuits composed of OFETs. OFET memories are also low-cost, light-weight, and offer mechanical flexibility and solvent processibility, which are expected to provide excellent alternatives to traditional Si-based memories.[3, 4] An OFET memory cell is a conventional transistor with a charge-storage layer sandwiched between an organic semiconducting layer and a dielectric layer. The charge-storage layer is the key component in OFET memory since it can trap positive or negative charges through an additional electric field (gate bias). Therefore, charge distribution in the semiconducting layer can be changed to modulate its high conducting and low conducting states.[5]

Three major types of charge-trapping materials that have been widely used as the charge-storage layer of OFET memories are metallic nano-floating-gate dielectrics,[6, 7] organic ferroelectric materials,[8, 9] and polymer electrets.[10, 11] Polymer-based electrets have drawn tremendous research attention recently, owing to their advanced mechanical properties and flexibility in terms of chemical structural design.[12] Among various kinds of polymer electrets,

polyfluorene-based materials are particularly promising due to desirable energy levels and charge-trapping ability. Several processing or synthetic strategies, such as conjugated/insulating polymer blends,[13, 14] self-doped nanostructures of polyfluorene,[15] pendent fluorene moieties with different conjugation length,[16] and polyfluorene-based block copolymers (BCPs),[17] have been proposed to facilitate charge-trapping within polymer thin films. However, as a result of the rigid polymer backbone of conjugated polymers, the materials in the above examples are still incapable of enduring high mechanical strain for stretchable device applications.

To improve the mechanical properties of conjugated polymers, one useful strategy is to create BCPs with conjugated and soft elastic blocks. For example, polythiophene-based conjugated/elastic BCPs have been developed as stretchable semiconducting materials.[18-20] The incorporated soft segments provide a degree of freedom for the movement of polymer chains, leading to enhanced mechanical properties of the conjugated polymers. In a more relevant study on polyfluorene, a linear diblock copolymer consisting of poly(9,9-di-*n*-hexyl-2,7-fluorene) and poly(*n*-butyl acrylate) (PF-*b*-PBA) was synthesized to investigate the effect of stress on the optical properties of the BCP.[21] However, polyfluorene-based BCPs as polymer electrets for stretchable OFET memory applications have not yet been reported.

In this chapter, I demonstrate novel stretchable polyfluorene-based miktoarm BCPs as hole-trapping materials. The incorporated soft segments with different structures are expected

to not only provide elastic properties but also tailor phase separation and charge trapping sites within the polymer thin films. A series of polyfluorene-based linear and branched BCPs containing poly(9,9-di-*n*-hexyl-2,7-fluorene) (PF) and poly(δ-decanolactone) (PDL), denoted as PF-*b*-PDL, PF-*b*-PDL$_2$, and PF-*b*-PDL$_3$, were designed as the charge-storage layer of an n-type *N*,*N*′-dioctyl-3,4,9,10-perylenedicarboximide (PTCDI-C8)-based OFET memory. Note that PDL is a bio-based amorphous polymer with a glass transition temperature below -60 °C, which is an environmental-friendly candidate for creating BCPs with soft segments.[22] Also, I adopted diphenyl phosphate (DPP)-catalyzed ring-opening polymerization of δ-decanolactone as the metal-free and nontoxic method to synthesize PDL building blocks,[23-25] as mentioned in Chapter 1. The crystallization processes of the BCPs were investigated with differential scanning calorimetry (DSC), and the energy levels were determined by UV-vis absorption spectroscopy and cyclic voltammetry (CV). Moreover, I propose a new protocol to correlate the film morphology of the BCP electret with its charge-trapping properties. The PF nanofibers confined within an insulting polymer matrix are regarded as efficient hole-trapping sites in the polymer electret.[17] In the present study, I quantitatively analyzed the width (W), length (L) and coverage area (A%) of the PF nanofibers within the BCP thin films using atomic force microscopy (AFM) phase images, and those features were correlated with the charge trapping density of the OFET memories. This method is useful for evaluating nanostructures of BCP thin films for advanced device applications. In the last section, I investigated the stretchability

of the polymer thin films using optical microscopy (OM). OFET memory devices fabricated with the stretched and transferred charge-storage layer were also examined to assess the performance of the charge-trapping materials under stretching conditions.

3.2 Experimental Section

3.2.1 Materials

Tetrahydrofuran (THF, anhydrous, ≥99.9%), methanol (MeOH, anhydrous, 99.8%), toluene (≥99.8%), *N*,*N*,*N*',*N*'',*N*''-pentamethyldiethylenetriamine (PMDETA, 99%), copper(I) bromide (CuBr, 98%), trichloroethylene (TCE, anhydrous, ≥99%), ammonium hydroxide solution (ammonia water, 28.0-30.0%), PTCDI-C8 (98%), and polydimethylsiloxane (PDMS, Sylgard 184) were purchased from Sigma-Aldrich Co., Ltd.. *N*-octadecyltrichlorosilane (ODTS, 97%) was purchased from Gelest Inc.. *δ*-decanolactone (*δ*-DL) (synthetic and racemic compound) was purchased from Tokyo Chemical Industry Co., Ltd. and was purified by distillation over CaH_2 before being used.

3.2.2 Polymer Synthesis

The synthetic route for the target polymers is shown in **Scheme 3.1**. Alkyne functionalized PF (alkyne-PF) and azido functionalized PDLs (N_3-PDL_x, x = 1-3) were prepared as the building blocks for the target BCPs. AB, AB_2, and AB_3 type polymers (A = PF, B = PDL) were then synthesized via Cu-catalyzed azido–alkyne click reaction (CuAAC) between alkyne-PF

and N_3-PDL_x (x = 1-3) homopolymers.

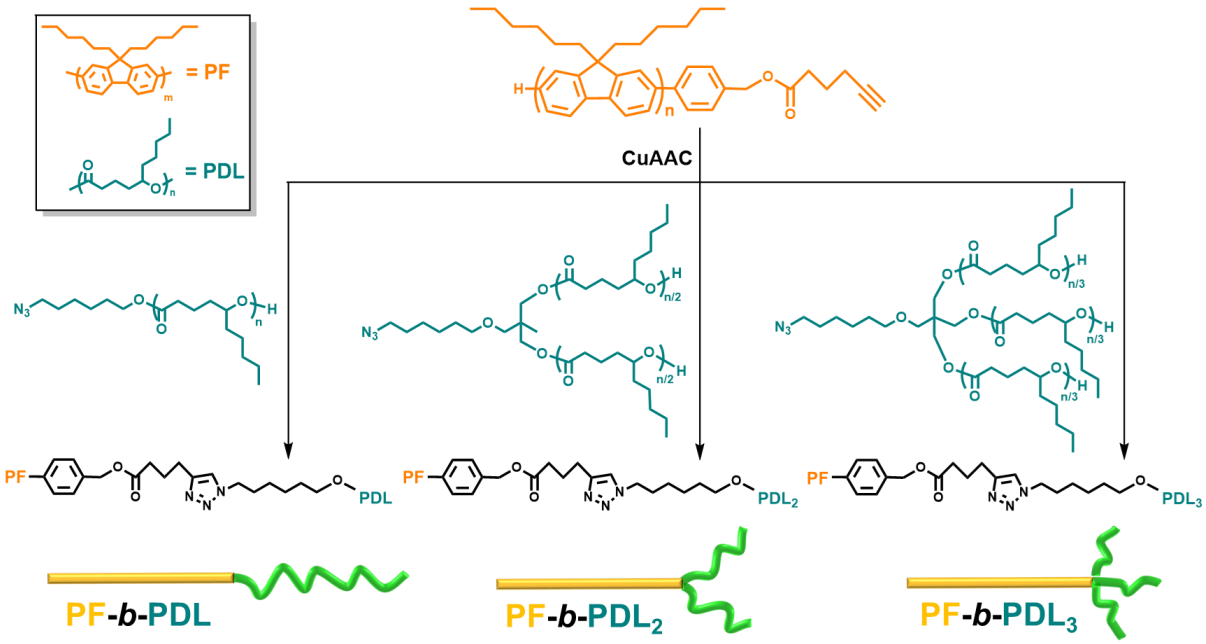

Scheme 3.1 Synthetic route for PF-*b*-PDL, PF-*b*-PDL_2, and PF-*b*-PDL_3.

Synthesis of alkyne-functionalized poly(9,9-di-*n*-hexyl-2,7-fluorene) (alkyne-PF). Poly(9,9-di-*n*-hexyl-2,7-fluorene) with a benzyl alcohol group at α chain-end ($HOCH_2$-PF) was synthesized through modified Suzuki-Miyaura coupling polymerization according to previous report.[26] Esterification reaction between $HOCH_2$-PF and 5-hexynoic acid was then performed to achieve alkyne-functionalized PF (alkyne-PF).[27] The product was yellowish and powder-like solid. (357 mg, yield: 63%, yellow powder, $M_{n,NMR}$ (in $CDCl_3$) = 5400 g mol^{-1}, $M_{n,SEC}$ (in THF, calibrated with polystyrene standards) = 8600 g mol^{-1}, $Đ$ = 1.43.

Synthesis of linear, 2-armed, and 3-armed azido-functionalized PDLs. Azido-

functional PDLs with linear, two-armed and three-armed architectures were synthesized based on the DPP-catalyzed living ring-opening polymerization as illustrated in Chapter 2.[28] **Linear PDL (N_3-PDL):** The product was viscous transparent liquid (1170 mg, yield: 81%, $M_{n,NMR}$ (in $CDCl_3$) = 5100 g mol^{-1}, $M_{n,SEC}$ (in THF, calibrated with polystyrene standards) = 7200 g mol^{-1}, $Đ$ = 1.09). **Two-armed PDL (N_3-PDL_2):** The product was viscous and transparent liquid (1054 mg, 70%, $M_{n,NMR}$ = 5000 g mol^{-1}, $M_{n,SEC}$ = 6600 g mol^{-1}, $Đ$ = 1.13). **Three-armed PDL (N_3-PDL_3 (5k)):** The product was viscous and transparent liquid (1345 mg, 67%, $M_{n,NMR}$ = 5100 g mol^{-1}, $M_{n,SEC}$ = 6400 g mol^{-1}, $Đ$ = 1.14.). solvent information

Synthesis of PF-*b*-PDLs by click reaction. The click reaction between the alkyne-functional PF and azido-functionalized PDL was performed in anhydrous THF. I take PF-*b*-PDL as an example to explain the procedure in detail. PF (100 mg, 19 μmol) and CuI (10.6 mg, 56 μmol) were put in a Schlenk flask and dried for at least 30 min. N_3-PDL with 1.2 equivalent to PF (113 mg, 22.2 μmol), PMDETA (19.3 μL, 11.1 μmol), and anhydrous THF (3 mL) were mixed and the oxygen were removed by three freeze-drying cycles. The reaction flask was stirred for 2 days in at 50 °C. The polymer solution was diluted by THF and purified by an Al_2O_3 column to remove the metallic catalyst. Then the solution was evaporated and precipitated in a cold MeOH/acetone solution. The precipitate was dried under vacuum to achieve the final product.

PF-*b*-PDL: 134 mg, yield: 63%, yellow solid, $M_{n,NMR}$ (in $CDCl_3$) = 10500 g mol^{-1}, $M_{n,SEC}$

(in THF, calibrated with polystyrene standards) = 12800 g mol^{-1}, $Đ$ = 1.41. ^{1}H NMR (400 MHz, $CDCl_3$, δ (ppm)): δ (ppm) 7.56-7.94 (m, Ar-H of PF backbone), 2.13 (m, **PF** side chain -C-($CH_2C_5H_{11}$)$_2$), 0.79-1.10 (m, **PF** side chain -C-($CH_2C_5H_{11}$)$_2$, **PDL** side chain-$CHC_4H_8CH_3$), 4.87 (m, **PDL** main chain -$COOC_3H_6CH$), 2.29 (t, **PDL** main chain-$COOCH_2C_2H_4CH$), 1.08-1.90 (m, **PDL** main chain -$COOCH_2$-C_2H_4CH, **PDL** side chain-$CC_4H_8CH_3$), 3.59 (m, **PDL** chain end -C*H*OH), 5.09 (s, PF-CH_2O-), 4.16 (t, PDL-O-$C_5H_{10}CH_2$), 2.81 (t, PF-$CH_2OCOC_2H_4CH_2$-), 2.23 (t, PF-CH_2OCOCH_2-), 1.91 (m, PF-$CH_2OCOCH_2CH_2$-), 4.03 (t, PDL-O-CH_2).

PF-*b*-PDL$_2$: 119 mg, yield: 58%, yellow solid, $M_{n,NMR}$ (in $CDCl_3$) = 10400 g mol^{-1}, $M_{n,SEC}$ (in THF, calibrated with polystyrene standards) = 11700 g mol^{-1}, $Đ$ = 1.46. ^{1}H NMR (400 MHz, $CDCl_3$, δ (ppm)): δ (ppm) 7.56-7.94 (m, Ar-H of PF backbone), 2.13 (m, **PF** side chain -C-($CH_2C_5H_{11}$)$_2$), 0.79-1.10 (m, **PF** side chain -C-($CH_2C_5H_{11}$)$_2$, **PDL** side chain-$CHC_4H_8CH_3$), 4.87 (m, **PDL** main chain -$COOC_3H_6CH$), 2.29 (t, **PDL** main chain-$COOCH_2C_2H_4CH$), 1.08-1.90 (m, **PDL** main chain -$COOCH_2$-C_2H_4CH, **PDL** side chain-$CC_4H_8CH_3$), 3.59 (m, **PDL** chain end -C*H*OH), 5.09 (s, PF-CH_2O-), 4.16 (t, PDL-O-$C_5H_{10}CH_2$), 2.81 (t, PF-$CH_2OCOC_2H_4CH_2$-), 2.23 (t, PF-CH_2OCOCH_2-), 1.91 (PF-$CH_2OCOCH_2CH_2$-), 3.97 (s, PDL-OCH_2) 3.39 (t, N_3-$C_5H_{10}CH_2$), 3.22(s, -$N_3C_6H_{12}OCH_2$-).

PF-*b*-PDL$_3$: 145 mg, yield: 70%, yellow solid, $M_{n,NMR}$ (in $CDCl_3$) = 10500 g mol^{-1}, $M_{n,SEC}$ (in THF, calibrated with polystyrene standards) = 11400 g mol^{-1}, $Đ$ = 1.43. ^{1}H NMR (400 MHz,

$CDCl_3$, δ (ppm)): δ (ppm) 7.56-7.94 (m, Ar-H of PF backbone), 2.13 (m, **PF** side chain -C-($CH_2C_5H_{11}$)$_2$), 0.79-1.10 (m, **PF** side chain -C-($CH_2C_5H_{11}$)$_2$, **PDL** side chain -$CHC_4H_8CH_3$), 4.87 (m, **PDL** main chain -$COOC_3H_6CH$), 2.29 (t, **PDL** main chain-$COOCH_2C_2H_4CH$), 1.08-1.90 (m, **PDL** main chain -$COOCH_2$-C_2H_4CH, **PDL** side chain-$CC_4H_8CH_3$), 3.59 (m, **PDL** chain end -C*H*OH), 5.09 (s, PF-CH_2O-), 4.16 (t, PDL-O-$C_5H_{10}CH_2$), 2.81 (t, PF-$CH_2OCOC_2H_4CH_2$-), 2.23 (t, PF-CH_2OCOCH_2-), 1.91 (PF-$CH_2OCOCH_2CH_2$-), 4.09 (s, PDL-OCH_2-), 3.38 (m, N_3-$C_5H_{10}CH_2$- and N_3-$C_5H_{10}CH_2OCH_2$-).

3.2.3 Characterization

Polymer structure characterization. Proton nuclear magnetic resonance (^{1}H NMR) spectra were recorded on a JEOL JNM-ECS400 400 MHz NMR spectrometer using deuterated chloroform. Size exclusion chromatography (SEC) measurements were performed at 40 °C using a Jasco GPC-900 system equipped with two Shodex KF-804L columns (8 mm × 300 mm) using THF as the eluent solvent at a flow rate of 1.0 mL·min^{-1}. Number-average molecular weight ($M_{n,SEC}$) and dispersity ($Đ$) of the polymers were calculated on the basis of a polystyrene standard. Fourier transform infrared spectroscopy (FTIR) measurements were performed using a PerkinElmer Frontier MIR spectrometer equipped with a single reflection diamond universal attenuated total reflection (ATR) accessory.

Thermal Properties. Thermal gravimetric analysis (TGA) was conducted using a TA

Instruments Q50 with a heating rate of 10 °C·min^{-1} from 100 °C to 650 °C under a flow of nitrogen. DSC measurements were conducted using a TA Instruments Q100 instrument in which 3-5 mg samples were measured with heating and cooling rates of 10 °C·min^{-1} between -70 °C and 235 °C.

Optical Properties, Electrical Properties, and Thin Film Morphology. Polymer thin films were prepared by spin-coating a polymer solution (3 g·L^{-1}) with a spin rate of 1000 rpm onto an octadecyltrichlorosilane (ODTS)-modified bare silicon wafer, quartz substrate, or indium tin oxide (ITO) glass. The ODTS-modified wafer was prepared by spin-coating a solution of ODTS in TCE (20 μL/20 mL, 3000 rpm) onto a UV-pretreated silicon wafer, followed by annealing with ammonia water for at least 24 h. The hydrophobic surface of the modified wafer facilitated the molecular packing and orientation of the polymer thin films.[28] The annealing process for the polymer thin films was carried out at 100 °C in a N_2-filled glovebox for 1 h. CV measurements was conducted with a CHI 627E electrochemical analyzer using a three-electrode cell system, with ITO glass used as the working electrode and a platinum wire as the auxiliary electrode. The Ag/AgCl, KCl (sat.) reference electrode was used to define the cell potential. Electrochemical properties of the polymer films were measured using 0.1 M tetrabutylammonium perchlorate in anhydrous acetonitrile as the electrolyte. Solid-state UV-vis absorption spectra were recorded with a Hitachi U-4100 spectrophotometer. Nanostructures of the polymer thin films were visualized with AFM using a Nanoscope 3D

controller atomic force microscope (Digital Instruments) operated in the tapping mode under an ambient atmosphere. The spring constant of the silicon cantilevers (Nanosensor PPP-SEIHR) was 15 N/m and the resonant frequency was 330 kHz. Quantitative analysis of the features of polyfluorene nanofibers was conducted by an open-source GT-Fiber software.[29] Grazing incidence wide angle X-ray scattering (GI-WAXS) measurements of the polymer films on ODTS-modified bare wafer substrates were conducted in the National Synchrotron Radiation Research Center in Taiwan (23A beamline) using an X-ray radiation source of λ = 1.239851 Å, and Pilatus 1M-F and C9728DK area detector. Cross-sectional Scanning Electron Microscope (SEM) images of the fabricated device were measured using a JSM-7600F Schottky Field Emission Scanning Electron Microscope. For the optical microscopy (OM) images of the stretched polymer films, films were first prepared on an ODTS-modified silicon wafer and then transferred to a cross-linked PDMS elastomeric substrate (reagent A:B = 20:1 (w/w)). The stretched polymer films were then transferred back to a second bare silicon wafer for the measurements, and the images were recorded using an OLYMPUS BX51 microscope.

Device Fabrication. Fabrication of n-type OFET memories with PTCDI-C8 as the semiconducting layer and the prepared PF-*b*-PDL$_x$ (x = 1-3) as the charge-storage layer (Si/SiO$_2$/PF-*b*-PDL$_x$/PTCDI-C8/Au) allowed us to investigate the charge-trapping properties of the prepared polymers. A 3 g·L^{-1} solution of PF-*b*-PDL$_x$ in toluene was spin-coated onto the ODTS-modified SiO$_2$ (300 nm)/Si substrates at a spin rate of 1000 rpm. The average film

thickness was 30-35 nm. The spin-casted polymer thin films were then thermally annealed at 100 °C for 1 h in a N_2-filled glovebox. Subsequently, 50 nm-thick PTCDI-C8 layer was thermally evaporated on top of the polymer layer. 50 nm-thick gold source and drain electrodes were then subsequently thermally evaporated through a regular shadow mask with channel length (L) and width (W) of 50 and 1000 μm, respectively. For the OFET memories prepared from the stretched polymer thin films, the thermally annealed polymer thin films developed on the ODTS-modified SiO_2/Si substrates were first transferred to a PDMS substrate (reagent A:B = 20:1 (w/w)), and then the polymer films on PDMS substrates were stretched at different strain levels and clamped on a glass substrate. The polymer films were then transferred to a silicon wafer with a 300 nm SiO_2 layer. Finally, the PTCDI-C8 and gold electrodes were deposited in the same manner as the procedures mentioned above. Current-voltage characteristics (I_{ds}-V_g) of the fabricated OFETs were recorded in a N_2-filled glovebox using a Keithley 4200 semiconductor parametric analyzer (Keithley Instruments Inc., Cleveland, OH).

3.3 Results and Discussion

3.3.1 Polymer Characterization

Molecular weight and $Đ$ values of the polymers used in this study are summarized in **Table 3.1**. Alkyne-PF and N_3-PDL_x (x = 1-3) were prepared according to previous literature[26, 28] with precise molecular weight control; the corresponding ^{1}H NMR spectra are shown in **Fig.**

3.1. The number-averaged molecular weight calculated from the ^{1}H NMR spectrum ($M_{n,NMR}$) of PF is 5400, and the $Đ$ value is 1.43. The $M_{n,NMR}$ values of N_3-PDL, N_3-PDL_2, and N_3-PDL_3 are 5100, 5000, and 5100, respectively, with $Đ$ values of 1.09, 1.13, and 1.14, respectively. Note that the number-averaged molecular weights calculated from the SEC traces ($M_{n,SEC}$) of N_3-PDL, N_3-PDL_2, and N_3-PDL_3 are 7200, 6600, and 6400, respectively. The lower $M_{n,SEC}$ of the branched PDLs indicates a smaller hydrodynamic volume. Since the PDL homopolymers exhibit nearly the same $M_{n,NMR}$ (5000-5100), it can be concluded that the branched PDLs possess higher relative density compared with the linear PDL. A CuAAC click reaction was then performed between alkyne-PF and the N_3-PDL_x to obtain the desired BCPs. As shown in **Fig. 3.2**, SEC traces of the BCPs clearly shift to higher molecular weight after the click reaction. The $M_{n,SEC}$ values of PF-*b*-PDL, PF-*b*-PDL_2, and PF-*b*-PDL_3 are 12800, 11700, and 11400, respectively. Compared with PF-*b*-PDL, the smaller $M_{n,SEC}$ values of PF-*b*-PDL_2 and PF-*b*-PDL_3 can be attributed to the smaller volume of the branched PDL building blocks. Moreover, $Đ$ values range from 1.41 to 1.46, showing that the molecular weight of the BCPs can be effectively controlled with the method provided in this work. The chemical structures of the BCPs were then confirmed by FTIR spectroscopy and ^{1}H NMR spectroscopy. In the FTIR spectrum of PF-*b*-PDL (**Fig. 3.3a**), an absorption band of the azido group from N_3-PDL at 2097 cm^{-1} completely disappears after the click reaction, indicating effective coupling between the alkyne and azido functional groups. Similar results were found for PF-*b*-PDL_2 and PF-*b*-PDL_3;

the corresponding FTIR spectra are provided in **Fig. 3.3b and c**. ^{1}H NMR spectra of the BCPs (**Fig. 3.4**) possess the signals from both PF (0.59-1.12 ppm, 1.96-2.11 ppm, and 7.50-7.94 ppm) and PDL blocks (1.10-1.80 ppm, 2.11-2.22 ppm, and 4.79-4.91 ppm). The portion of PDL connected to polyfluorene (*%P*) was estimated using the integration of the ^{1}H NMR signal at 2.13 ppm (m, **PF** side chain -C-(CH_2C$_5$H$_{11}$)$_2$) and 2.29 ppm (t, **PDL** main chain-COOCH_2C$_2$H$_4$CH) with the equation:

$$\%P = (A_{2.29} \div 2 \times N_{PDL}) \div [A_{2.13} \div 4 \times N_{PF}] \times 100\%,$$

where $A_{2.29}$ is intensity at 2.29 ppm, $A_{2.13}$ is intensity at 2.13 ppm, N_{PDL} is the number of repeat unit of PDL homopolymers, and N_{PF} is the number of repeat unit of PF homopolymer. The calculated *%P* values for the synthesis of PF-*b*-PDL, PF-*b*-PDL$_2$ and PF-*b*-PDL$_3$ are 94%, 93% and 97%, respectively, indicating satisfactory connection between PF and PDL segments. The combined results indicate that the synthesis of the target BCPs with controlled molecular weight and block ratio was successful. Note that the weight ratio of the PF block (w_{PF}) in all of the BCPs is controlled between 51.4% and 51.9% to assess the relationship between polymer architecture and polymer properties without any other effects originating from differences in the block ratios.

Table 3.1 Molecular weight parameters of the studied polymers.

sample	$M_{n,NMR}$ [a]	$M_{n,SEC}$ [b]	$Đ$ [b]	w_{PF} [c]
PF	5400	8600	1.43	100%
N_3-PDL	5100	7200	1.09	0%
N_3-PDL_2	5000	6600	1.13	0%
N_3-PDL_3	5100	6400	1.14	0%
PF-*b*-PDL	10500	12800	1.41	51.4%
PF-*b*-PDL_2	10400	11700	1.46	51.9%
PF-*b*-PDL_3	10500	11400	1.43	51.4%

[a] Calculated from ^{1}H NMR in $CDCl_3$. [b] Calculated from SEC traces in THF. [c] Weight ratio of the PF block in all of the BCPs calculated from ^{1}H NMR spectra of the studied polymers.

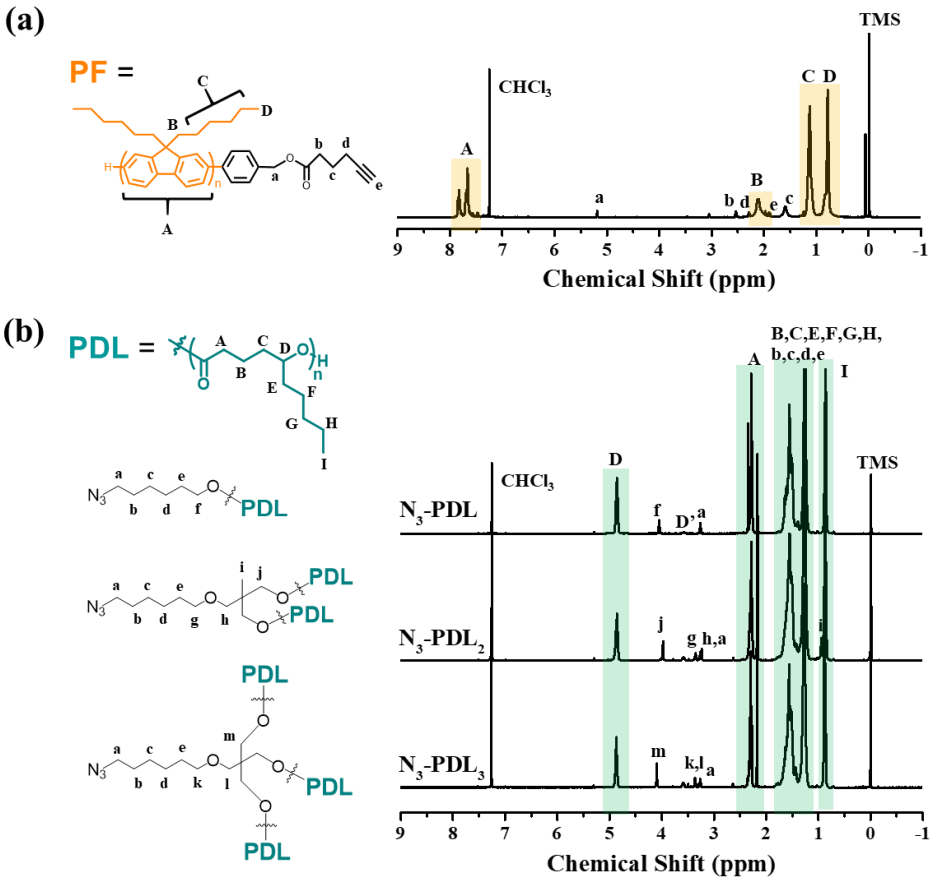

Fig. 3.1 ^{1}H NMR spectra of the (a) alkyne-PF and (b) N_3-PDL_x (x = 1-3).

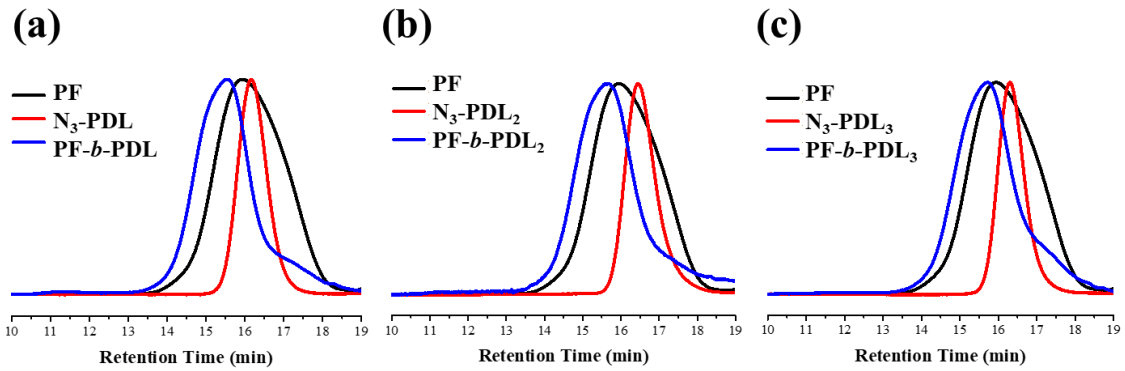

Fig. 3.2 SEC traces of (a) PF-*b*-PDL, (b) PF-*b*-PDL_2 and (c) PF-*b*-PDL_3 along with their starting materials.

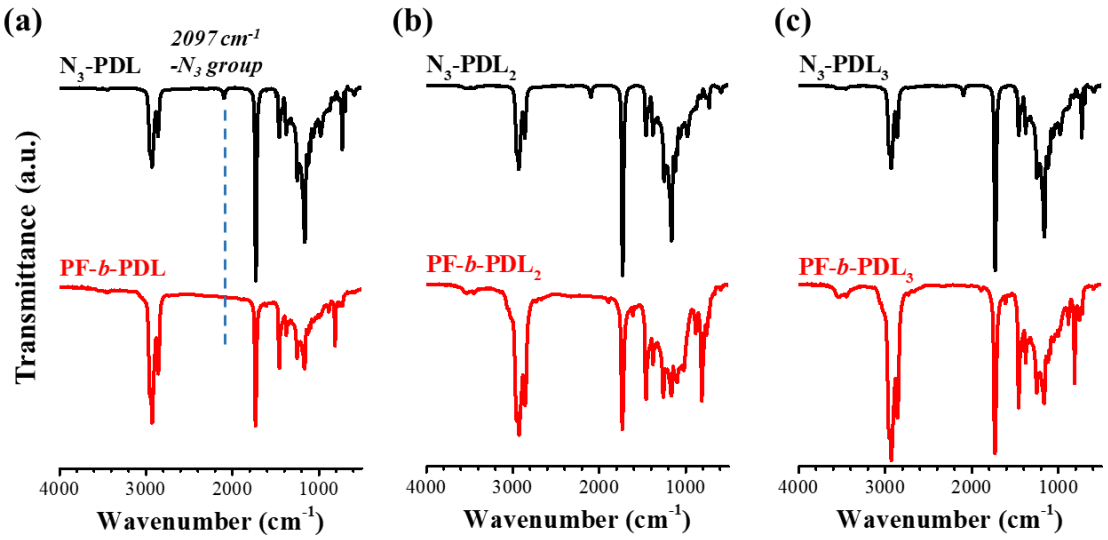

Fig. 3.3 FTIR spectra of (a) N_3-PDL_2, PF-*b*-PDL_2, (b) N_3-PDL_3 and PF-*b*-PDL_3.

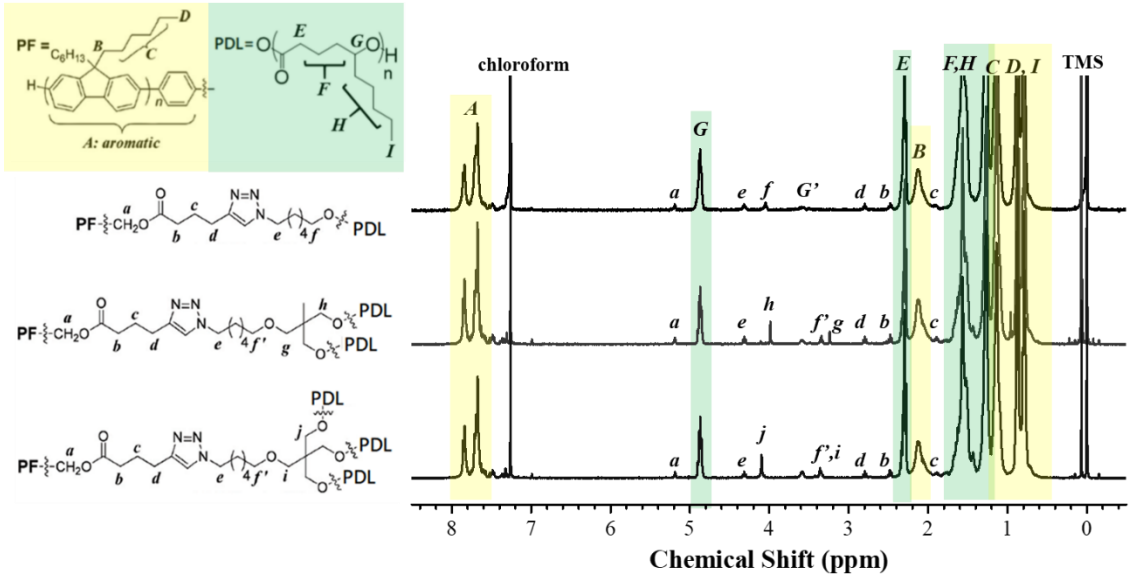

Fig. 3.4 ^{1}H NMR spectra (in $CDCl_3$) of PF-*b*-PDL, PF-*b*-PDL_2, and PF-*b*-PDL_3.

3.3.2 Thermal Properties

Thermal properties of the polymers were investigated, and the results are summarized in **Table 3.2**, **Fig. 3.5**, and **Fig. 3.6**. Thermal stability of the BCPs was determined from TGA traces recorded from 100 °C to 650 °C (**Fig. 3.5**). The BCPs exhibit two degradation temperatures ($T_{d,\ 5\%}$), at 290.2-297.1 °C and 375.0-380.8 °C, which represent the 5% degradation of the PDL block and the PF block, respectively. DSC measurements with a ramp rate of 10 °C/min under nitrogen flow were performed to investigate phase transitions of the studied polymers (**Fig. 3.6**). The DSC traces were recorded at temperatures up to 235 °C to prevent thermal decomposition of the PDL segments.

Table 3.2 Thermal and electrical properties of alkyne-PF, PF-*b*-PDL, PF-*b*-PDL_2, and PF-*b*-PDL_3.

sample	ΔH_c [a] (J/g)	$FWHM_c$ [a] (°C)	ΔH_m [b] (J/g)	HOMO [c] (eV)	LUMO [d] (eV)
alkyne-PF	-	-	-	-5.63	-2.73
PF-*b*-PDL	5.68	15.5	5.88	-5.63	-2.73
PF-*b*-PDL_2	6.83	14.6	7.04	-5.61	-2.71
PF-*b*-PDL_3	8.98	14.4	9.29	-5.61	-2.71

[a] Calculated from DSC first cooling curves (**Fig. 3.6a**). [b] Calculated from DSC second heating curves (**Fig. 3.6b**). [c] Calculated from the onset oxidation potential measured by CV (**Fig. 3.8**). [d] Calculated using the formula LUMO = HOMO + E_g. E_g was determined from the onset UV absorption (**Fig. 3.7b**) of the annealed polymer films.

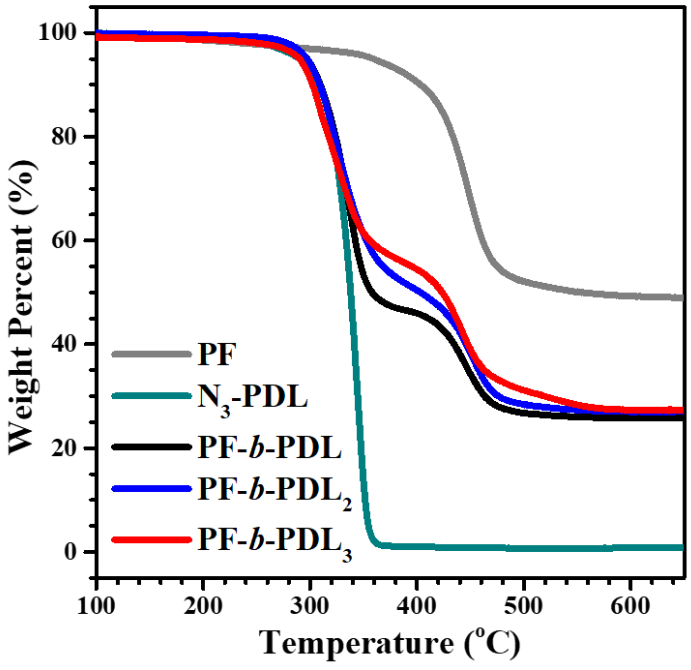

Fig. 3.5 TGA traces of the alkyne-PF (PF), N_3-PDL, PF-*b*-PDL, PF-*b*-PDL_2 and PF-*b*-PDL_3 (under nitrogen flow).

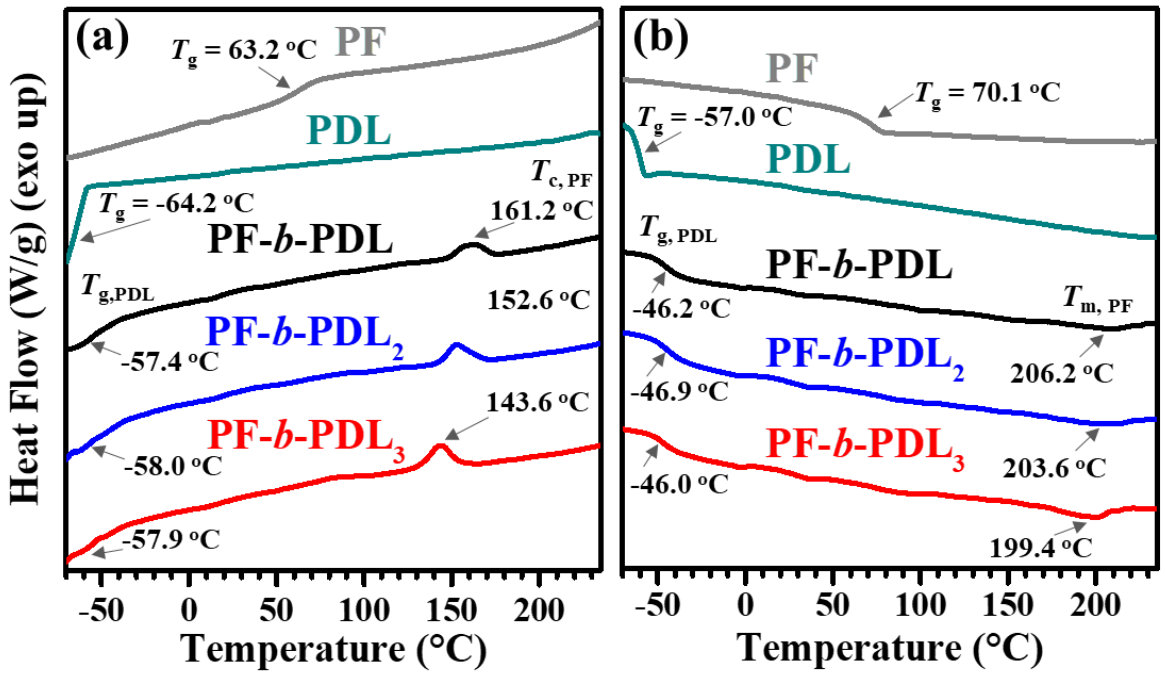

Fig. 3.6 DSC (a) first cooling and (b) second heating curves of alkyne-PF (PF), N_3-PDL (PDL), PF-*b*-PDL, PF-*b*-PDL$_2$, and PF-*b*-PDL$_3$.

The PF homopolymers (alkyne-PF) exhibits a significant glass transition temperature (T_g) at 63.2 °C in the first cooling curve (**Fig. 3.6a**) and at 70.1 °C in the second heating curve (**Fig. 3.6b**). No melting or crystallization peaks were identified in the cooling and heating curves, suggesting low crystallinity of the PF homopolymer. Compared with a previous report on poly(9,9-di-*n*-hexyl-2,7-fluorene) with a molecular weight of 45000 that exhibited high crystallinity,[30] the poor crystallinity of the PF homopolymer in this research can be explained by the low molecular weight of the sample. The PDL homopolymer (represented by N_3-PDL) exhibits a T_g at -64.2 °C in the first cooling curve and at -57.0 °C in the second heating curve, demonstrating the benefit of PDL as a soft building block of the BCP. All of the BCPs exhibit glass transition temperatures that vary between -58.0 °C and -57.4 °C during the first cooling,

and between -46.9 °C and -46.0 °C during the second heating, representing the glass transition temperature of the PDL segments in the BCPs ($T_{g,PDL}$). Conversely, the glass transition temperature of the PF segment is indistinguishable among all of the BCP samples. Instead of exhibiting a T_g of the PF segment, each BCP sample exhibits a sharp exothermic peak (143.6-161.2 °C) during the first cooling, and a broader endothermic peak (199.4-206.2 °C) during the second heating. These phase transitions can be regarded as the crystallization process and melting process of the PF crystalline phase, respectively.[30] This suggests that the PDL segments in the studied BCP system facilitate the crystallization process of the PF segment, which originally exhibits poor crystallinity as the homopolymer. Moreover, the much lower crystallization temperature ($T_{c,PF}$, **Fig. 3.6a**) of the branched BCPs can be attributed to the confined crystallization and homogeneous nucleation of the polymer.[31] Note that the crystalline structure of the PF segments in the BCPs was confirmed as the α crystalline form of poly(9,9-di-*n*-hexyl-2,7-fluorene)[30] by grazing-incidence wide-angle X-ray scattering (GI-WAXS) measurements, which will be discussed in the next section.

To investigate the kinetics of the crystallization process in more detail, the enthalpy of crystallization (ΔH_c), enthalpy of fusion (ΔH_m), and full width at half-maximum of crystallization ($FWHM_c$) were calculated and are summarized in **Table 3.2**. The ΔH_c and ΔH_m were calculated considering the composition of the PF segment in each BCP sample. As shown in **Table 3.2**, ΔH_c and ΔH_m of the BCPs gradually increase as the branching number increases,

indicating higher crystallinity of the branched BCPs. Moreover, the smaller $FWHM_c$ of the branched BCPs can be attributed to smaller crystal size distribution.[32, 33] Based on the DSC studies, it can be inferred that the PF segments in the branched BCPs may undergo a more homogeneous crystallization process, leading to higher crystallinity and a more uniform PF crystalline phase.

3.3.3 Optical and Electrochemical Properties

The electronic properties of alkyne-PF (denoted as PF), PF-*b*-PDL, PF-*b*-PDL_2, and PF-*b*-PDL_3 were studied by UV-vis absorption and CV of the annealed polymer thin films. The as-cast polymer thin films possess one absorption band with the same peak at 385 nm (**Fig. 3.7a**). After thermal annealing **(Fig. 3.7b**), all of the BCPs exhibit a blue-shift of absorption to 376 nm, whereas the absorption band of the PF homopolymer remains unchanged. This finding is in agreement with a previous report on poly(9,9-di-*n*-hexyl-2,7-fluorene),[34] in which a blue-shift of the UV absorption peak was observed in conjunction with the growth of α crystallites in the melt-quenched polyfluorene sample. To compare the energy levels of the PF homopolymer and the BCPs, the optical band gap (E_g) was calculated from the onset absorption of the annealed films (**Fig. 3.7b**), and CV measurements (**Fig. 3.8**) were conducted to determine the exact HOMO level. The LUMO level was then calculated from the equation LUMO = HOMO + E_g. The HOMO/LUMO values of PF, PF-*b*-PDL, PF-*b*-PDL_2, and PF-*b*-PDL_3 are -5.63/-2.73, -5.63/-2.73, -5.61/-2.71, and -5.61/-2.71 eV, respectively (summarized in **Table 3.2**).

This demonstrates that incorporation of the soft PDL segments does not affect the energy levels of the semiconducting polymer, as expected.

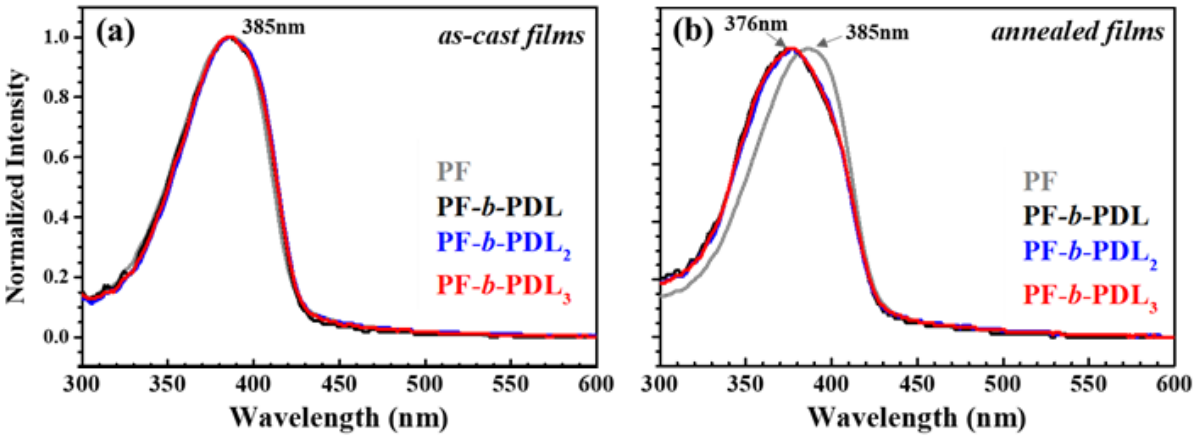

Fig. 3.7 UV-vis absorption spectra of the (a) as-cast and (b) annealed polymer films.

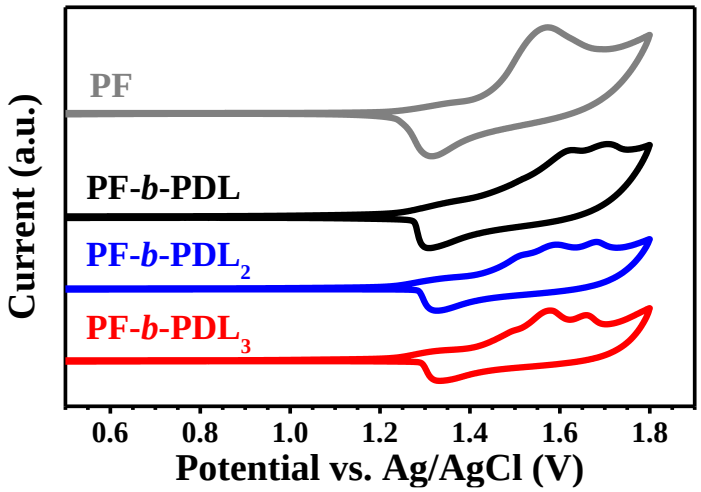

Fig. 3 8 CV characteristics of the annealed polymer films (annealing: 100 °C, 1 h).

3.3.4 Thin-film Morphology and Analysis of Crystalline Polyfluorene Domain

AFM images. The branched PDL soft segments are expected to modulate the phase separation of BCP and facilitate crystallization of the PF segment. Thin film morphology of the annealed polymer films (30 nm thick) was investigated by AFM and GI-WAXS experiments. To extract the features of the PF nanofibers from the AFM phase images of the BCPs, the nanofibers were identified using GTFiber software.[29] This is the first time that this method has been applied to a conjugated BCP system. In the phase images of the PF homopolymer (**Fig. 3.9b**), no distinct phase-separated structure was observed, owing to the continuous PF domain within the polymer film. Conversely, the phase image of the PF-*b*-PDL film (**Fig. 3.10d**) exhibits distinguishable soft (dark) and hard (bright) domains, in which the bright stripes are the nanofibrous structures formed by the assembly of PF. Moreover, the phase images of the branched polymers, PF-*b*-PDL_2 (**Fig. 3.10e**) and PF-*b*-PDL_3 (**Fig. 3.10f**), exhibit higher contrast and longer nanofibrous structures. The longer PF nanofibers in the branched BCP samples are likely due to the confined crystallization and homogeneous nucleation of the PF segment, as explained by the lower $T_{c,\,PF}$ and smaller $FWHM_c$ in the DSC studies. AFM height images of the alkyne-PF and the BCPs are provided in **Fig. 3.9a** and **Fig. 3.10a-c**, respectively. Root-mean-square surface roughness (R_q) of alkyne-PF, PF-*b*-PDL, PF-*b*-PDL_2, and PF-*b*-PDL_3 calculated from the height images is 0.76, 3.85, 4.16, and 3.75 nm, respectively.

The slightly higher R_q of the BCP films arises from the phase separation of the BCPs.

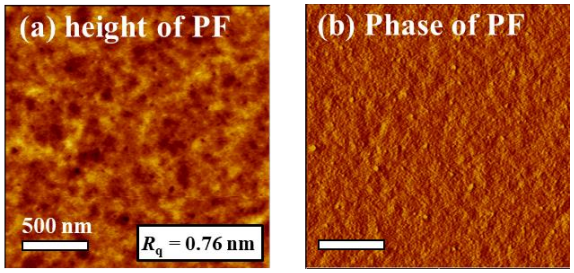

Fig. 3.9 AFM (a) height and (b) phase images of alkyne-PF (PF). Insets show the scale bars and surface roughness (R_q).

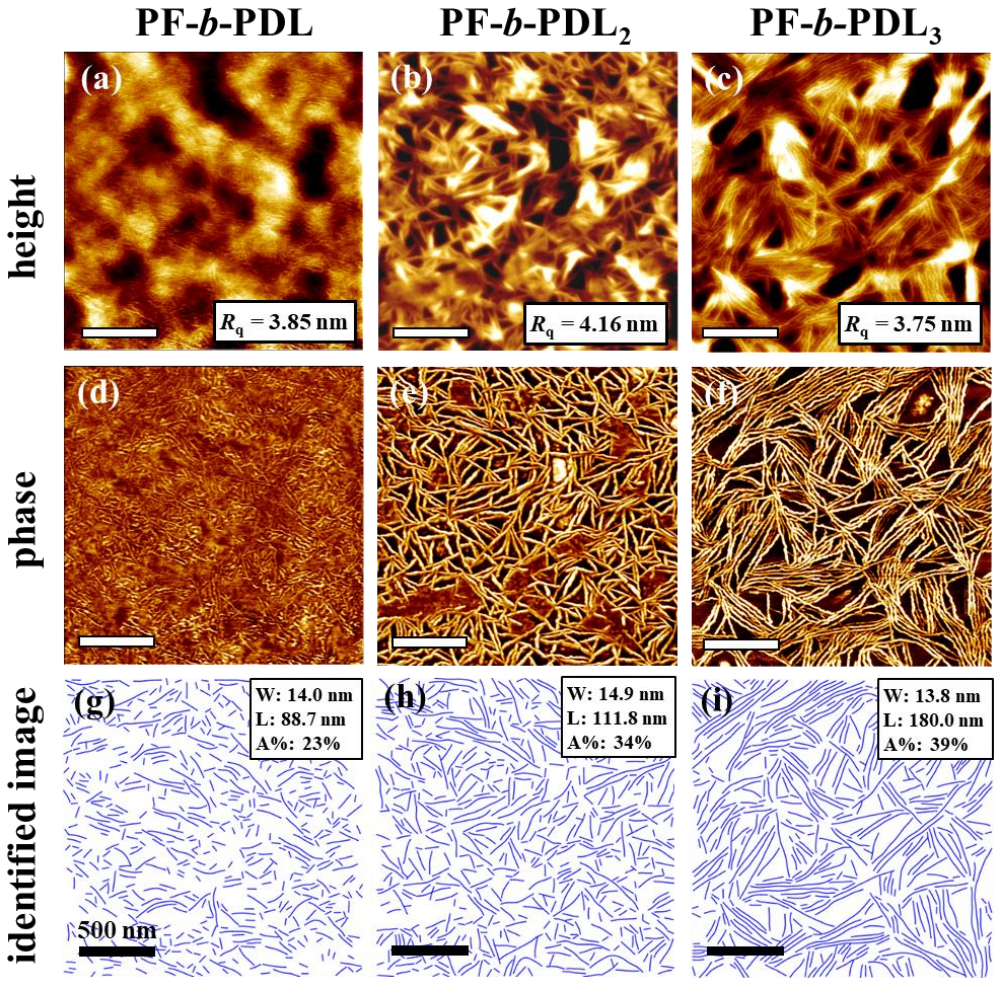

Fig. 3.10 AFM (a-c) height and (d-f) phase images, and the identified fiber images (g-i) of (a, d, g) PF-*b*-PDL, (b, e, h) PF-*b*-PDL$_2$ and (c, f, i) PF-*b*-PDL$_3$. Insets show scale bars, surface roughness (R_q), fiber width (W), length (L) and coverage area (A%).

Quantitative analysis of the PF nanofibers. AFM measurements frequently yield images with low contrast and moderate noise, thus making it difficult to extract features of the nanofibers from images.[29] Therefore, the identified fiber images, in which the nanofibers were identified from AFM images and thinned to single-pixel width, are more suitable choices for quantitative analysis. **Fig. 3.10g-i** show the identified fiber images of the BCPs and the features of the PF nanofibers (width (W), length (L), and coverage area (A%)) derived from the AFM phase images (**Fig. 3.10d-f**). The parameters used for identification of the fibers are provided in **Fig. 3.11** to aid readers in obtaining the same fiber images from our AFM phase images. As shown in **Fig. 3.10g-i**, all of the BCP samples exhibit PF nanofibers with similar fiber widths (W = 13.8-14.9 nm). However, the length of the nanofibers varies with the polymer architecture. The average length of the nanofibers in the PF-*b*-PDL, PF-*b*-PDL_2, and PF-*b*-PDL_3 films is 88.7 nm, 111.8 nm, and 180.0 nm, respectively, revealing that the branched PDL segments in the BCPs benefit the formation of long-range crystalline structures of PF. Aside from the width and length of the PF nanofibers, it is of great importance to compare the coverage area (A%) of PF nanofibers on the polymer thin films. Since the confined PF crystalline domains in the insulating polymer (PDL) matrix can be regarded as effective hole-trapping sites, the A% value can be correlated with the hole trapping density of the polymer electret. The A% value is calculated from the identified single-pixel width fiber images (**Fig. 3.10g-i**) considering the average width (W) of the nanofibers. The A% values of PF-*b*-PDL, PF-*b*-PDL_2, and PF-*b*-

PDL_3 are 23%, 34%, and 39%, respectively. The larger A% value of the branched BCPs (PF-*b*-PDL_2 and PF-*b*-PDL_3) can be attributed to two main reasons: 1) stronger phase separation behavior and higher crystallinity (supported by DSC data) of the branched BCPs, leading to more distinct and confined PF domains; and 2) higher relative density and smaller volume of the branched PDL segments, as evidenced by the SEC traces, which result in a higher volume ratio of PF in the branched BCPs. Quantitative analysis of the PF nanofibrous structure indicates that the branched BCPs as a charge-storage layer may provide more charge trapping sites for memory devices.

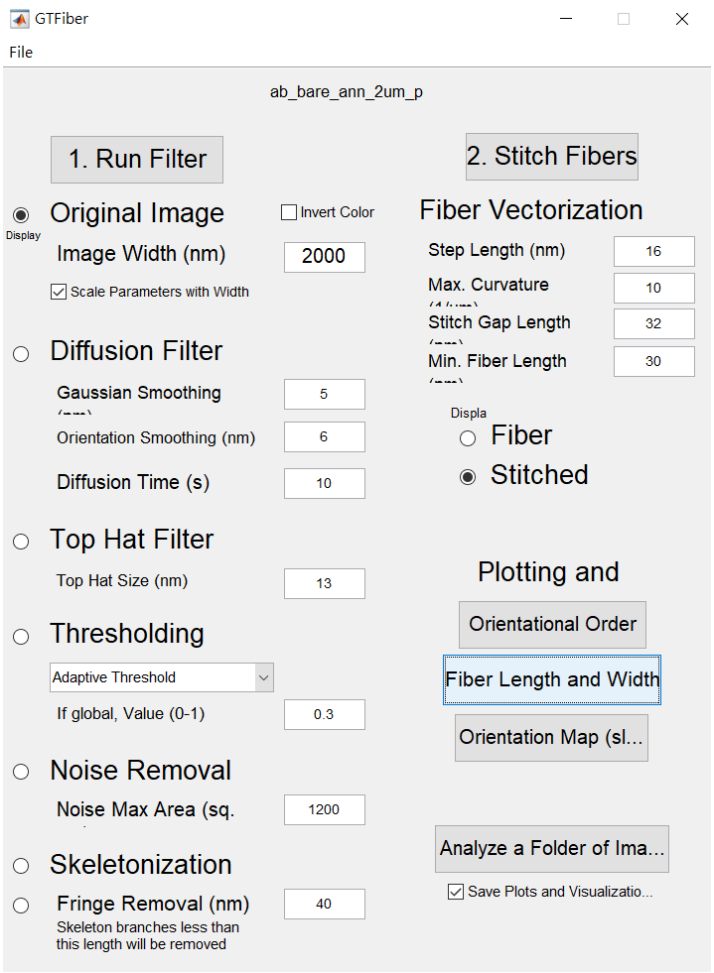

Fig. 3.11 Parameters used in this study for the analysis of the AFM phase images.

GI-WAXS measurements. GI-WAXS scattering images were collected to better understand the molecular packing within the polymer thin films. As shown in **Fig. 3.12a**, no distinguishable scattering patterns were present in the GI-WAXS two-dimensional (2D) image of alkyne-PF as a result of poor crystallinity of the PF homopolymer. Interestingly, the GI-WAXS 2D images of PF-*b*-PDL, PF-*b*-PDL_2, and PF-*b*-PDL_3 (**Fig. 3.12b-d**) exhibit multiple scattering spots with almost the same q values. Furthermore, the BCP samples each exhibit a scattering spot with the highest intensity in the out-of-plane (q_z) direction (q = 0.564 $Å^{-1}$, d = 11.1 Å). According to the X-ray diffraction data of poly(9,9-di-*n*-hexyl-2,7-fluorene),[30] this scattering spot represents the characteristic lamellar reflection (200) of the α crystallites. Therefore, it can be concluded that the PF block of the BCPs form α phase crystallites, with stacking of the lamellar structure perpendicular to the surface of the silicon wafer substrate. Moreover, the scattering patterns clearly indicate an orthogonal unit cell (a = 2.23 nm, b = 2.37 nm, c = 3.23 nm), in which a is along the q_z direction, and b and c are along the q_{xy} direction. This type of GI-WAXS pattern has been reported for the melt-crystallized α phase nanofibril films of monodisperse poly(9,9-di-*n*-octyl-2,7-fluorene) (PFO),[35] but has never been reported for any studies involving poly(9,9-di-*n*-hexyl-2,7-fluorene)-based polymers. I speculate that the incorporated soft PDL segments in the BCPs facilitate the assembly of the PF block through phase separation, thus leading to highly oriented α crystallites of PF within the PF nanofibers.

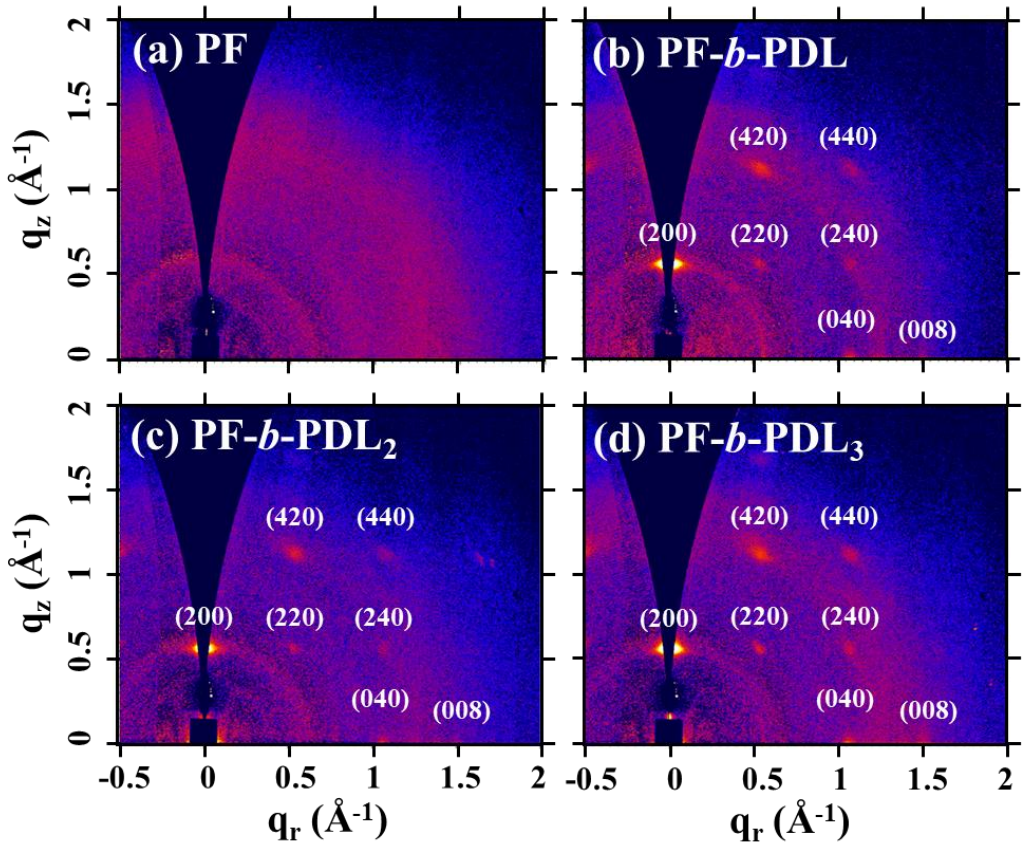

Fig. 3.12 GI-WAXS 2D images of (a) alkyne-PF (PF), (b) PF-*b*-PDL, (c) PF-*b*-PDL_2, and (d) PF-*b*-PDL_3.

3.3.5 Charge Trapping Properties of the Polymer Electrets

OFET memories with different polymer electrets (Si/SiO_2 (300 nm)/PF or PF-*b*-PDL_x/PTCDI-C8/Au) were fabricated and the device performance was investigated, as summarized in **Table 3.3** along with the coverage area (A%) of PF nanofibers in the electret films. The cross-sectional SEM image of the PF-*b*-PDL_3 device is provided in **Fig. 3.13**. Note that PTCDI-C8 was chosen as n-type semiconducting layer for the fabrication of OFET device. Due to the built-in electric field formed by the holes trapped in the PF-based polymer electret, electrons can be more easily accumulated at the semiconductor/electret interface, facilitating the transportation of electrons in the PTCDI-C8 layer. Therefore, the drain current-gate voltage (I_{ds}-V_g) curve shows a negative shift and the device could retain at high conductive state even when the gate bias is removed. Also, the HOMO and LUMO energy levels of PTCDI-C8 are -6.3 eV and -4.3 eV, respectively.[36] The holes injected to the polymer electret layer could be stabilized owing to the sufficiently low HOMO level of PTCDI-C8 compared with the prepared PF-based BCPs (-5.63 to -5.61 eV).

Table 3.3 Coverage area of polyfluorene nanofibers (A%) and OFET memory performance of the studied polymer electrets.

sample	A [a] (%)	μ_{ave} ($cm^2V^{-1}S^{-1}$)	I_{on}/I_{off} (-)	V_{th} (V) *initial*	*writing*	*erasing*	ΔV_{th} (V)	I_{write}/I_{erase} (-)	Δn (cm^{-2})
PF	-	7.1×10^{-2}	2.3×10^{5}	32	*-43	*35	*78	*1.9×10^{5}	*5.6×10^{12}
PF-*b*-PDL	23	1.3×10^{-2}	9.5×10^{3}	24	-32	31	63	4.1×10^{3}	4.5×10^{12}
PF-*b*-PDL_2	34	1.1×10^{-2}	2.9×10^{4}	23	-56	30	86	2.4×10^{4}	6.2×10^{12}
PF-*b*-PDL_3	39	1.0×10^{-2}	1.0×10^{5}	23	-70	32	102	3.5×10^{4}	7.3×10^{12}

[a] Determined from the identified fiber images of the BCPs (**Fig. 3.10 g-i**). *The PF homopolymer device exhibits transient memory behavior with poor on-current retention, as shown in **Fig. 3.17b**.

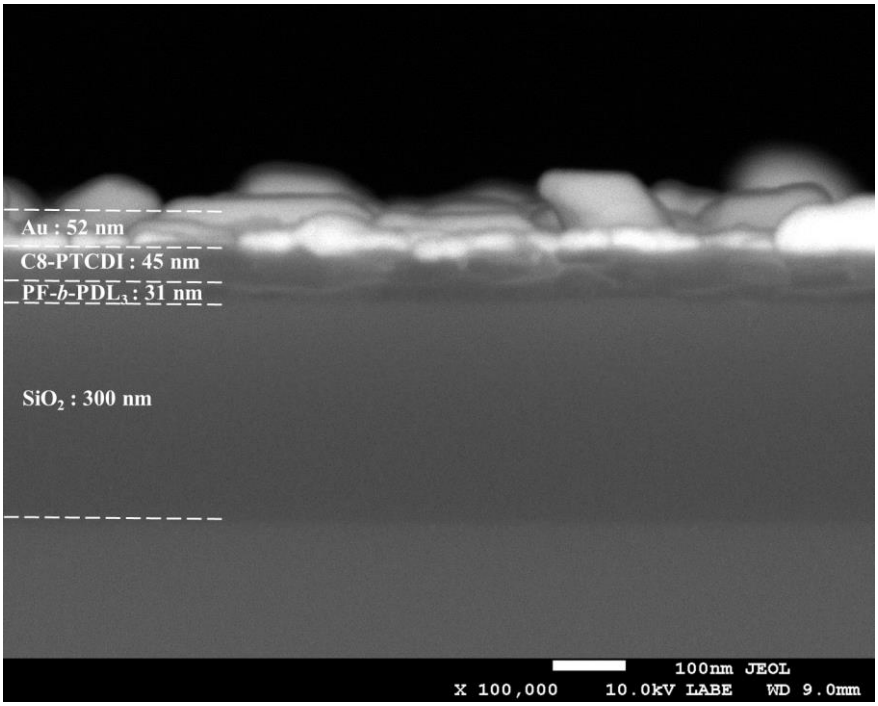

Fig. 3.13 Cross-sectional SEM image of the PF-*b*-PDL_3 based OFET memory.

All of the devices were measured in the dark to avoid light-induced charge transfer or excitons in the charge-storage and semiconducting layers. Judging from the initial I_{ds}-V_g curves (**Fig. 3.14a**), the average charge mobility of the OFET memories (μ_{ave}) with electrets of PF, PF-*b*-PDL, PF-*b*-PDL$_2$, and PF-*b*-PDL$_3$ is 7.1 × 10^{-2}, 1.3 × 10^{-2}, 1.1 × 10^{-2}, and 1.0 × 10^{-2} $cm^2V^{-1}S^{-1}$, respectively, and the on/off current ratio (I_{on}/I_{off}) of the devices ranges from 9.5 × 10^3 to 2.3 × 10^5, respectively. The PF homopolymer device exhibits comparable mobility with the PTCDI-C8 OFET (Si/SiO_2/PTCDI-C8/Au) (**Fig. 3.14b**). Due to more hydrophilic surface (contact angle measurements, **Fig. 3.15**), and higher surface roughness of the BCP electrets, the subsequently deposited PTCDI-C8 layer exhibit smaller grain size and higher surface roughness as investigated by AFM (**Fig. 3.16**). Therefore, the devices of BCP electrets possess slightly lower charge mobility of the BCP devices compared with the PF-based device.

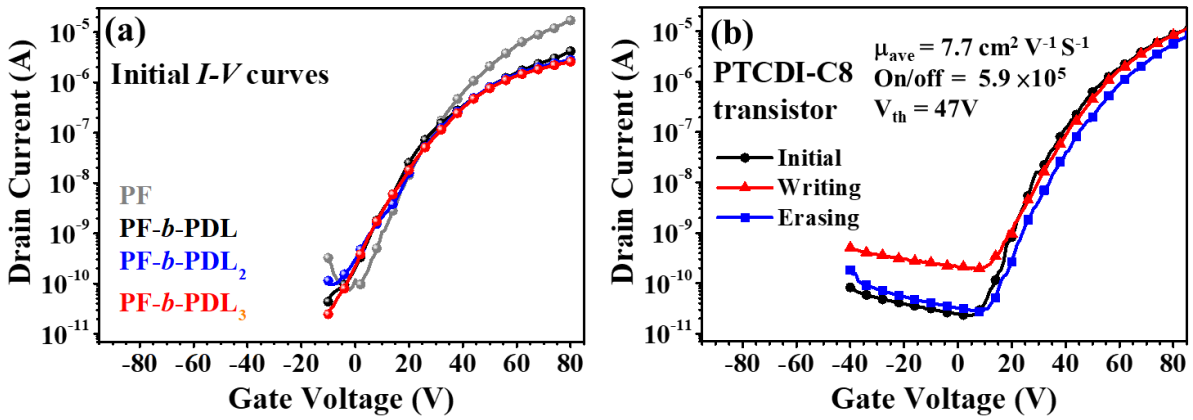

Fig. 3.14 (a) Initial I_{ds}-V_g curves of the OFET memory with different charge-storage layers. (b) Initial, writing and erasing curves of the PTCDI-C8 transistor with the device structure of Si/SiO_2/PTCDI-C8/Au.

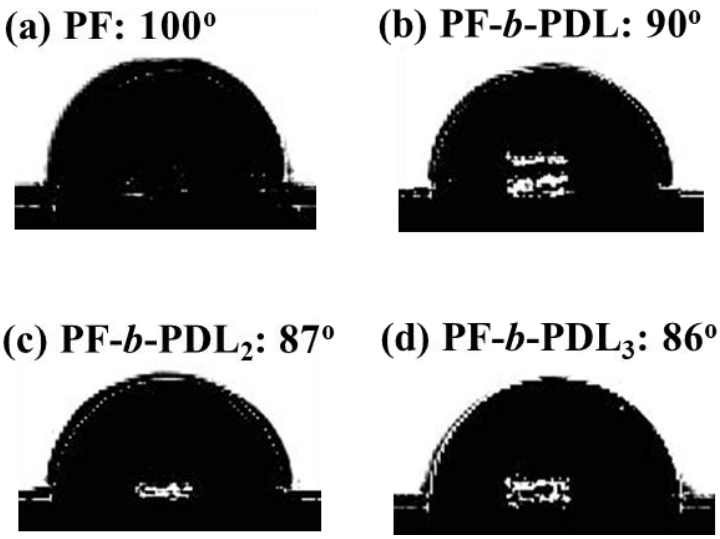

Fig. 3.15 Contact angle measurements of the studied polymers.

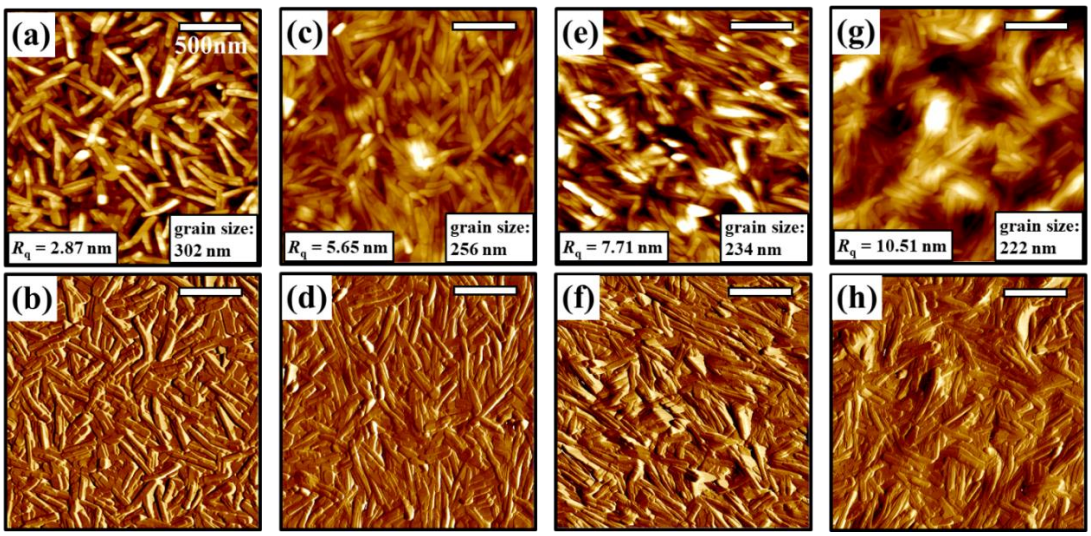

Fig. 3.16 AFM height (a, c, e, g) and phase (b, d, f, h) images of C8-PTCDI deposited on top of (a, b) PF, (c, d) PF-*b*-PDL, (e, f) PF-*b*-PDL$_2$ and (g, h) PF-*b*-PDL$_3$ electrets. The insets show the scale bar, surface roughness (R_q) and averaged grain size.

After applying a gate voltage (V_g) of -140 V for 8 s as the "writing" process (**Fig. 3.17a**), the PF and BCP devices turn to the ON state and the transfer curves shift in the negative direction, leading to much higher drain current at $V_g = 0$. This is due to the positive charges accumulated in the electret layer through negative gate bias. The "erasing" process was

performed by applying a V_g of 140 V for 2 s, resulting in a backward shift of the transfer curves to the OFF state along with a slightly more positive threshold voltage (V_{th}) than the initial state. The slightly lower V_{th} of the initial curve than the erasing curve of each OFET memory is due to the small number of holes trapped in the film before OFET operation. The memory window (ΔV_{th}) of the PF, PF-*b*-PDL, PF-*b*-PDL$_2$, and PF-*b*-PDL$_3$ devices is 78, 63, 86, and 102 V, respectively, and the memory ratio (I_{write}/I_{erase}) at $V_g = 0$ is 1.9×10^5, 4.1×10^3, 2.4×10^4, and 3.5×10^4, respectively, indicating that the memory behavior of the devices can be modulated through the choice of polymer electret. The drain current retention of the device at the ON and OFF states was recorded at $V_g = 0$ and $V_d = 80$ V (**Fig. 3.17b**). Although the PF homopolymer device exhibits a large memory window of 78 V, the drain current of the ON state drops to a similar level as that of the OFF state (10^{-11} A) after 4000 s due to the continuous PF domain in the electret that forces charges to rapidly dissipate.[17] On the contrary, the drain current of the BCP devices in the ON state decreases more slowly, reaching a steady value after 10000 s, which is at least two orders of magnitude higher than the OFF state. This demonstrates that it is beneficial to employ a conjugated/insulating BCP as the electret for non-volatile OFET memory. Moreover, the drain current of the PF-*b*-PDL, PF-*b*-PDL$_2$, and PF-*b*-PDL$_3$ devices in the ON state after 10000 s is 1.1×10^{-9}, 8.3×10^{-8}, and 4.5×10^{-7} A, respectively, revealing superior memory performance of the branched BCP devices compared to the linear BCP device.

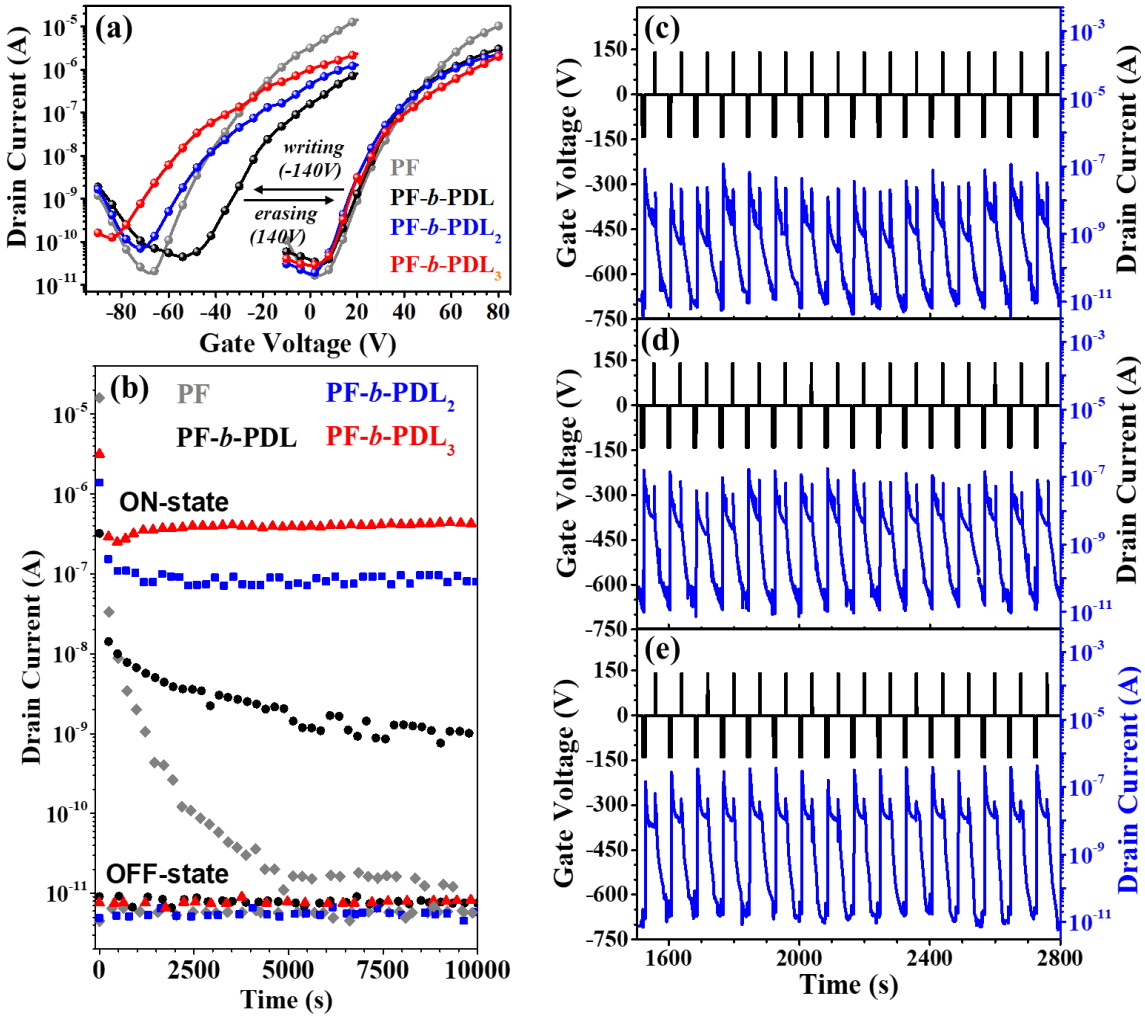

Fig. 3.17 (a) Writing/erasing plots and (b) corresponding memory retention characteristics (V_g = 0V) of the OFET devices at V_d = 80 V. WRER cycles of the (c) PF-*b*-PDL, (d) PF-*b*-PDL$_2$ and (e) PF-*b*-PDL$_3$ device at V_d = 80 V.

Trapping density (Δn) of the memory devices was then calculated from the equation $\Delta n = (\Delta V_{th}/e) \times C$, where ΔV_{th} is the memory window, e is the charge of a hole, and C is the capacitance. As shown in **Table 3.3**, Δn can be effectively improved from 4.5×10^{12} (PF-*b*-PDL) to 7.3×10^{12} (PF-*b*-PDL$_3$) by increasing the branching number of the PDL segments, which can be comprehensively explained by the higher A% value of the branched BCP thin

films. The rewritability of the OFET memories of BCP was than examined with write-read-erase-read (WRER) cycles at V_g = 140 V (8 s), 0 V (30 s), -140 V (2 s), and 0 V (40 s). As can be seen in **Fig. 3.17e**, the PF-*b*-PDL_3 device can be repeatedly written and erased with an ON/OFF current ratio > 10^3. The PF-*b*-PDL (**Fig. 3.17c**) and PF-*b*-PDL_2 (**Fig. 3.17d**) devices also retain their performance after WRER cycles, but they exhibit slightly lower ON/OFF ratios due to the presence of fewer charge-trapping sites within the charge-storage layer.

Energy levels of the insulating PDL matrix (represented by N_3-PDL) were calculated from UV (**Fig. 3.18a**) and CV (**Fig. 3.18b**) measurements to better understand the mechanism of memory effect. PDL shows wide optical band gap at 4.77eV, and the calculated HOMO and LUMO levels of PDL is -6.5 and -1.7 eV, respectively, indicating insulating property of PDL. **Figure 3.19** explains different memory performance of PF and PF-based electrets (**Fig. 3.19a** and **Fig. 3.19b**), and the proposed mechanism of BCP-based memory devices (**Fig. 3.19c** and **Fig. 3.19d**). In the OFET memory made by PF electret (**Fig. 3.19a**), the positive charges accumulated in electret layer will dissipate to the electret/semiconductor interface rapidly through continuous PF domain, and those charges are neutralized with the electron flow in semiconductor during operation of transistor. Therefore, PF-based device has poor on-current retention. On the other hand, the positive charges can be stabilized in the isolated PF domains created in the PDL matrix due to insulating property of PDL and energy barrier created by low-lying HOMO level of PDL. Therefore, the BCP devices have much better on-current retention.

Considering the energy band diagrams of PDL matrix, PF and semiconducting layer of PTCDI-C8, I propose operating mechanism of the OFET memories with PF-*b*-PDLs as electrets, as illustrated in **Fig. 3.19c** and **Fig. 3.19d**. During the writing process (**Fig. 3.19c**), a large number of holes were induced in the HOMO level (-6.3 eV) of PTCDI-C8, and those holes were tunneled and stabilized into the isolated PF domain. Due to the sufficiently high HOMO level of PF (-5.7 eV) and the energy barrier from the low-lying HOMO level of PDL (-6.5 eV), the injected holes can be retained in the PF domain even after removing the gate bias, leading to a non-volatile memory-performing device. During the erasing process (**Fig. 3.19d**), the holes in the PF domain were tunneled back to the PTCDI-C8 layer due to the repulsive force created from the positive gate bias, thus the device can be turned back to the OFF state. Collectively, the energy level adaptation between PTCDI-C8 and the BCPs conduces to a respectable, reproducible and rewritable device performance.

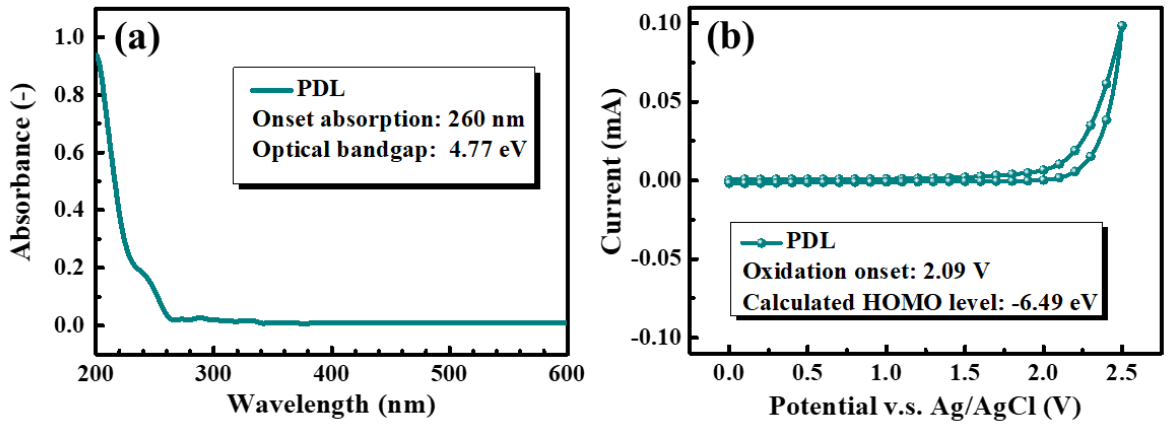

Fig. 3.18 (a) UV and (b) CV measurements of N_3-PDL (PDL).

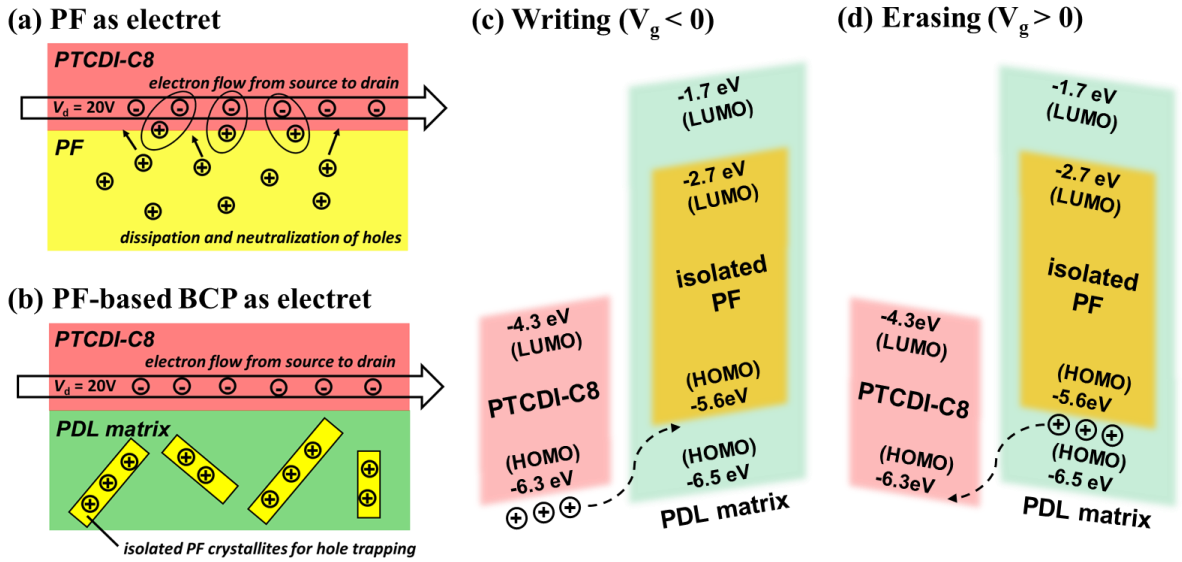

Fig. 3.19 Comparison of memory performance of (a) PF ant (b) PF-based BCP electrets. Proposed mechanism and energy band diagrams under the (c) negative and (d) positive gate voltage bias for the OFET memory using the BCP electrets.

3.3.6 Stretchable OFET Memory Applications

Finally, I examined the stretchability of the polymer thin films from OM images and then fabricated the OFET memories with the stretched and transferred polymer electret films. As shown in **Fig. 3.20**, the PF homopolymer thin film cannot endure the applied strain, exhibiting obvious cracks perpendicular to the strain direction at 25% strain, which grow even larger at higher stretching loadings. On the other hand, all of the BCP thin films exhibit favorable stretchability due to incorporation of the soft PDL segments, which do not crack at up to 100% strain. This suggests that the studied BCPs are suitable for use in stretchable electronic devices.

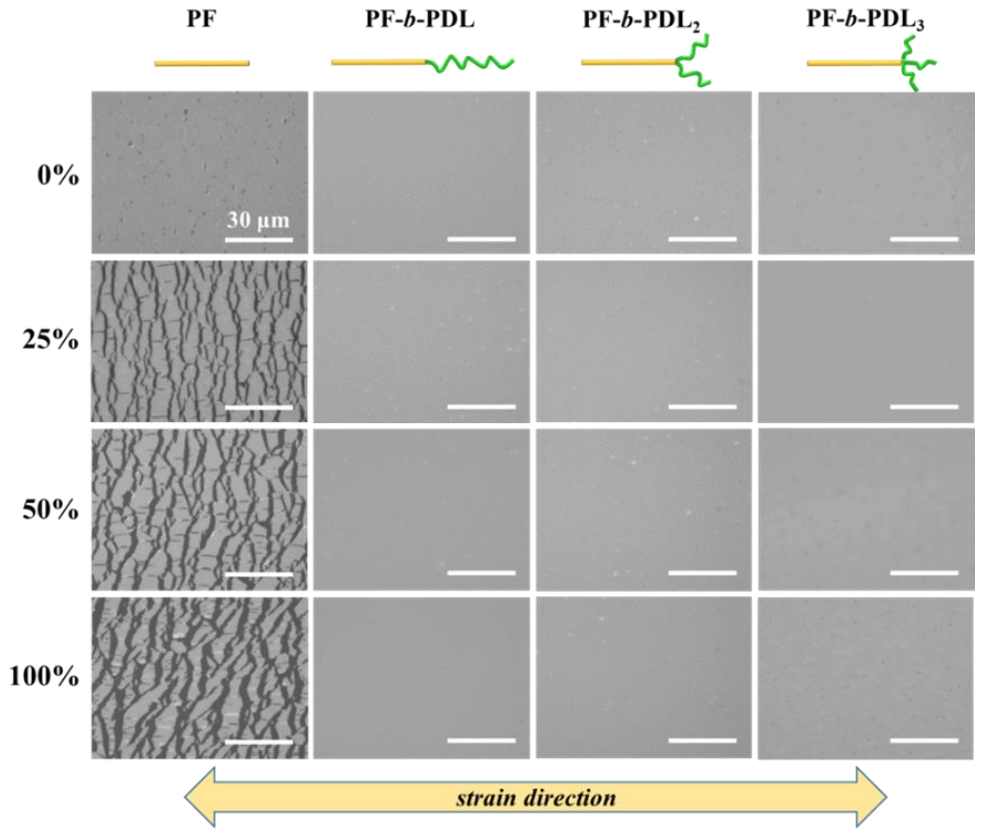

Fig. 3.20 OM images of the stretched polymer thin films. The annealed polymer films were transferred from an ODTS wafer to a PDMS substrate, stretched at different loadings, and transferred back to a second bare silicon wafer for the measurements.

The structure of the OFET memories of the "stretched and transferred BCP electrets" is illustrated in **Fig. 3.21a**. After transferring the electret layer on 300nm silicon wafer, C8-PTCDI as semiconducting layer was subsequently deposited on top of electret layer, and then source and drain electrodes (gold) were thermally evaporated through shadow masks on top of C8-PTCDI layer to finish device fabrication. Note that in this application, only the electret layer (PF-based polymers) was stretched, while the rest of the device components were not stretched. To realize a fully stretchable device in the future, stretchable electrode such as poly(3,4-ethylenedioxythiophene) polystyrene sulfonate (PEDOT:PSS) and carbon nanotubes, stretchable dielectric such as polydimethylsiloxane, and stretchable semiconductor such as P3HT-b-PDLs, as developed in chapter 2, should be adopted in device fabrication, which is beyond the scope of this dissertation. The performance of the BCP electrets under different strain loadings was compared by analyzing the I_{ds}-V_g curves of the ON and OFF states of the devices. PF-based device (**Fig. 3.21b**) shows deteriorated performance from 50% of strain, which is result from the micrometer-scale cracks formed on the electret layer that affect the smoothness and uniformity of the subsequently deposited PTCDI-C8 layer. Unlike the PF-based device, the BCP devices (**Fig. 3.21c-e**) can be written and erased at up to 100% strain without a significant change in V_{th} in the ON and OFF states. As shown in **Fig. 3.21f** (dashed lines), the mobility retention of all the BCP devices is > 50% after applying 100% strain. Note that the on-current and mobility of the devices with 0% strain and transferred electret film in

this section (**Fig. 3.21**) is lower than those of the devices with the electret layer directly deposited on top of silicon wafer (**Fig. 3.17**). It is due to the defects formed at the SiO_2 dielectric/polymer interface during the film transferring process.[28] The memory window of the BCP devices (**Fig. 3.21f,** solid lines) drops slightly before reaching 50% strain, and then becomes steady at higher stretching loadings. These results indicate that the prepared conjugated/insulating BCPs perform well as stretchable hole-trapping materials. Furthermore, the PF-*b*-PDL_3 device exhibits a memory window of 90 V (91% retention) at 100% strain, demonstrating extraordinary memory performance of the stretchable device. Finally, I_{ds}-V_g curves of the PF-*b*-PDL_3 device after 0-500 stretch-release cycles at 50% strain were recorded (**Fig. 3.22a**) and the device performance was evaluated (**Fig. 3.22b**). As shown in **Fig. 3.22b**, charge mobility of the PF-*b*-PDL_3 device drops within one order of magnitude (34% mobility retention), and the memory window of the device changes from 99 V to 83 V (84% memory window retention) after 500 cycles, demonstrating excellent durability of the device under strain. Device performances of the OFET memories in all the stretching conditions including mobility (μ), memory window (ΔV_{th}) and memory ratio (I_{write}/I_{erase}) are summarized in **Table 3.4**.

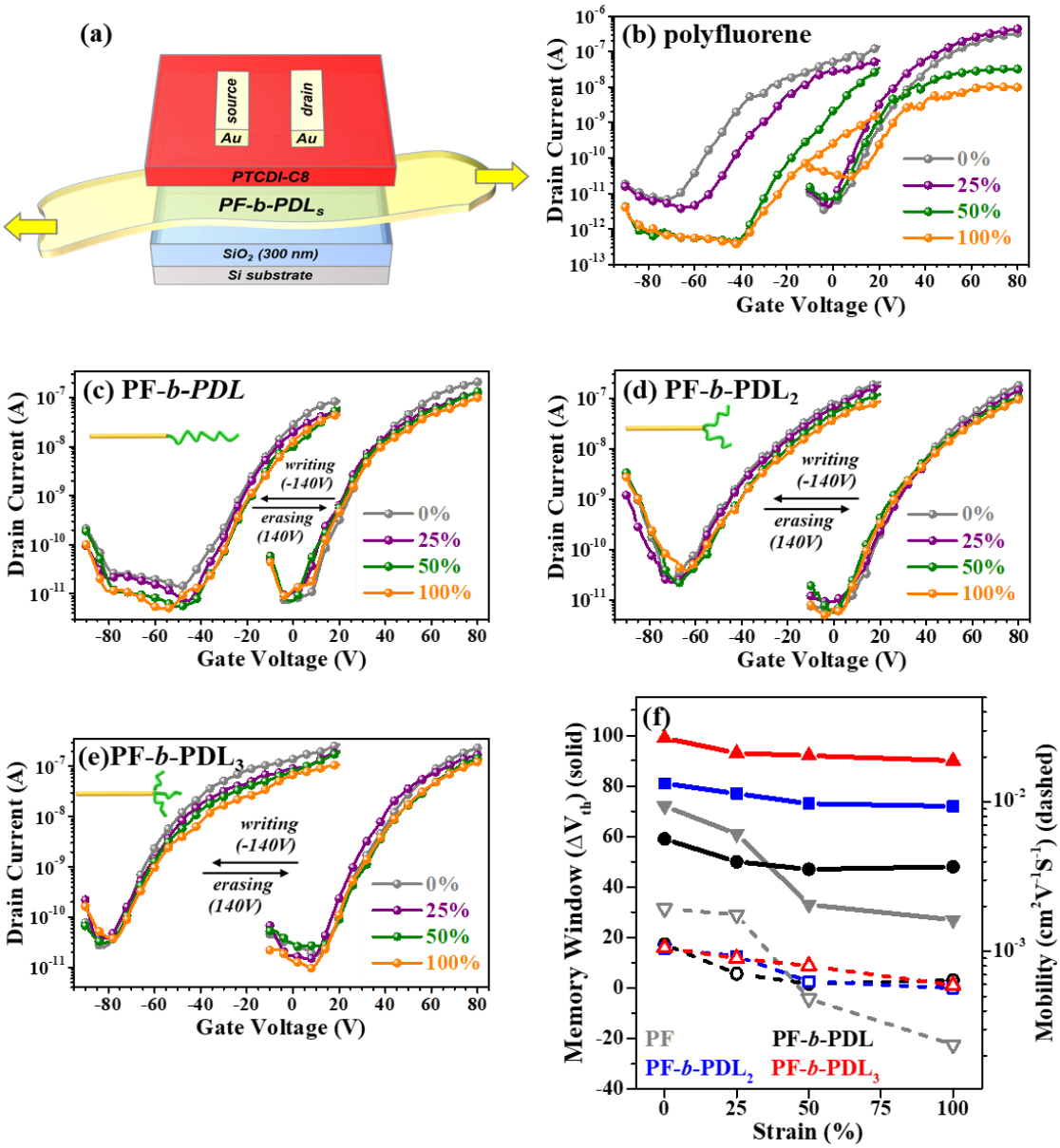

Fig. 3.21 (a) Structure of the stretchable OFET memories. Writing/erasing plots of the OFET memories made from the stretched (b) PF, (c) PF-*b*-PDL, (d) PF-*b*-PDL$_2$, and (e) PF-*b*-PDL$_3$ films at V_d = 80 V. (f) Memory window (solid lines) and charge mobility (dashed lines) of the stretchable memory device.

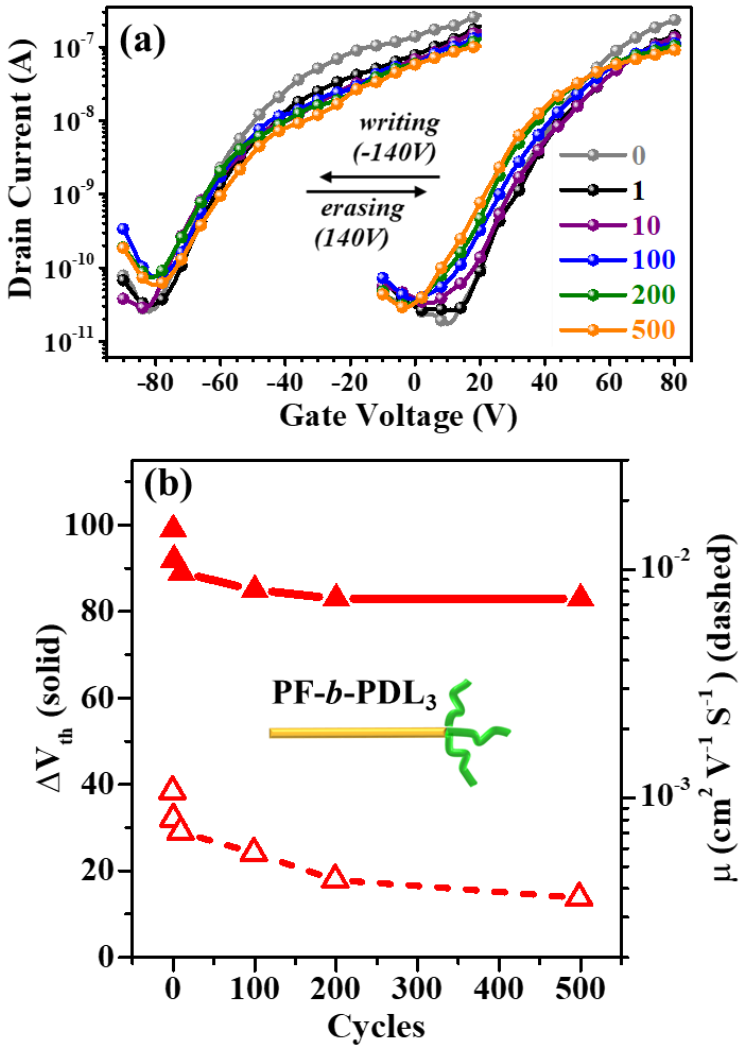

Fig. 3.22 (a) Writing and erasing plots of the PF-*b*-PDL$_3$ device after 0-500 stretch/release cycles at 50% strain (V_d = 80 V). (b) Memory window (ΔV_{th}) (solid lines) and charge mobility (μ) (dashed lines) of the PF-b-PDL$_3$ device after stretch-release cycles at 50% strain. (V_d = 80 V).

Table 3.4 Device performance of the stretchable devices. All the values were calculated from **Fig. 3.21b-e** and **Fig. 3.22a**. All of the device performance was averaged by at least 5 devices in 2 different batches.

sample	stretching conditions	μ_{ave} ($cm^2V^{-1}S^{-1}$)	V_{th} (V)		ΔV_{th} (V)	I_{write}/I_{erase} (-)
			writing	*erasing*		
PF	0%	1.94×10^{-3}	-46	26	72	8.9×10^{3}
	25%	1.76×10^{-3}	-37	24	61	4.1×10^{3}
	50%	4.83×10^{-4}	-20	13	33	2.9×10^{2}
	100%	2.38×10^{-3}	-13	14	27	7.2
PF-*b*-PDL	0%	1.13×10^{-3}	-28	31	59	3.8×10^{3}
	25%	7.08×10^{-4}	-22	28	50	1.8×10^{3}
	50%	6.08×10^{-4}	-20	27	47	1.4×10^{3}
	100%	6.42×10^{-4}	-19	29	48	1.1×10^{3}
PF-*b*-PDL_2	0%	1.05×10^{-3}	-50	31	81	1.2×10^{4}
	25%	9.30×10^{-4}	-49	28	77	6.2×10^{3}
	50%	6.30×10^{-4}	-46	27	73	9.1×10^{3}
	100%	5.68×10^{-4}	-45	27	72	5.6×10^{3}
PF-*b*-PDL_3	0%	1.06×10^{-3}	-65	34	99	4.7×10^{3}
	25%	9.01×10^{-4}	-61	32	93	5.3×10^{3}
	50%	8.00×10^{-4}	-59	33	92	2.7×10^{3}
	100%	5.93×10^{-4}	-57	33	90	5.0×10^{3}
PF-*b*-PDL_3	50% 10 cycles	7.02×10^{-4}	-57	32	89	1.8×10^{3}
	50% 100 cycles	5.67×10^{-4}	-55	30	85	1.6×10^{3}
	50% 200 cycles	4.33×10^{-4}	-54	29	83	1.7×10^{3}
	50% 500 cycles	3.61×10^{-4}	-54	29	83	1.7×10^{3}

3.4 Summary

I synthesized poly(9,9-di-*n*-hexyl-2,7-fluorene)-*block*-poly(*δ*-decanolactone) (PF-*b*-PDL) with AB, AB_2, and AB_3 architectures for OFET memory applications. Judging from the DSC data, the PF block of the branched BCPs underwent a more homogeneous crystallization process than the linear BCP, leading to higher PF crystallinity and a more uniform PF crystalline phase. In thin film state, the annealed BCP films formed nanofibrous structures of PF with highly oriented *α* crystallites on silicon wafer owing to the incorporated PDL segments. Moreover, the average fiber width, length, and coverage area of the PF nanofibers on the thin films were quantitatively analyzed using AFM phase images. The results indicate that the BCPs with branched PDL segments form longer PF nanofibers with a larger coverage area, which is desirable for memory device applications. Consequently, the OFET memory with the charge-storage layer of PF-*b*-PDL_3 exhibited the largest memory window (102 V), highest memory ratio (3.5×10^4), and highest hole-trapping density (7.3×10^{12} cm^{-2}). Stretchable OFET devices were fabricated, with all of the BCP devices retaining their performance at up to 100% strain. In particular, exposing PF-*b*-PDL_3 to 500 stretch-release cycles at 50% strain resulted in 34% mobility retention and 84% memory window retention. This study provides a new strategy to create high-performance and stretchable hole-trapping materials through the design of conjugated/insulating block copolymer architectures, thus demonstrating a new protocol that correlates the morphology of BCP films with memory device performance.

3.5 Reference

1. D. Son, J. H. Koo, J.-K. Song, J. Kim, M. Lee, H. J. Shim, M. Park, M. Lee, J. H. Kim and D.-H. Kim, *ACS nano*, 2015, **9**, 5585-5593.
2. Y.-C. Lai, Y.-C. Huang, T.-Y. Lin, Y.-X. Wang, C.-Y. Chang, Y. Li, T.-Y. Lin, B.-W. Ye, Y.-P. Hsieh and W.-F. Su, *NPG Asia Mater.*, 2014, **6**, e87-e87.
3. C. a. Di, F. Zhang and D. Zhu, *Adv. Mater.*, 2013, **25**, 313-330.
4. Y. Ni, Y. Wang and W. Xu, *Small*, 2020, 1905332.
5. A.-N. Au-Duong, C.-C. Kuo and Y.-C. Chiu, *Polym. J.*, 2018, **50**, 649-658.
6. W. L. Leong, P. S. Lee, A. Lohani, Y. M. Lam, T. Chen, S. Zhang, A. Dodabalapur and S. G. Mhaisalkar, *Adv. Mater.*, 2008, **20**, 2325-2331.
7. M. Kang, K. J. Baeg, D. Khim, Y. Y. Noh and D. Y. Kim, *Adv. Funct. Mater.*, 2013, **23**, 3503-3512.
8. J. Hoffman, X. Pan, J. W. Reiner, F. J. Walker, J. Han, C. H. Ahn and T. Ma, *Adv. Mater.*, 2010, **22**, 2957-2961.
9. R. C. Naber, K. Asadi, P. W. Blom, D. M. de Leeuw and B. de Boer, *Adv. Mater.*, 2010, **22**, 933-945.
10. Y.-H. Chou, H.-C. Chang, C.-L. Liu and W.-C. Chen, *Polym. Chem.*, 2015, **6**, 341-352.
11. K. J. Baeg, Y. Y. Noh, J. Ghim, B. Lim and D. Y. Kim, *Adv. Funct. Mater.*, 2008, **18**, 3678-3685.
12. C.-C. Shih, W.-Y. Lee and W.-C. Chen, *Mater. Horiz.*, 2016, **3**, 294-308.
13. C. C. Shih, Y. C. Chiu, W. Y. Lee, J. Y. Chen and W. C. Chen, *Adv. Funct. Mater.*, 2015, **25**, 1511-1519.
14. C.-C. Shih, Y.-C. Chiang, H.-C. Hsieh, Y.-C. Lin and W.-C. Chen, *ACS Appl. Mater. Interfaces*, 2019, **11**, 42429-42437.
15. H. Ling, J. Lin, M. Yi, B. Liu, W. Li, Z. Lin, L. Xie, Y. Bao, F. Guo and W. Huang, *ACS Appl. Mater. Interfaces*, 2016, **8**, 18969-18977.
16. J.-C. Hsu, W.-Y. Lee, H.-C. Wu, K. Sugiyama, A. Hirao and W.-C. Chen, *J. Mater. Chem.*, 2012, **22**, 5820-5827.
17. Y.-C. Chiu, C.-C. Shih and W.-C. Chen, *J. Mater. Chem. C*, 2015, **3**, 551-558.
18. C. Müller, S. Goffri, D. W. Breiby, J. W. Andreasen, H. D. Chanzy, R. A. Janssen, M. M. Nielsen, C. P. Radano, H. Sirringhaus and P. Smith, *Adv. Funct. Mater.*, 2007, **17**, 2674-2679.
19. J.-T. Wang, S. Takshima, H.-C. Wu, C.-C. Shih, T. Isono, T. Kakuchi, T. Satoh and W.-C. Chen, *Macromolecules*, 2017, **50**, 1442-1452.
20. Y.-C. Chiang, S. Kobayashi, T. Isono, C.-C. Shih, T. Shingu, J.-J. Hung, H.-C. Hsieh, S.-H. Tung, T. Satoh and W.-C. Chen, *Polym. Chem.*, 2019, **10**, 5452-5464.
21. H.-C. Hsieh, C.-C. Hung, K. Watanabe, J.-Y. Chen, Y.-C. Chiu, T. Isono, Y.-C. Chiang,

R. R. Reghu, T. Satoh and W.-C. Chen, *Polym. Chem.*, 2018, **9**, 3820-3831.
22. M. T. Martello, A. Burns and M. Hillmyer, *ACS Macro Lett.,* 2012, **1**, 131-135.
23. T. Isono, B. J. Ree, K. Tajima, R. Borsali and T. Satoh, *Macromolecules*, 2018, **51**, 428-437.
24. T. Isono, S. Nakahira, H.-C. Hsieh, S. Katsuhara, H. Mamiya, T. Yamamoto, W.-C. Chen, R. Borsali, K. Tajima and T. Satoh, *Macromolecules*, 2020, **53**, 5408-5417.
25. K. Makiguchi, T. Satoh and T. Kakuchi, *Macromolecules*, 2011, **44**, 1999-2005.
26. S. Kobayashi, K. Fujiwara, D.-H. Jiang, T. Yamamoto, K. Tajima, Y. Yamamoto, T. Isono and T. Satoh, *Polym. Chem.*, 2020, **11**, 6832-6839.
27. D.-H. Jiang, S. Kobayashi, C.-C. Jao, Y. Mato, T. Isono, Y.-H. Fang, C.-C. Lin, T. Satoh, S.-H. Tung and C.-C. Kuo, *Polymers*, 2020, **12**, 84.
28. L.-C. Hsu, S. Kobayashi, T. Isono, Y.-C. Chiang, B. J. Ree, T. Satoh and W.-C. Chen, *Macromolecules*, 2020, **53**, 7496-7510.
29. N. E. Persson, M. A. McBride, M. A. Grover and E. Reichmanis, *Chem. Mater.*, 2017, **29**, 3-14.
30. S. Chen, A. Su, C. Su and S. Chen, *J. Phys. Chem. B.*, 2006, **110**, 4007-4013.
31. J.-T. Xu, J. P. A. Fairclough, S.-M. Mai, C. Chaibundit, M. Mingvanish, C. Booth and A. J. Ryan, *Polymer*, 2003, **44**, 6843-6850.
32. S. Tzavalas, D. E. Mouzakis, V. Drakonakis and V. G. Gregoriou, *J. Polym. Sci., Part B: Polym. Phys.*, 2008, **46**, 668-676.
33. C. Liu, K. W. Chan, J. Shen, C. Z. Liao, K. W. K. Yeung and S. C. Tjong, *Polymers*, 2016, **8**, 425.
34. W.-R. Wu, W.-T. Chuang, U.-S. Jeng, C.-J. Su, S.-H. Chen, C.-Y. Chen, C.-H. Su and A.-C. Su, *Polymer*, 2012, **53**, 3928-3936.
35. J. Liu, Q. Wang, C. Liu, H. Chang, H. Tian, Y. Geng and D. Yan, *Polymer*, 2015, **65**, 1-8.
36. C.-H. Kim and I. Kymissis, *J. Mater. Chem. C*, 2017, **5**, 4598-4613.

Chapter 4

Conclusion and Perspectives

4.1 Conclusion

In summary, two series of conjugated/insulating BCPs, poly(3-hexylthiophene)-*block*-poly(*δ*-decanolactone)s (P3HT-*b*-PDLs) and poly(9,9-di-*n*-hexyl-2,7-fluorene)-*block*-poly(*δ*-decanolactone)s (PF-*b*-PDLs) using PDL as bio-based soft segments have been designed for stretchable electronic device applications. The incorporated PDL segments with linear, two-armed and three-armed structures were synthesized from a metal-free, solvent-free and non-toxic ring-opening polymerization using *δ*-decanolactone as a bio-based monomer. The soft PDL segments can not only provide stretchability to conjugated polymers but also modulate the phase separation behavior and crystallinity of the BCPs, leading to stretchable semiconducting polymers with tunable mechanical and electrical properties.

In chapter 2, P3HT-*b*-PDLs with AB, BAB, B_2AB_2 and B_3AB_3 architectures (A: P3HT, B: PDL) were employed as the semiconducting layer of OFET. Through the soft-hard-soft type BCP design and the selective solvent process of cyclohexane, confined molecular assembly of the P3HT segment was achieved in the BCP films, leading to outstanding charge mobility of the BCPs that is comparable with the pristine P3HT homopolymer. Moreover, the branched PDL segments affect the crystallinity and phase separation of BCP, resulting in higher stretchability of the branched BCP films. Consequently, the B_3AB_3 device shows the best mobility retentions under up to 100% strain, and can endure 500 stretch-release cycles at 50% strain. Based on this research, I demonstrate a new architecture design for

conjugated/insulating BCP to elevate its stretchability without sacrificing charge mobility.

In chapter 3, PF-*b*-PDLs with AB, AB_2 and AB_3 architectures (A: PF, B: PDL) were designed as the electret layer of OFET memory. The diblock copolymers with branched PDL segments show more distinct phase separation and more condensed PF nanofibers in thin film states, creating polymer electret materials with higher trapping density. Consequently, the AB_3 device shows the highest memory window and memory ratio, demonstrating the best memory performance of the branched BCP. Regards the mechanical properties, all of the PDL-contained BCPs exhibit extraordinary stretchability that can endure up to 100% strain and maintain their memory performance, while the PF homopolymer can only endure up to 25% strain. On top of that, the AB_3 electret layer can endure 500 stretch-release cycles with good memory performance. This research provides a novel PF-based stretchable charge-trapping material as well as a new protocol to correlate thin-film morphology of BCP electret with memory device performance.

In this dissertation, a synthetic and racemic δ-decanolactone compound was used for the synthesis of PDL concerning the prize and purity of monomer. Since the chirality of repeat unit doesn't affect glass transition and crystallization of aliphatic polyesters with long carbon chain in the monomeric unit,[1] the author assumes that the PDL derived from natural and optically active δ-decanolactone will still be amorphous with similar physical properties.

Based on the present study, PDL can increase bio-based content (up to around 50%) and the stretchability of conjugated BCP. Here the author further elaborates the competitiveness of PDL against other petroleum-based polymers in the industry. Regarding physical property, PDL is a totally amorphous polymer with a low glass transition temperature at -64 °C and high hydrophobicity. One of the representative oil-based polymers with similar properties is poly(*n*-butyl acrylate) (PBA), a hydrophobic and amorphous polymer with a glass transition temperature at -57 °C. Previous studies reported the improved stretchability of conjugated block copolymers using PBA as a soft segment.[2, 3] In my research, the function of PBA soft polymer to improve the stretchability of conjugated block copolymer can be adequately replaced by PDL. From an economic perspective, the price of making PDL and PBA can be estimated from the cost of monomers. PBA can be synthesized from butyl acrylate, which is a significant acrylate ester in the polymer industry for the production of acrylic polymers. The industrial class butyl acrylate costs about 2 US dollars per kilogram. In comparison, the natural δ-decanolactone extracted from the plant costs 300 to 400 US dollars per kilogram.[4] Although the price and production scale of δ-decanolactone cannot compete with butyl acrylate yet, it is noteworthy that PDL is a 100% bio-based polymer, with no carbon footprint during production, while PBA is 100% petroleum-based. In the 2021 United Nations Climate Change Conference, also known as COP26, held in Glasgow, Scotland, UK, the countries in United Nations are being asked to come forward with ambitious emission reduction targets that align with reaching

net zero emission by 2050.[5] Therefore, it is expected that the countries will charge more carbon tax to companies, and the polymer materials with zero carbon emission will be more competitive against their oil-based counterpart. Moreover, PBA is usually synthesized from anionic or radical polymerization using a metal-containing catalyst with petroleum-based solvents such as toluene and tetrahydrofuran.[2, 3, 6] In contrast, PDL can be made from a metal-free and solvent-free ring-opening polymerization. The author points out this as another advantage of PDL over PBA that should be concerned.

Another important issue, although it is rarely discussed in stretchable device applications, should be considered is long-term durability of stretchable device. The synthesized BCPs, P3HT-*b*-PDLs and PF-*b*-PDLs, possess one glass transition temperature below -50 °C from the insulating PDL segments and melting points of conjugated segments, P3HT and PF, over 150 °C. As operating the devices at room temperature, heat generated within electronic device may increase polymer chain mobility of the amorphous PDL soft segment, while the crystalline structure formed by conjugated segments which contributes to the electronic performance of device can be retained owing to the high melting points. Therefore, the author speculates that the electronic performance of the devices made by our BCPs may not be weaken too much due to the retained structure of conjugated segments during operation at room temperature, while the devices may not perform well at above 100 °C. Long-term durability of the devices at room and elevated temperature should be evaluated in the future to verify this idea.

4.2 Future Work

Succeeding works related to the synthesis of bio-based conjugated BCPs and their applications that can be done in the future are summarized below:

(1) For the development of stretchable semiconductor, synthetic strategy of conjugated polymer with high charge mobility (> 1 cm^2 V^{-1} S^{-1}), controlled molecular weight and controlled end-functionality is urgently demanded. For example, Park et al. reported a low-crystallinity poly(thiophene-*co*-hexylthiophene) with greatly enhanced charge mobility of 1.37 cm^2 V^{-1} S^{-1}.[7] This polymer can be used as the conjugated segment for high-performance BCP using similar synthetic strategy as that of the current P3HT-based BCP. Also, Lipomi et al. have reported a stretchable and degradable semiconducting block polymer recently based on a high-performance donor-acceptor polymer, diketopyrrolopyrrole (DPP).[8] However, donor-acceptor polymers cannot be synthesized through living polymerization, so they generally show higher dispersity. Therefore, the development of controlled polymer synthesis for donor-acceptor polymer should be of great potential.

(2) For the development of electret layer, some of the applications related to electron-trapping material and photonic memory device are of great interests. Polyfluorene generally shows hole-trapping ability. However, by introducing β phase of polyfluorene, one can create self-doped nanostructures with electron-trapping ability.[9] Therefore, by creating polyfluorene-based BCP using polyfluorene that possesses β phase such as poly(9,9-di-*n*-octyl-

2,7-fluorene) (PFO), one can realize a stretchable electron-trapping material. Recently, polyfluorene materials have drawn research attentions as a photo-chargeable electret layer[10, 11] since it can easily absorb blue and ultraviolet light and generate excitons. Therefore, nw material design and device manufacturing strategy for polyfluorene-based stretchable photonic memory are highly expected.

(3) For the bio-based soft segments, extra functionality of the soft segment is expected. In the previous studies of conjugated/insulating BCP, the focus lies on tuning mechanical properties of the semiconducting polymer by introducing insulating blocks. One can introduce other functionality to the bio-based polymers by using a monomer with reactive functional groups. For example, Jasmine lactone (CAS: 25524-95-2) occurs naturally in Jasmine oil, tea and peach, etc. It has a similar structure to δ-decanolactone but with a reactive double bond on the side chain. Therefore, it can be used to develop bio-based polyester as a building block for BCP with additional functionality.

Based on the results in Chapter 2 and Chapter 3, new material design and applications of bio-based functional polymers for advanced optoelectronic applications are proposed (**Scheme 4.1**). In addition to improve stretchability of BCP and study topology effect, other functions of bio-based polymers can be explored. Polymers with hydrogen bonding possess multiple advantages including advanced solubility in water,[12] stimuli-response to temperature and acidity,[13] forming amphiphilic block copolymers[14] and ability to generate supramolecular

structure.[15] As shown in **Scheme 4.1a**, poly(jasmine lactone) as a bio-based and soft polymer matrix can be obtained through a DPP-catalyzed ring-opening polymerization of Jasmine lactone. Carboxylic acid or amide functional groups can be introduced to the side-chain of poly(jasmine lactone) by a one-step thiol-ene reaction using different thiols such as 3-mercaptopropionic acid, 2-aminoethanethiol or L-cysteine. Thus the modified poly(jasmine lactone) can provide hydrogen-bonding with well-known natural dyes such alizarin red, and quercetin, leading to a bio-based and photosensitive polymer/dye composites. Such composites can be used as green electret layer of photonic OFET memory. On the other hand, as shown in **Scheme 4.1b**, conjugated BCP can be formed through click reaction between azido-functional poly(jasmine lactone) and conjugated polymer such as polyfluorene. Through thiol-ene post-modification of the BCP, amphiphilic and conjugated block copolymer can be formed. Such polymers should be useful as water and alcohol-soluble polymer electret at thin-film state. Regards the solution state, the BCPs could form micellar structure and the stimuli-response of BCP should be investigated.

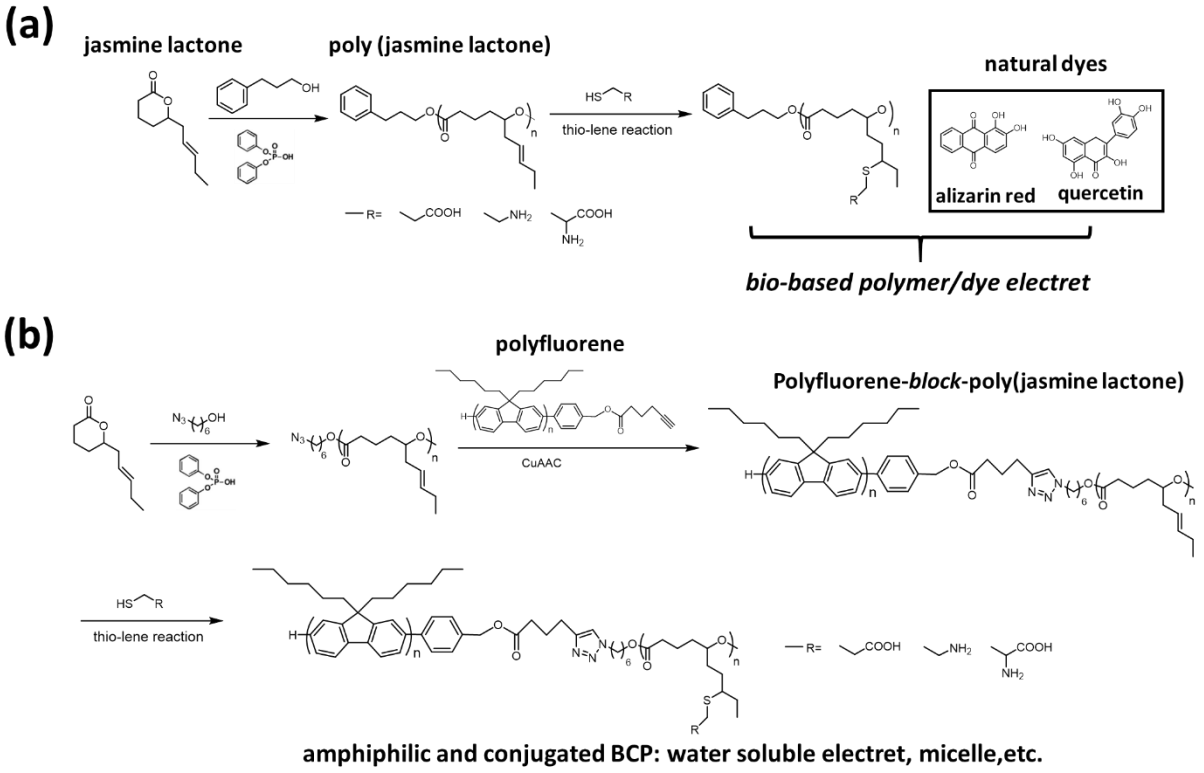

Scheme 4.1 Proposed future work: (a) Bio-based poly(jasmine lactone)/dye composites with hydrogen-bonding, (b) amphiphilic and conjugated BCP containing poly(jasmine lactone).

4.3 Reference

1. C. Zhang, D. K. Schneiderman, T. Cai, Y.-S. Tai, K. Fox and K. Zhang, *ACS Sustain.Chem. Eng.,* 2016, **4**, 4396-4402.
2. J.-T. Wang, S. Takshima, H.-C. Wu, C.-C. Shih, T. Isono, T. Kakuchi, T. Satoh and W.-C. Chen, *Macromolecules*, 2017, **50**, 1442-1452.
3. H.-C. Hsieh, C.-C. Hung, K. Watanabe, J.-Y. Chen, Y.-C. Chiu, T. Isono, Y.-C. Chiang, R. R. Reghu, T. Satoh and W.-C. Chen, *Polym. Chem.*, 2018, **9**, 3820-3831.
4. "Buy Delta Decalactone,713-95-1,Farwell 713-95-1 Delta Decalactone Product on Alibaba.com", 2021, **7**, Data sources are from: https://www.alibaba.com/product-detail/Farwell-713-95-1-Delta-Decalactone_326909813.html?spm=a2700.galleryofferlist.normal_offer.d_title.11dlleeejsfbal
5. "What do we need to achieve at COP26?", UN Climate Change Conference UK 2021, Data sources are from: https://ukcop26.org/cop26-goals/.
6. R. Fayt, R. Forte, C. Jacobs, R. Jérôme, T. Ouhadi, P. Teyssié and S. K. Varshney, *Macromolecules*, 1987, **20**, 1442-1444.
7. S. Y. Son, Y. Kim, J. Lee, G.-Y. Lee, W.-T. Park, Y.-Y. Noh, C. E. Park and T. Park, *J. Am. Chem. Soc.,* 2016, **138**, 8096-8103.
8. F. Sugiyama, A. T. Kleinschmidt, L. V. Kayser, M. A. Alkhadra, J. M.-H. Wan, A. S.-C. Chiang, D. Rodriquez, S. E. Root, S. Savagatrup and D. J. Lipomi, *Macromolecules*, 2018, **51**, 5944-5949.
9. H. Ling, J. Lin, M. Yi, B. Liu, W. Li, Z. Lin, L. Xie, Y. Bao, F. Guo and W. Huang, *ACS Appl. Mater. Interfaces*, 2016, **8**, 18969-18977.
10. C.-C. Shih, Y.-C. Chiang, H.-C. Hsieh, Y.-C. Lin and W.-C. Chen, *ACS Appl. Mater. Interfaces*, 2019, **11**, 42429-42437.
11. Y.-C. Chen, Y.-C. Lin, H.-C. Hsieh, L.-C. Hsu, W.-C. Yang, T. Isono, T. Satoh and W.-C. Chen, *J. Mater. Chem. C*, 2021, **9**, 1259-1268.
12. H. A. Al-Attar and A. P. Monkman, *Adv. Funct. Mater.*, 2012, **22**, 3824-3832.
13. C.-L. Liu, C.-H. Lin, C.-C. Kuo, S.-T. Lin and W.-C. Chen, *Prog. Polym. Sci.*, 2011, **36**, 603-637.
14. W.-C. Wu, C.-Y. Chen, W.-Y. Lee and W.-C. Chen, *Polymer*, 2015, 65, A1-A16.
15. S. Burattini, B. W. Greenland, D. H. Merino, W. Weng, J. Seppala, H. M. Colquhoun, W. Hayes, M. E. Mackay, I. W. Hamley and S. J. Rowan, *J. Am. Chem. Soc.*, 2010, **132**, 12051-12058.